Cover Page

Submitted to: Department of Energy/National Energy Technology Laboratory
Federal Grant: DE-FE0031794
Project Name: Conversion of Domestic US Coal into Exceedingly High-Quality Graphene
PI Name, Title, E-mail, Phone: James M. Tour, Ph.D., T.T. and W.F. Chao Professor of Chemistry, tour@rice.edu, 713-348-6246
Name of Submitting Official, Title, E-mail, Phone: Heidi Thornton, Ph.D., Assistant Director, Office of Sponsored Projects & Research Compliance, sparc@rice.edu, 713-348-6200
Submission Date: July 1, 2022
DUNS Number: 05-029-9031
Recipient Organization: William Marsh Rice University, P.O. Box 1892 – MS 16 Houston, TX 77251-1892
Project/Grant Period: 10/01/2019 through 09/30/2021
Reporting Period End Date: 30 September 2021
Report Term: Final Technical Report

Signature of Submitting Official: Heidi Thornton

ACKNOWLEDGMENT This material is based upon work supported by the U.S. Department of Energy under Award Number DE-FE0031794.

Table of Contents

Conversion of Domestic US Coal into Exceedingly High-Quality Graphene

Introduction to the Project

A. Objectives of the project

We will study how flash Joule heating (FJH) of anthracite and bituminous coal, as well as other carbon sources, affords graphene in gram scales in <1 s. The graphene is termed flash graphene (FG). The process uses no furnace and no solvent or reactive gases, and the yields, depending on the carbon content of the source, can range from 70-95% with a purity >99%. The scaled electrical energy cost is ~$100 per ton. FG can be among the lowest defect graphene ever reported (2D/G = 17:1) and turbostratic by powder X-ray diffraction (XRD) analysis, meaning that is has little order between the graphene layers, thereby facilitating. FG might provide the long-sought method to make graphene in bulk with industrially acceptable economics: inexpensive coal, furnace-free, solvent-free and chemical-free processing, and low-energy input so as to render it suitable for bulk plastic, metal and even concrete composites.

B. Scope of Work of the project

The scope of work includes studying how FJH of coal produces FG. Using the funds provided here, in the first year of funding reaction equipment was built, the reactions of different feedstocks were studied, and data was gathered and analyzed. Iterations were to produce the best FG for the several applications discussed in the technical proposal. In the second year of funding, scale-up equipment was built that will be designed to meet the yield and quantity targets laid out by the Department of Energy.

In-depth study of flash graphene materials properties 1.

Introduction.

Flash Joule heating (FJH) has been demonstrated to be a method to convert almost any carbon-based precursor into bulk quantities of graphene. Here we explore the morphologies and properties of flash graphene (FG) generated from carbon black. It is shown that FG is partially comprised of sheets of turbostratic FG (tFG) that have a rotational mismatch between neighboring layers. These tFG sheets exhibit moiré patterns revealed by TEM imaging. The remainder of the FG is wrinkled graphene sheets that resemble non-graphitizing carbon. To generate high quality tFG sheets, a FJH duration of 30 – 100 ms was employed. Beyond 100 ms, the turbostratic sheets have time to AB-stack and form bulk graphite. Theoretical simulations revealed that wrinkled graphene is predominantly formed because of simple thermal annealing and displays minimal to no alignment of graphitic planes, as opposed to the high-quality tFG that is formed under the direct influence of current conducted through the material. The tFG was easily exfoliated *via* shear, hence the FJH process has the potential for bulk production of tFG without the need for chemical exfoliation or high energy mechanical shear.

Graphene is defined as 2-dimensional sheets of sp^2-hybridized carbon.[1,2] Because of the stable carbon-carbon covalent bonding and sp^2-hybridization, graphene exhibits high carrier mobility,[3] thermal conductivity,[4] and mechanical strength, among other favorable properties.[5] Graphene is

typically synthesized by chemically or mechanically intensive top-down methods[6] or slow bottom-up methods.[2,7] Top-down approaches often start with bulk graphite that is subsequently exfoliated into sheets by mechanical, electrochemical, or chemical processes, such as *via* the production of graphene oxide with subsequent reduction. Bottom-up graphene growth is usually carried out by chemical vapor deposition (CVD), which is suitable for the growth of single to few-layer graphene films. However, CVD growth typically results in small quantities of graphene generated and is not a suitable method for bulk graphene production where a large mass of graphene is desired.
Recently, bulk quantities of flash graphene (FG) have been generated in a process by which virtually any carbon source is converted to graphene using flash Joule heating (FJH).[8] The FG is largely turbostratic, which facilitates ease in exfoliation and dispersibility. The turbostratic FG (tFG) is significantly mechanically, electronically, and optically decoupled from neighboring sheets, resulting in spectroscopic signatures like high-quality monolayer graphene. The high-power FJH rapidly heats the carbon precursor and causes outgassing of non-carbon elements. Rapid cooling prevents rotational registration of graphene sheets and promotes the formation of tFG sheets. In this section, the production and morphology of FG are studied. The mechanism by which turbostratic sheets are assembled is explored.

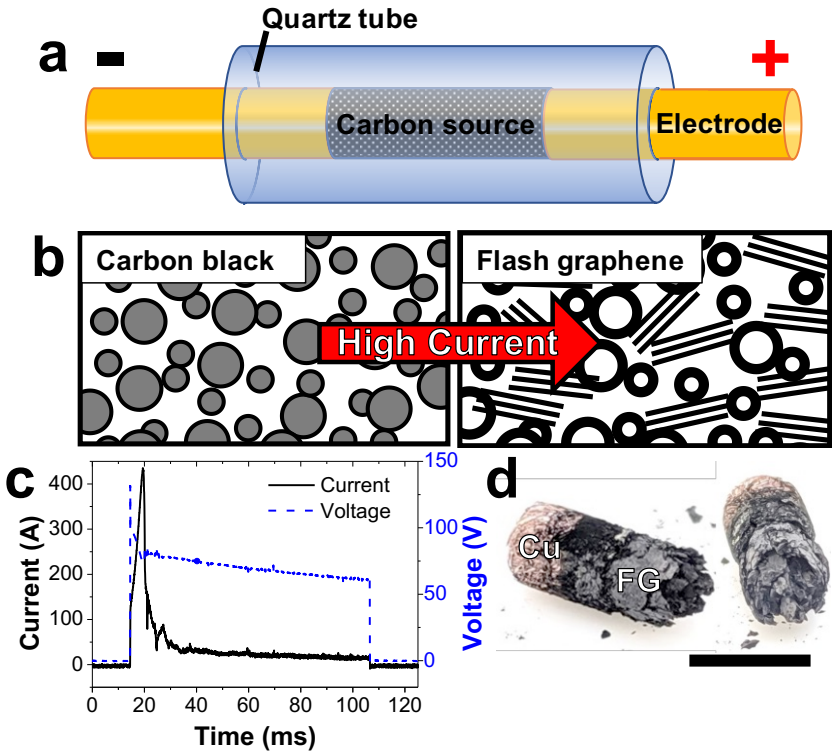

Figure 1.1 General FJH characteristics. (a) Schematic of setup for FJH of a carbon source to form FG. (b) Schematic representing the graphitization of the carbon source after FJH. In the product (right) the circles represent graphitized carbon. The lines represent FG sheets. (c) Current (black) and voltage (blue) passed through the carbon source during FJH. (d) Photograph of FG after FJH as it was pushed from the quartz tube and broken in two. Copper wool was used as an

electrode, but this is easily substituted with a refractory conductor such as graphite rods. Scale bar is 5 mm.

To synthesize FG, carbon black (CB) was enclosed within a quartz tube and pressed between two copper electrodes with copper touch the CB, as shown in **Figure 1.1a**. The electrodes were connected to a capacitor bank with a total capacitance of 60 mF and charged to a voltage of 120 V. Controlled discharge of the capacitor banks through the CB results in FJH that rapidly heats the CB to ~ 3000 K within tens of ms and then it cools to room temperature within seconds.[8] During the discharge time period, the CB is rapidly heated and graphitized to form FG, as illustrated in **Figure 1.1b**. **Figure 1.1c** reports the current and voltage across the CB for a FJH duration of 100 ms. Notably, a peak current of > 400 A passes through the CB that results in a rapid power dissipation of ~ 30 kW. This high-power dissipation is responsible for the rapid FJH. During FJH, the CB forms planar crystals of tFG that are aligned in the direction of current and resemble a charred log (**Figure 1.1d**). The CB starting material is predominantly comprised of small particles that are largely amorphous carbon. After 100 ms of FJH, sheets of tFG are dispersed throughout the sample along with small, graphitized carbon particles, thus resulting in the bulk bottom-up synthesis of graphene.

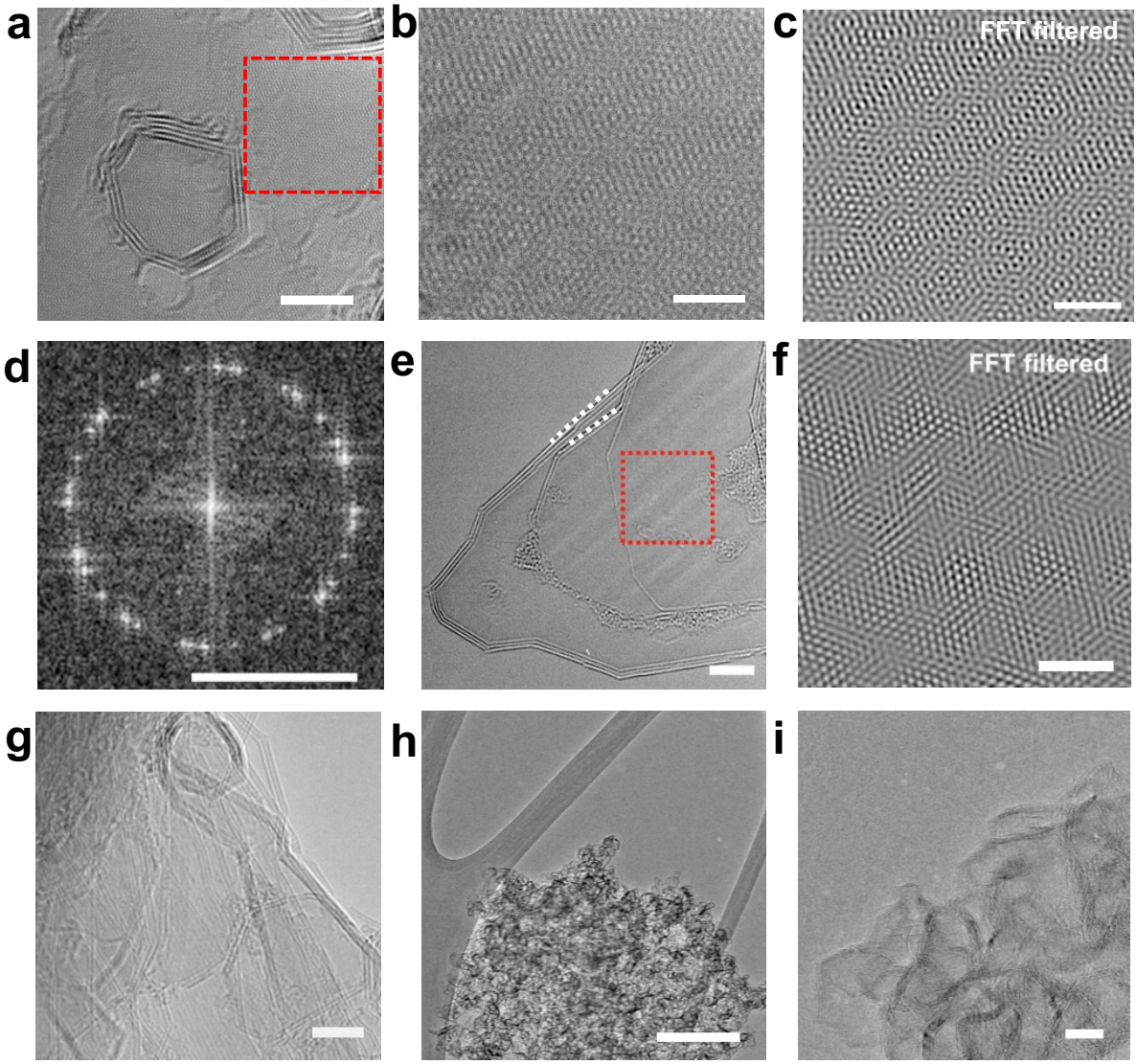

Figure 1.2. Microscopic analysis of the FJH products. (a) TEM image of tFG sheets. Scale bar is 5 nm. (b) High-resolution TEM of tFG and (c) FFT filtered image of b. Scale bars are 2 nm. (d) FFT of the HR-TEM image in b. Scale bar is 5 nm^{-1} (e) TEM image of tFG with striations in the image denoting rotational mismatch. Scale bar is 5 nm. (f) FFT filtered image of the inset region in e revealing a moiré pattern. Scale bar is 2 nm. (g) TEM image of tFG showing more striations indicating a rotational mismatch. Scale bar is 5 nm. (h) TEM image of wrinkled graphene produced from the FJH procedure. Scale bar is 200 nm. (i) HR-TEM image of the wrinkled graphene. Scale bar is 10 nm.

High-resolution transmission electron microscopy (HR-TEM) was conducted to observe the atomic structure of FG, and **Figure 1.2a** shows tFG sheets. A HR-TEM image of the inset red box region is shown in **Figure 1.2b**. **Figure 1.2c** shows an FFT-filtered image of this region, revealing the presence of moiré patterns in the lattice consistent with a rotational mismatch. **Figure 1.2d** reports a fast Fourier transform (FFT) of the region that is comprised of 30 distinct Bragg spots

(each graphene layer consisting of 6 Bragg spots). This indicates that the region is comprised of 5 layers of tFG with a rotational mismatch between each layer. The rotational mismatch is further analyzed in the **Figure A1.1**. **Figure 1.2e** shows other sheets of tFG. A slight rotational mismatch between sheets (denoted by the non-parallel inset dotted lines), results in a moiré pattern that manifests itself as striations in the image only where the mismatched sheets overlap. The rotational mismatch between these sheets is ~ 5.4°. The moiré pattern induced by the rotational mismatch is more clearly shown in **Figure 1.2f. Figure 1.2g** shows similar striations in the image due to a rational mismatch between neighboring sheets of graphene. As depicted in **Figure 1.1b**, a FG sample is comprised of sheets of tFG as well as smaller particles of graphitic carbon. The HR-TEM images of the smaller particles are shown in **Figure 1.2h** and 1.**2i**. This material is graphitic with many bends and typically has a thickness of 3-8 layers.[8] It resembles non-graphitizing carbon[9,10] and will be referred to as wrinkled graphene in this work. TEM images of both forms of graphene reveal an interatomic spacing of ~ 0.34 nm, which corresponds with turbostratic material and lack of AB-stacking (**Figure A1.2**).

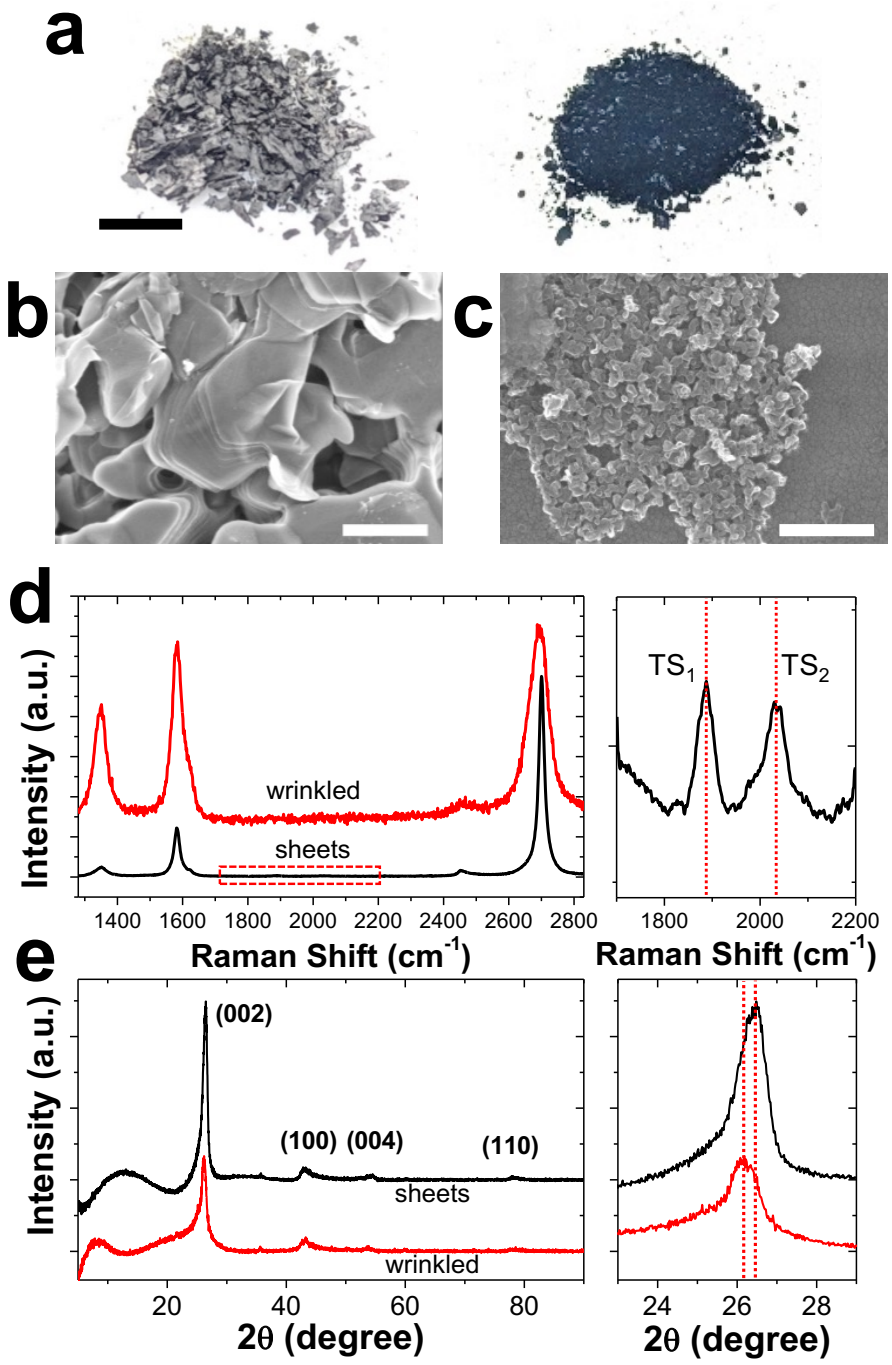

Figure 1.3. FJH product morphologies and spectral characteristics. (a) Photographs of FG that was passed through a 250 μm sieve. Gray crystals are separated from a fine black powder. The scale bar is 3 mm. (b) SEM image of the gray crystals showing delaminating sheets. Scale bar is 500 nm. (c) SEM image of the black powder that is comprised of nanoparticles. Scale bar is 300 nm. (d) Representative Raman spectra for sheets and wrinkled structures. Expansion of the red boxed region from the sheets (right) exhibit TS_1 and TS_2 peaks that are characteristic of turbostratic

layers and show a missing M band. (e) X-ray diffraction of sheets and wrinkled structures. A shift in the peak position of (002) peak is exhibited for the wrinkled structures.

Upon synthesizing FG, the sample is comprised of gray crystals and a fine black powder, as shown in **Figure 1.3a,** and the combined yield is ~85% by weight. The two components can easily be separated by screen-sieving since the gray crystals coalesce into larger particles. SEM imaging reveals that the gray crystals (**Figure 1.3b**) are extended networks of tFG sheets that readily exfoliate and delaminate, whereas the fine black powder is the wrinkled graphene. Representative Raman spectra of the tFG sheets and wrinkled graphene are shown in **Figure 1.3d**. The wrinkled graphene is further characterized by a 2D/G ratio of ~ 1.1 and a large D peak, presumably due to extensive curvature of the wrinkled graphene.[11] The tFG sheets exhibit a much larger 2D/G ratio with a minimal D peak. The tFG sheets also have distinct TS_1 and TS_2 peaks confirming that the FG is indeed turbostratic. These peaks only arise due to rotational mismatch between neighboring layers of graphene.[8,12] A more thorough analysis of the Raman spectra with peak fitting is provided in the **Figure A1.3** and **A1.4**. X-ray diffraction for each morphology is shown in **Figure 1.3e**. An asymmetric (002) peak is exhibited along with a weak (100) peak. These characteristics are typically exhibited in turbostratic graphene.[13,14] The (002) peak for tFG sheets is more pronounced than in the wrinkled graphene, which suggests a larger crystallite size in the c-axis. This is evident by observing the SEM image in **Figure 1.2b** that reveals the crystals of tFG sheets may be many layers thick and on the order of microns. **Figure A1.5** shows cross-sectional SEM images of the tFG crystals.

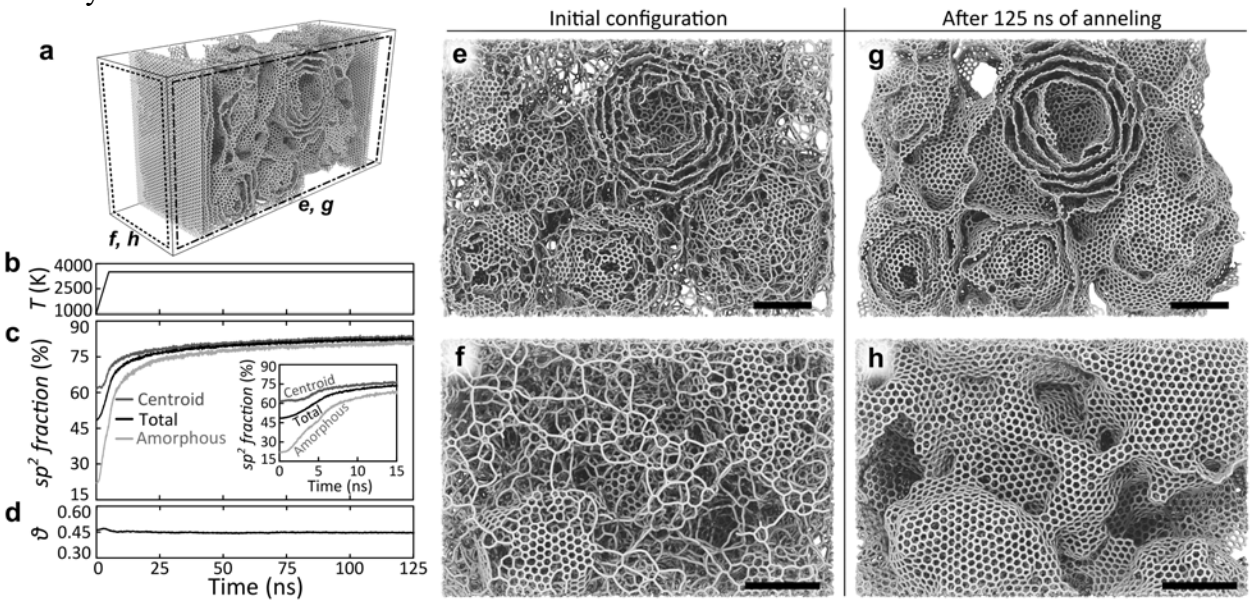

Figure 1.4. Modeling of flash graphene formation. (a) Structure of the amorphous carbon used for a molecular dynamics simulation of high-temperature annealing; vertical graphitic walls can be seen towards the front and back of the frame. (b) The temperature profile, (c) graphitization level, and (d) Herman's orientation function during the annealing. Visual comparison of (e,f) the initial configuration and (g,h) final configurations show a significant level of graphitization. Direction of view is indicated in (a), graphitic walls are omitted. Interestingly, the fraction of the sp^2 carbon within centroid particles changes significantly less compared to amorphous material (c), indicating an increased annealing barrier for atoms within the preexisting graphene-like

structure. At the same time, Herman's orientation function (d) shows no significant re-orientation or alignment of graphitic structures despite the presence of walls. Scale bars are 2 nm.

Molecular Dynamics Simulations

The drastic difference in morphology of tFG and wrinkled graphene originates in non-uniform formation conditions. Using molecular dynamics simulation with AIREBO potential (see **Appendix 1.1** for details), we analyzed the process and results of the prolonged high temperature annealing of CB material (**Figure 1.4**). The initial structure was designed to contain ~ 66 % of centroid particles characteristic for CB and ~ 34 % of loose amorphous carbon and surrounded by graphitic walls to emulate the presence of glass walls during the FJH process (**Figure 1.4a**). After initial pre-treatment at 1000 K for 5 ns, the material was exposed to heating and consequent annealing at a constant temperature of 3500 K (**Figure 1.4b**) while graphitization (**Figure 1.4c**) and Herman's orientation function (**Figure 1.4d**) of the material was monitored. As expected, the graphitization level, specifically the fraction of carbon atoms in sp^2-configuration, significantly increases from ~ 60 % to 85 % during the annealing process, with the most significant change occurring during the initial heating period (**Figure 1.4c** inset). Interestingly, the material within centroid particles appears to be significantly less mobile compared to the loose amorphous carbon resulting in smaller graphitization increase due to slow annealing of defects trapped in graphene-like centroid shells. At the same time, surrounding amorphous carbon does not have a rigid pre-existing structure and undergoes rapid graphitization resulting in the formation of graphene-like coating covering centroid particles (**Figure 1.4e-h**). Taking experimental observations as a guide, we analyzed the alignment of graphitic domains within the structure during annealing using Herman's orientation function θ, commonly used in polymer science. Computed as $\theta = (3\langle\cos^2\alpha\rangle - 1)/2$, where α is an angle between the local direction of the graphitic plane and the characteristic direction chosen to be horizontal (see Appendix **1.** for details and **Figure A1.6**), the orientation function is expected to be equal to -0.5, 1 and 0 for domains aligned with graphitic walls, perpendicular to the walls and randomly oriented, respectively. No significant change of alignment is observed during the annealing process (**Figure 1.4d**), mainly preserving the value dictated by the initial configuration. Even prolonged thermal annealing at high temperatures (125 ns, 3500 K) does not show a structural change characteristic for the formation of tFG by FJH only wrinkled structure is observed (see **Figure 1.3c** and **Figure 1.4h**). From these observations, we can conclude that wrinkled graphene forms at the areas of material undergoing simple thermal annealing. At the same time, the current and its directionality might guide formation of tFG.

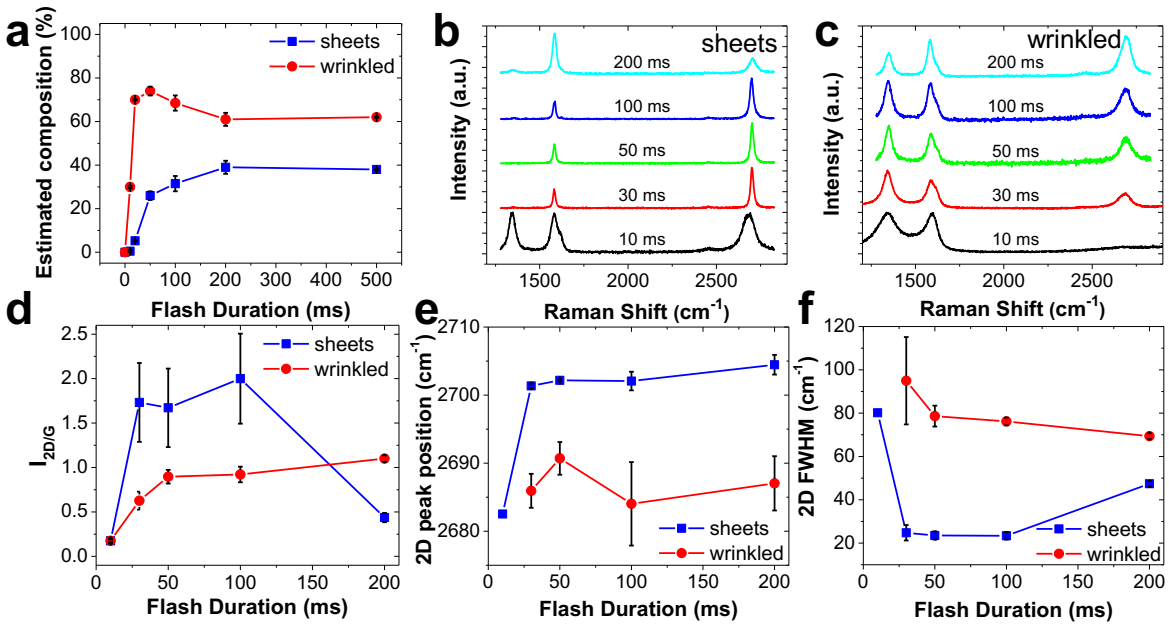

Figure 1.5. Effect of flash time duration on properties. (a) Estimated composition of a batch of FG as a function of FJH flash duration. (b) Representative Raman spectra at various flash durations for (b) tFG sheets and (c) wrinkled graphene. Analysis of Raman spectra reporting the (d) 2D/G intensity ratio, (e) 2D peak position, and (f) 2D FWHM. The error bar represents the standard deviation where N = 10.

Tuning Reaction Conditions to Vary Composition and Morphology

By controlling the flash duration through electrical pulse cessation during which FG is generated, the composition and morphology of FG can be tuned. Using an image analysis technique and Raman spectra (see **Figure A1.7** for more details), the amount of tFG sheets and wrinkled graphene is estimated as a function of the flash duration in **Figure 1.5a**. At t = 0 ms, the entire batch of material is amorphous carbon. Upon FJH, tFG sheets and wrinkled graphene are produced. The amount of tFG sheets increases relative to wrinkled graphene until a ~ 200 ms pulse is applied. Beyond 200 ms, the composition of tFG sheets remains unchanged. **Figure 1.5b** and **1.5c** show representative Raman spectra for the tFG sheets and wrinkled graphene. Complementary SEM images of the material are reported in **Figures A1.8 and A1.9**. Notably, tFG sheets exhibit much narrower peak full width at half maximum (FWHM) and more pronounced 2D peaks. Analysis of the Raman spectra for FG morphologies is reported in **Figures 1.5d – 1.5f.** The 2D/G ratio gives a reflection of graphene quality, and generally higher 2D/G ratio is exhibited by high quality graphene with low defect concentration. For the wrinkled graphene, the 2D/G ratio increases with flash duration and largely saturates beyond 100 ms once full graphitization has occurred. For the tFG sheets, the average 2D/G ratio is ~1.8 to 2.0 up to 100 ms; however, the 2D/G ratio decreases to ~ 0.4 with a flash duration of 200 ms and beyond. These results indicate that rotationally decoupled tFG is formed during short flash durations (30 to 100 ms). When prolonged FJH is supplied (200 ms), the tFG sheets begin to AB-stack and form bulk graphite, as confirmed by the reduction in 2D/G ratio and the increase in 2D FWHM. **Figure 1.5e** shows the position of the 2D peak. Once the tFG sheets begin to form and planarize, the 2D peak shifts from ~ 2683 cm^{-1} to

2701 cm^{-1}. **Figure 1.5f** reports the FWHM of the 2D peak for the tFG sheets and wrinkled graphene. Between 30 to 100 ms pulse duration, the tFG sheets exhibit a narrow FWHM averaged around 23 cm^{-1} that can be fitted with a single Lorentzian peak. This optically decoupled behavior is similar to the FWHM of a single layer of graphene. Therefore, modulation of the FJH conditions yield differing compositions according to the desired product. Additional images and Raman spectra of tFG sheets, wrinkled graphene, and other morphologies formed can be found in **Figures A1.10 – A1.16**. Some regions from a batch of FG formed densely packed graphite polyhedral crystals (GPCs). **Figure A1.13** shows that the GPCs form faceted rods. The Raman spectra typically displayed a 2D/G ratio of ~ 1.0. **Figure A1.14** shows more images of various GPC morphologies ranging from cones to high aspect-ratio rods.

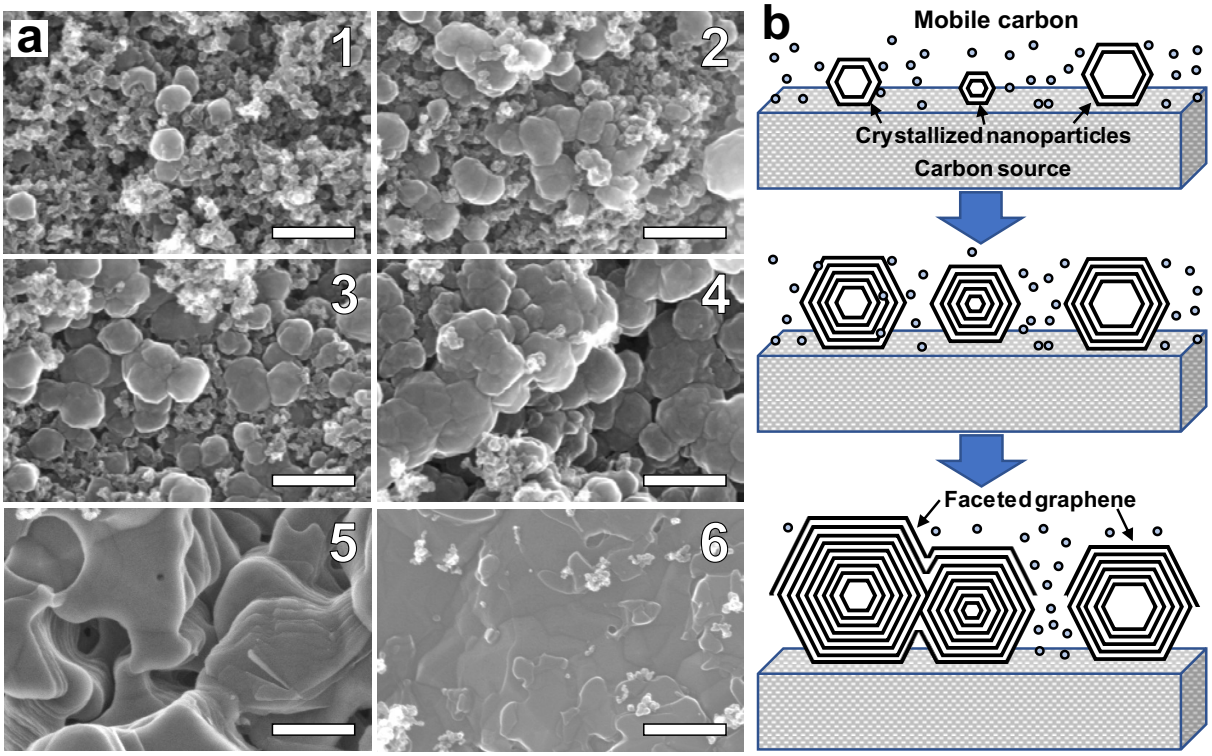

Figure 1.6. Morphology growth patterns. (a) SEM images showing nucleation and growth of graphitic crystals across the surface of a bed of graphitic nanoparticles. Crystals merge and eventually form a continuous graphitic shell. All scale bars are 300 nm. (b) Proposed mechanism for the formation of FG on the surface of graphitic crystals.

Mechanism of Formation of FG

Figure 1.6 shows SEM images taken from various regions of tFG that show the progression of tFG formation. In the image (1) seeds of faceted spherical particles can be seen nucleating in a bed of carbon. These seeds grow and merge in images (2) – (4). Eventually, layers of faceted tFG sheets form on the top of merged seeds (5). These regions generally exhibit the spectroscopic signatures of turbostratic graphene with Raman 2D/G ratios reaching > 15 (**Figure A1.11**). With sufficient heating time, the FG sheets merge and begin to AB stack and form more continuous graphite (6). **Figure A1.17** shows the effect of power dissipation during flashing on the nucleation

and growth of tFG. A sharp increase in the resistance of the carbon source after ~ 15 ms of flash duration suggests that the material becomes discontinuous potentially due to mobile carbon generation or gas evolution. The mobile carbon may originate from high resistance junctions between neighboring carbon particles parallel to the path of current. Previous work has shown that sublimed carbon will form turbostratic particles similar to those seen in **Figure 1.6a**.[15] **Figure 1.6b** shows a proposed mechanism for tFG formation. The carbon source for the formation of tFG is likely mobile carbon from a bed of carbon black. As mobile carbon is generated, faceted nanoparticles begin to nucleate. These nanoparticles will merge and eventually faceted sheets of tFG form along the top of the nucleated particles, as shown in **Figure 1.6a**.

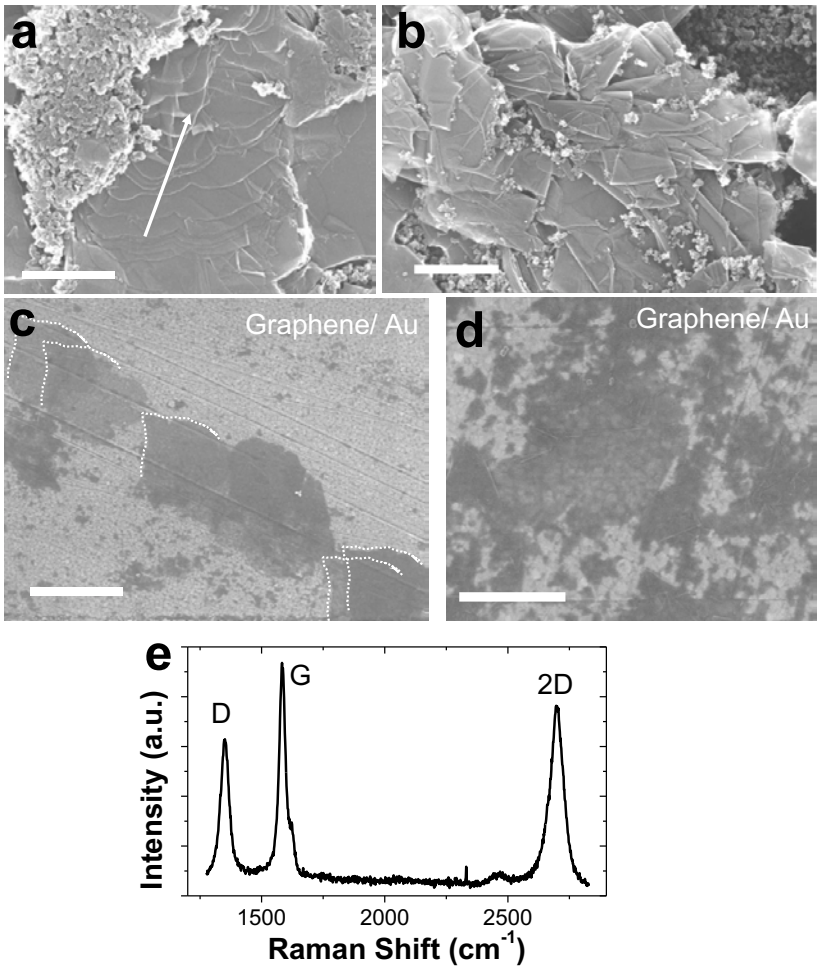

Figure 1.7. Exfoliation of tFG. (a,b) SEM images of gray crystal that were mechanically sheared, showing facile delamination of the bulk material. Scale bars are 500 nm. (c, d) Large area exfoliation of FG on an Au substrate (sheet edges were outlined for SEM image contrast). Scale bars are 1 μm and 400 nm, respectively. (e) Representative Raman of exfoliated FG.

Due to the increased interplanar spacing of tFG sheets, there are weaker van der Waals interactions between neighboring layers leading to more facile exfoliation. **Figure 1.7a** and **1.7b** show bulk crystals of tFG that were subject to shear. The crystals of tFG sheets readily delaminate due to the weak interlayer interactions. This material was exfoliated from a silicon wafer onto an Au substrate for SEM imaging clarity. **Figure 1.7c** and **1.7d** show that the tFG sheets are easily transferred to

the Au substrate. The dotted lines in **Figure 1.7c** indicate a common edge on the graphene sheets that show these sheets were all exfoliated from the same crystal of tFG. A Raman spectrum of the exfoliated graphene is reported in **Figure 1.7e** and reveals the presence of high-quality graphene. The high D-peak is likely induced from damage to the sheet from the exfoliation process and the non-flat Au surface. The tFG can be easily exfoliated by mechanical shear (**Figures A1.18 – A1.22**), as well as by dispersion in solutions such as oleum (**Figure A1.23**).

Conclusions of this flash graphene morphology study 1.

This works shows that FG is comprised of turbostratic sheets of graphene as well as wrinkled graphene as confirmed by high resolution TEM. Spectroscopically, the turbostratic sheets behave optically as monolayer graphene with high 2D/G peak ratios and narrow FWHM. The duration of FJH influences the composition of the FG and controls the ratio of tFG sheets to wrinkled graphene. Extended FJH (> 200 ms) causes the material to AB-stack to form graphite. Therefore, to generate high quality tFG, the flash duration should be maintained at ~30 to 100 ms; the experimental conditions presented in this work. The tFG can easily be exfoliated under shear, thus providing a method to generate bulk quantities of graphene.

References 1.

1. Geim, A. K. & Novoselov, K. S. The rise of graphene. *Nat Mater* **6**, 183–191 (2007).
2. Li, X. *et al.* Large-area synthesis of high-quality and uniform graphene films on copper foils. *Science.* **324**, 1312–1314 (2009).
3. Bolotin, K. I. *et al.* Ultrahigh electron mobility in suspended graphene. *Solid State Commun.* **146**, 351–355 (2008).
4. Balandin, A. A. Thermal properties of graphene and nanostructured carbon materials. *Nature Materials* **10**, 569–581 (2011).
5. Papageorgiou, D. G., Kinloch, I. A. & Young, R. J. Mechanical properties of graphene and graphene-based nanocomposites. *Progress in Materials Science* **90**, 75–127 (2017).
6. Marcano, D. C. *et al.* Improved synthesis of graphene oxide. *ACS Nano* **4**, 4806–4814 (2010).
7. Li, X. *et al.* Large-Area Graphene Single Crystals Grown by Low-Pressure Chemical Vapor Deposition of Methane on Copper. *J. Am. Chem. Soc.* **133**, 2816–2819 (2011).
8. Luong, D. X. Gram-scale bottom-up flash graphene synthesis. *Nature* **577**, 647–651 (2020).
9. Harris, P. J. F. & Tsang, S. C. High-resolution electron microscopy studies of non-graphitizing carbons. *Philos. Mag. A* **76**, 667–677 (1997).
10. Harris, P. J. F. New Perspectives on the Structure of Graphitic Carbons. *Crit. Rev. Solid State Mater. Sci.* **30**, 235–253 (2005).
11. Dimiev, A. M. *et al.* Direct Real-Time Monitoring of Stage Transitions in Graphite Intercalation Compounds. *ACS Nano* **7**, 2773–2780 (2013).
12. Garlow, J. A. *et al.* Large-Area Growth of Turbostratic Graphene on Ni(111) via Physical Vapor Deposition. *Sci. Rep.* **6**, (2016).
13. Fujimoto, H. Theoretical X-ray scattering intensity of carbons with turbostratic stacking and AB stacking structures. *Carbon N. Y.* **41**, 1585–1592 (2003).
14. Li, Z. Q., Lu, C. J., Xia, Z. P., Zhou, Y. & Luo, Z. X-ray diffraction patterns of graphite and turbostratic carbon. *Carbon N. Y.* **45**, 1686–1695 (2007).
15. Kokai, F., Ishihara, M., Koshio, A., Nakayama, A. & Koga, Y. Fabrication of some

graphitic polyhedra and balloon-like particles. *Diam. Relat. Mater.* **16**, 1264–1268 (2007).

Appendix 1.1

Fast-Fourier transform (FFT) of HR-TEM images reveals Bragg spots with rotational mismatch in **Figure A1.1**. Each set of 6 Bragg spots represents a single layer of FG and is indicated by the inset yellow hexagons. This region was composed of 5 sets of turbostratic FG (tFG) with rotational mismatch. **Figure A1.2** shows HR-TEM images of spherical flash graphene particles. These particles are faceted hexagonal crystals which are composed of concentric layers of graphitic carbon. The interlayer spacing was 3.4 Å, which corresponds with turbostratic graphene.

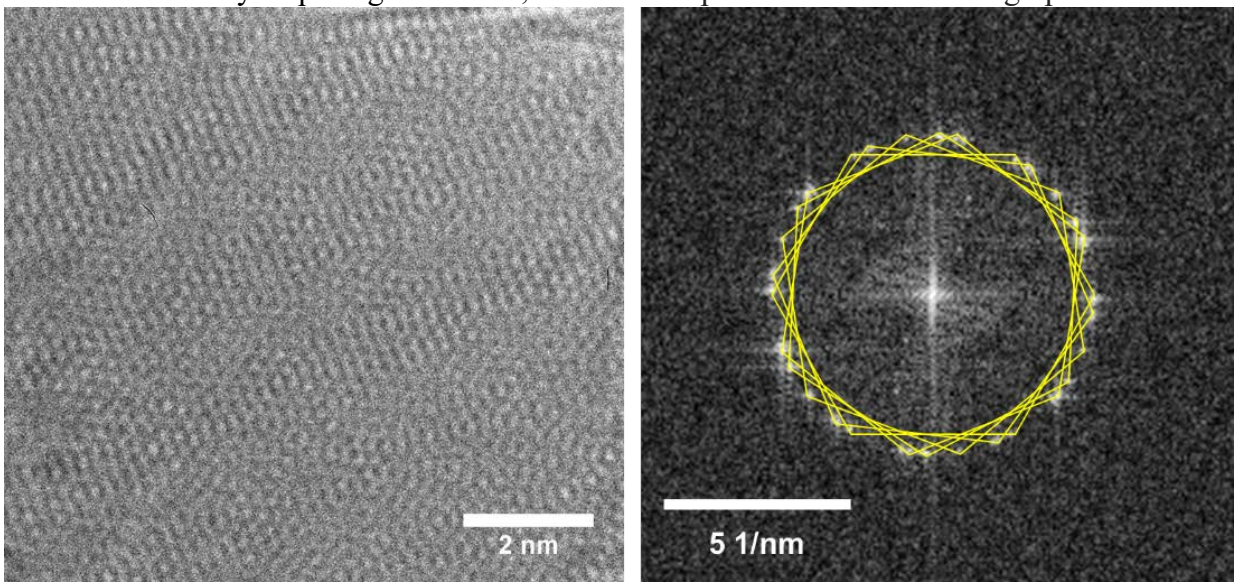

Figure A1.1. High-resolution TEM image of tFG sheet and FFT. FFT is composed of 5 sheets with 6-fold symmetry.

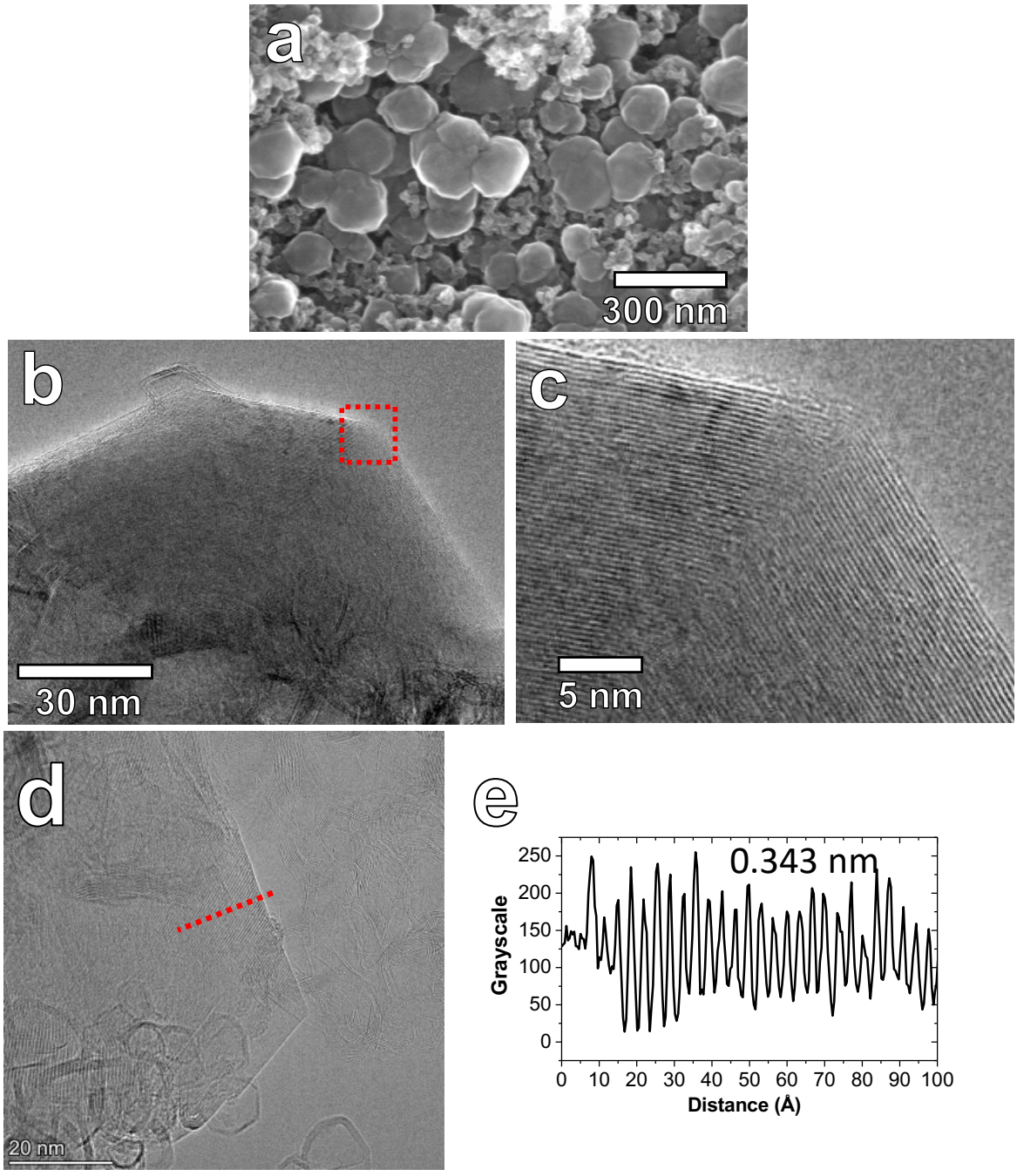

Figure A1.2. (a) SEM image of faceted FG spherical particles. (b-d) TEM images of particles. (e) Line scan showing interlayer spacing.

Fitted Raman spectra

Figure A1.3 reports analyzed Raman spectra for tFG sheets. The TS1 and TS2 peaks confirm that the material is turbostratic. The FWHM and peak positions are inset in the image. Importantly, the

G/TS ratio is only ~ 55, indicating the TS1 and TS2 peaks are very pronounced. The 2D peak is centered at 2700 cm^{-1} and can be fit with a single Lorentzian peak. The FWHM is 16.4 cm^{-1}. **Figure A1.4** reports the analyzed Raman spectra for the wrinkled graphene morphology. The TS1 and TS2 peaks are absent. The high curvature of this material may quench this peak since XRD suggests that the material is indeed turbostratic as well. The 2D peak is centered at 2695 cm^{-1} and is composed of multiple Lorentzian peaks and the FWHM is ~ 60 cm^{-1}.

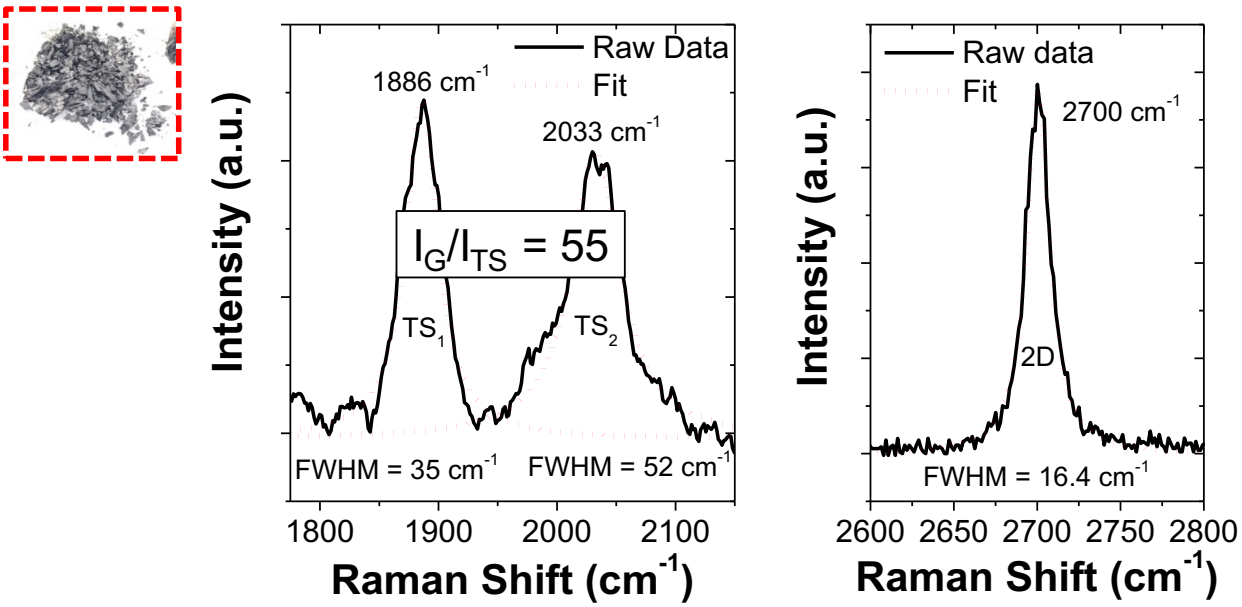

Figure A1.3. Raman spectra for TS1 and TS2 peaks as well as 2D peak for tFG sheets.

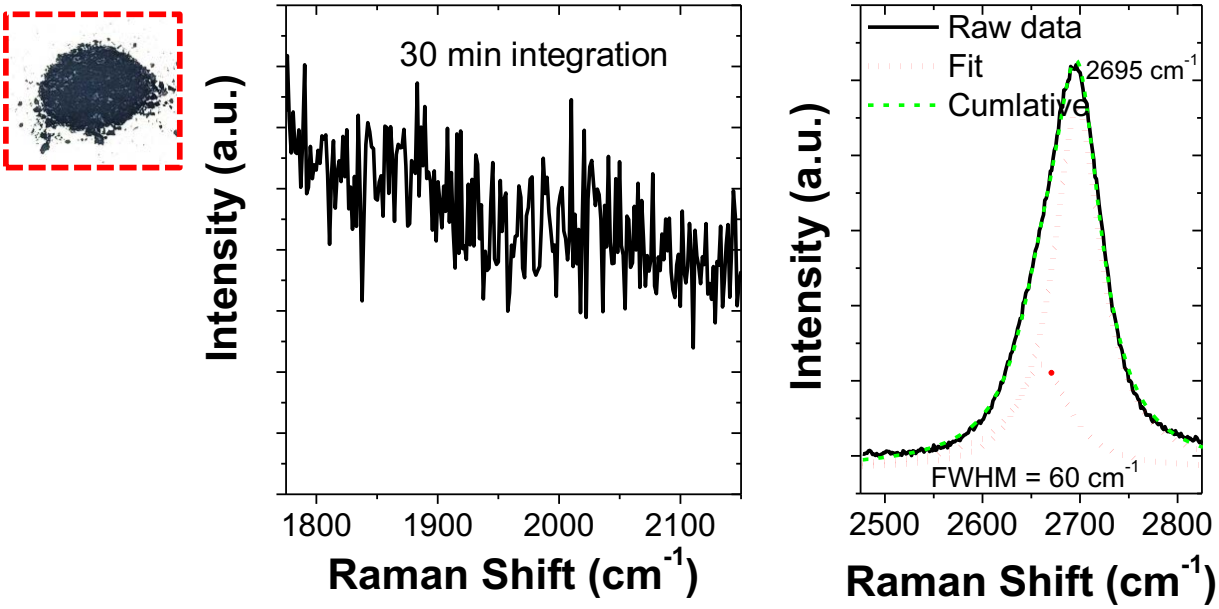

Figure A1.4. Raman spectra for TS1 and TS2 peaks as well as 2D peak for wrinkled graphene sheets.

TFG crystals

When forming FG, gray tFG crystals typically form across a bed of carbon. These crystals contain many layers of tFG that are not yet exfoliated. **Figure A1.5** shows SEM images of a crystal that was cross sectioned with a Ga^+ beam. The tFG layers extend for 10's of microns. Beneath these layers exist more tFG sheets (**Figure A1.5d**), which suggests large quantities of the material is converted to tFG sheets.

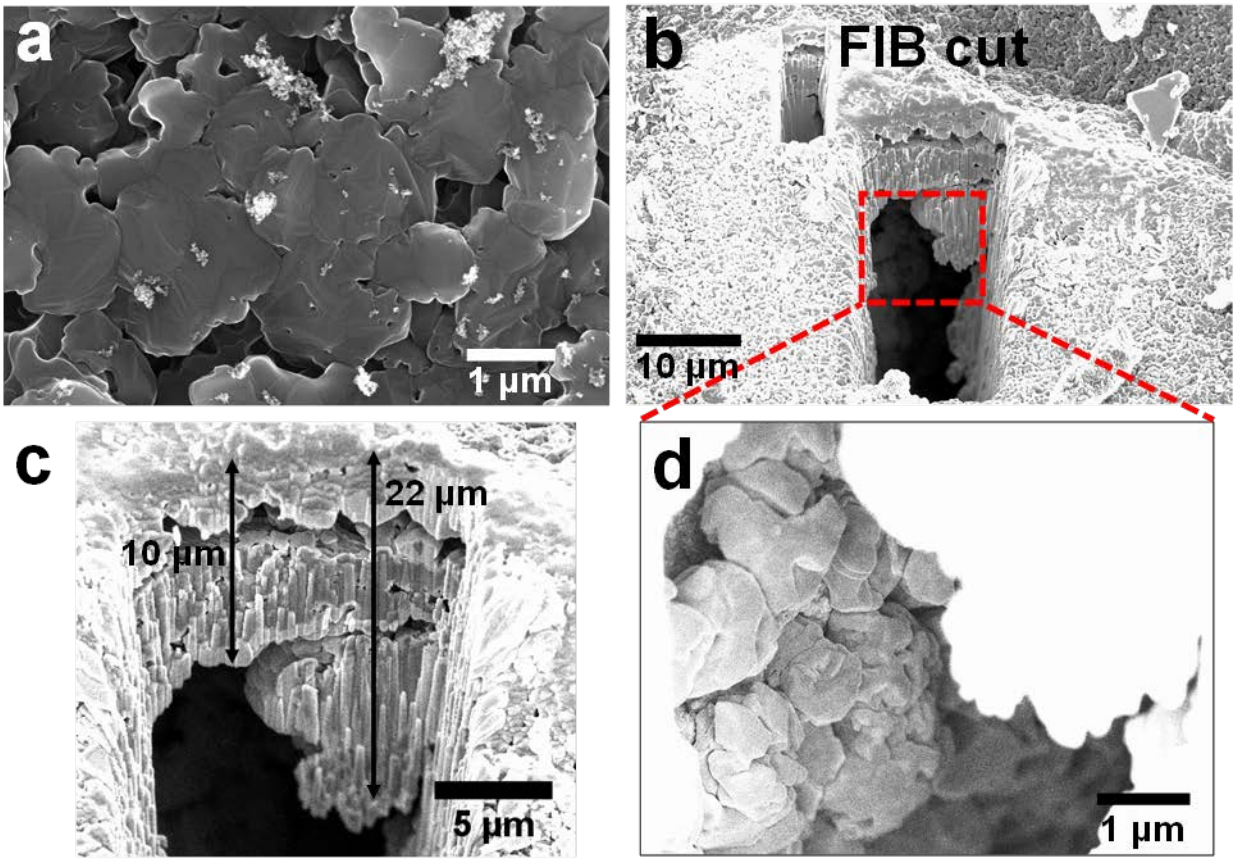

Figure A1.5. (a) SEM image of grey FG particle from CB source. (b) SEM image of FIB cut into FG. (c) Measurement of FG thickness. (d) SEM image inside of cut regions showing more turbostratic particles beneath cut.

Atomistic simulations

Initial structure preparation. Each of the characteristic CB centroid particles was constructed from individual graphitic flakes of arbitrary shape approximately 8–12 Å in diameter (**Figure A1.6a**) that are randomly positioned on concentric spherical surfaces following by random rotation and tilt (**Figure A1.6b**). Those spherical shells are combined into a centroid particle (**Figure A1.6c**), and additional individual carbon atoms are randomly positioned within the interaction range **(Figure A1.6d**). We combined eight centroid particles of various sizes (a slight deformation applied to some particles) into a large configuration adding graphitic walls and individual

randomly positioned carbon atoms constituting approximately 30% of the whole structure (**Figure 1.S6e**). The final configuration contained 85000 atoms. The size of the periodic cell was chosen to provide at least 15 Å of vacuum between graphitic walls.

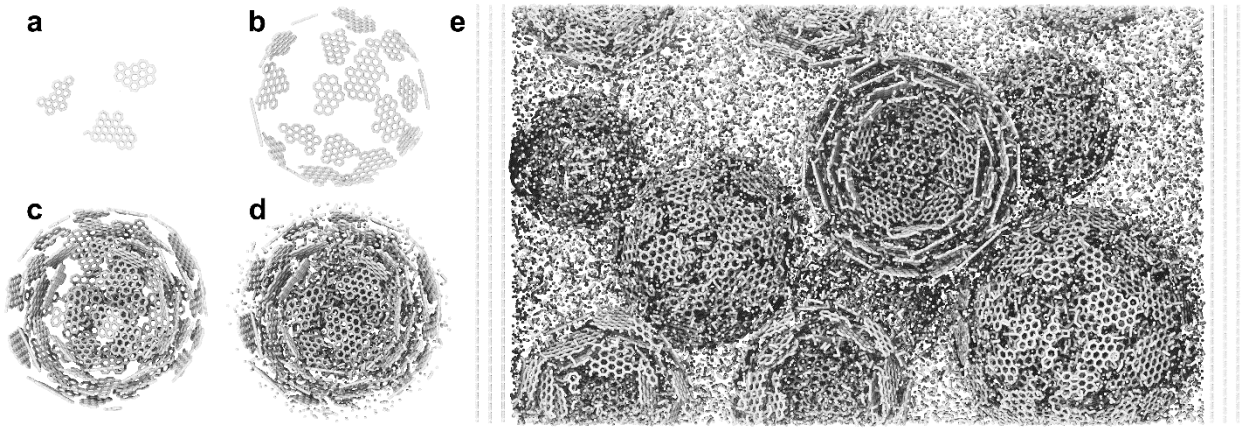

Figure A1.6. Creation of the initial configuration for atomistic simulations from individual graphitic flakes (a) arranged in spherical shells (b) that form centroid particle (c) with the addition of individual carbon atoms (d). The final configuration includes eight centroid particles, graphitic walls, and approximately 30% of individual randomly positioned carbon atoms (e).

Atomistic simulations were performed using AIREBO potential for a balance between computational cost and accuracy. Initial structure first underwent geometric optimization (some shrinkage in horizontal direction allowed for necessary change in atomic configuration) and then was subjected to preliminary annealing at 1000 K for 5×10^{-9} s to eliminate irregularities caused by the structure creation protocol.

Finally, the system was heated to the target annealing temperature with a heating speed of 0.5×10^{-12} K s^{-1} using a Nose–Hoover thermostat (canonical NVT ensemble) with a temperature damping parameter of 0.025×10^{-12} s. The structures were held at the target annealing temperatures for ~ 125×10^{-9} s (see temperature profile shown in **Figure 41.b**).

Structural characteristics were collected every 10 steps of the molecular dynamics simulation. Graphitization fraction was calculated as a ratio between carbon atoms in sp^2 configuration over the total number of atoms (graphitic walls were excluded from the characterization) – **Figure 41.c**. Additionally, graphitization fraction was calculated separately for atoms within centroid particles (**Figure A1.6d**), and the individual atoms randomly positioned around centroids (can be seen in **Figure A1.6e**). Herman's orientation function θ was employed to quantify alignment within the structure. Computed as $\theta = (3\langle\cos^2\alpha\rangle - 1)/2$, where α is an angle between the local direction of the graphitic plane and the characteristic direction. The local direction was calculated for plane formed by each sp^2 carbon atom and each combination of two of its neighbors and averaged. Generally, complete alignment with the characteristic direction would result in $\langle\theta\rangle = 1$, while alignment with the direction perpendicular to the characteristic direction should have $\langle\theta\rangle = -0.5$. To account for alignment to the plane of the graphitic walls, we chose a characteristic direction to be perpendicular to it (horizontal). Interestingly we did not observe a significant change in the alignment of the local graphitic directions nor did they become parallel to the graphitic walls nor

otherwise indicating that thermal annealing alone cannot be a cause of the structural directionality observed in the experiments.

Effect of FJH flash duration

Figure A1.7 shows image analysis used to estimate the composition of tFG sheets and wrinkled graphene. The tFG sheets appear as gray crystals, whereas the wrinkled structure appears black. Image thresholds were applied to determine the amount of gray and black material and the area of each species was used as an approximation of the composition of a batch of FG.

Figure A1.8 reports SEM images and representative Raman spectra for tFG sheets (gray crystals). Short pulses (10 ms) do not result in the widespread formation of tFG sheets. A percolating network of tFG is shown to form from 30– 50 ms, and the Raman spectra exhibits a high 2D/G ratio indicative of tFG. Extended FJH duration (200 ms) results in the formation of a continuous layer that exhibits Raman spectra consistent with graphite. Therefore, long FJH duration gives sufficient time for AB stacking and should be avoided if the intention is to form tFG.

Figure A1.9 shows SEM images and Raman spectra of the wrinkled graphene morphology (black powder) from a batch of FG. The morphology does not substantially change with various FJH flash durations; however, Raman spectra reveals that the material becomes more graphitic with increasing flash duration. This is suggested by the pronounced 2D peak and the reduction of the D peak. The residual presence of the D peak is likely due to bending of the wrinkled graphene sheets.

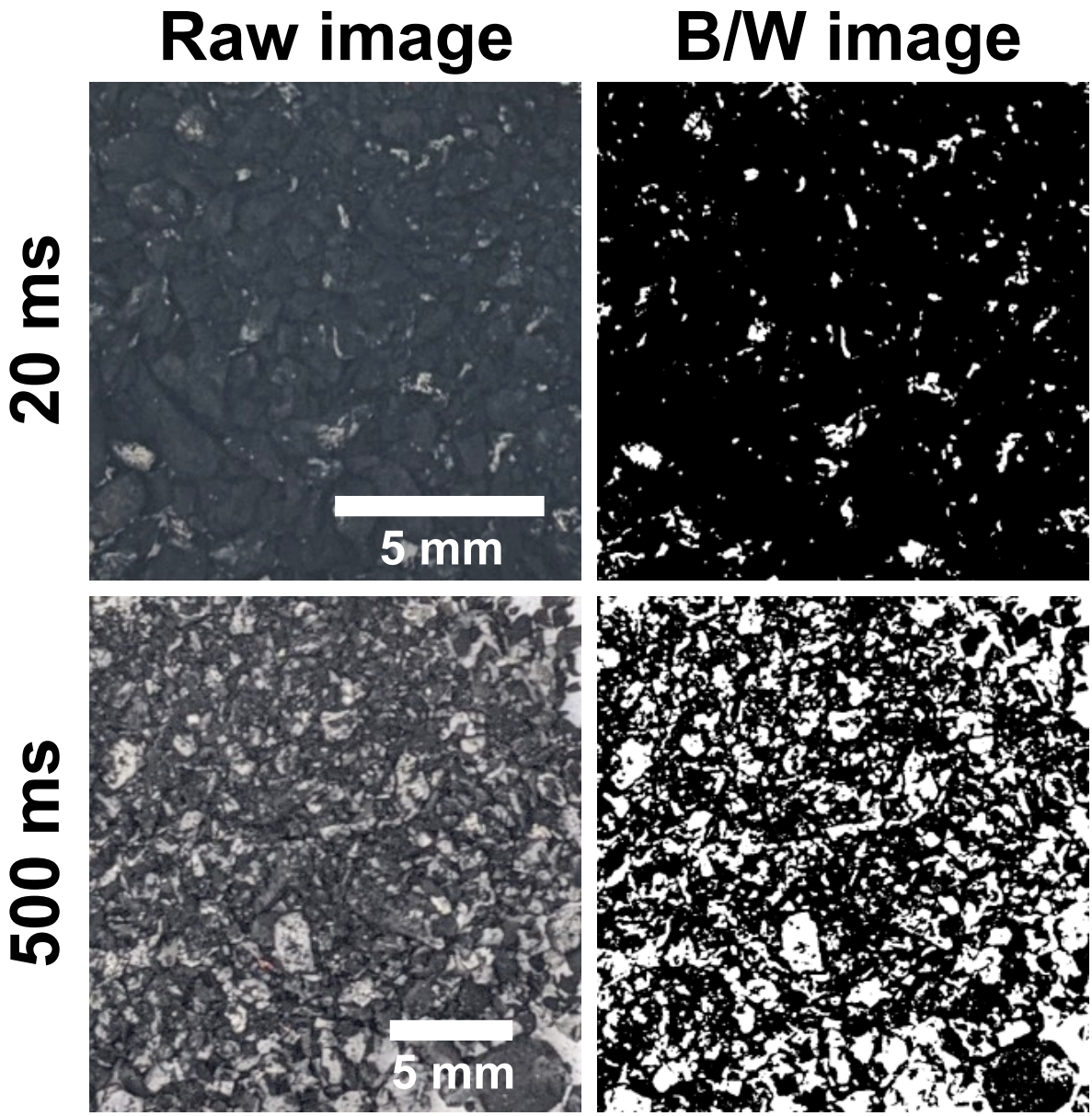

Figure A1.7. (left) Raw images and (right) processed images of FG at 20 and 500 ms flash duration.

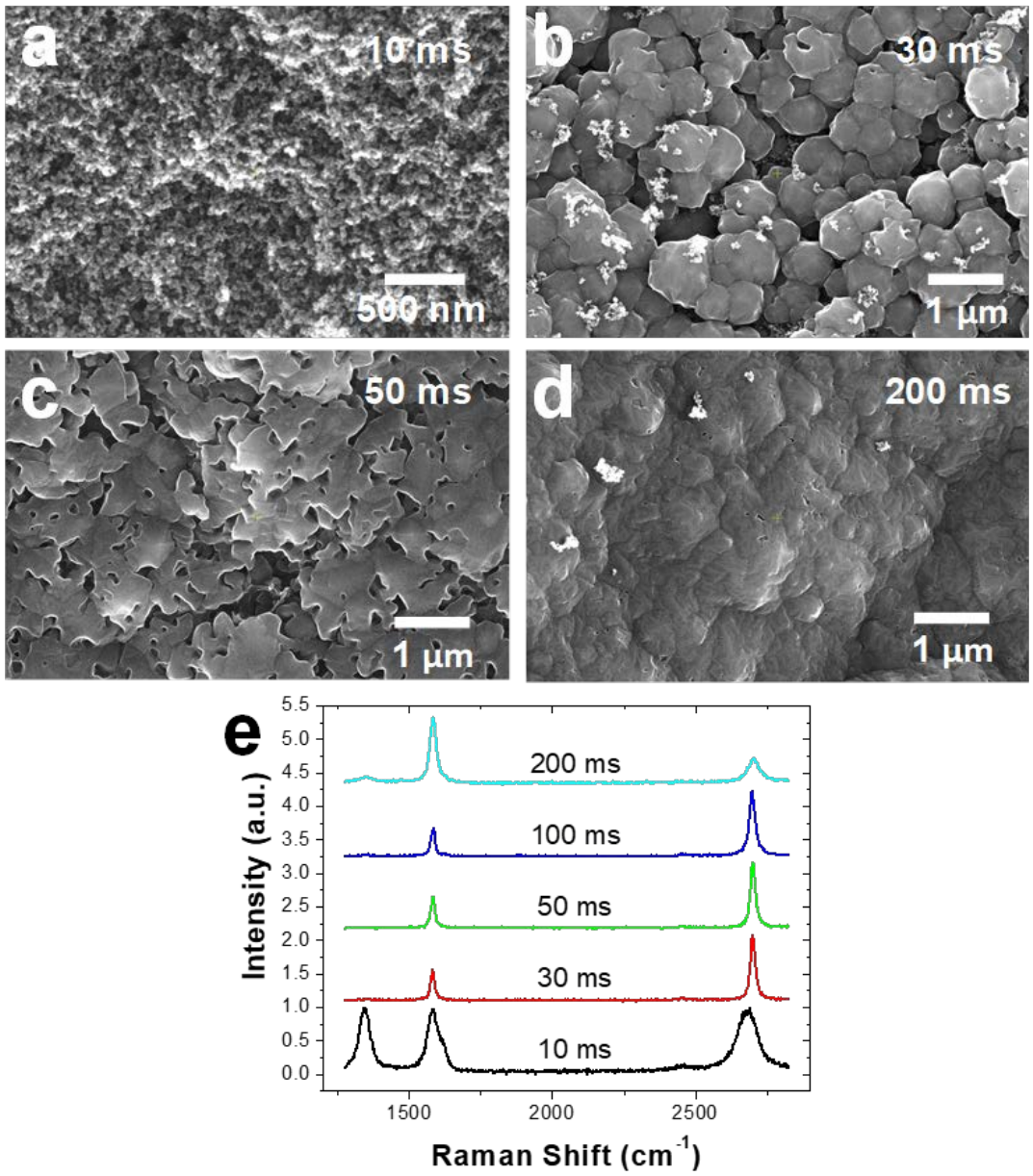

Figure A1.8. (a-d) Images of gray crystals as a function of flash duration. Flash voltage was 120 V. (e) Representative Raman spectra of grey particles.

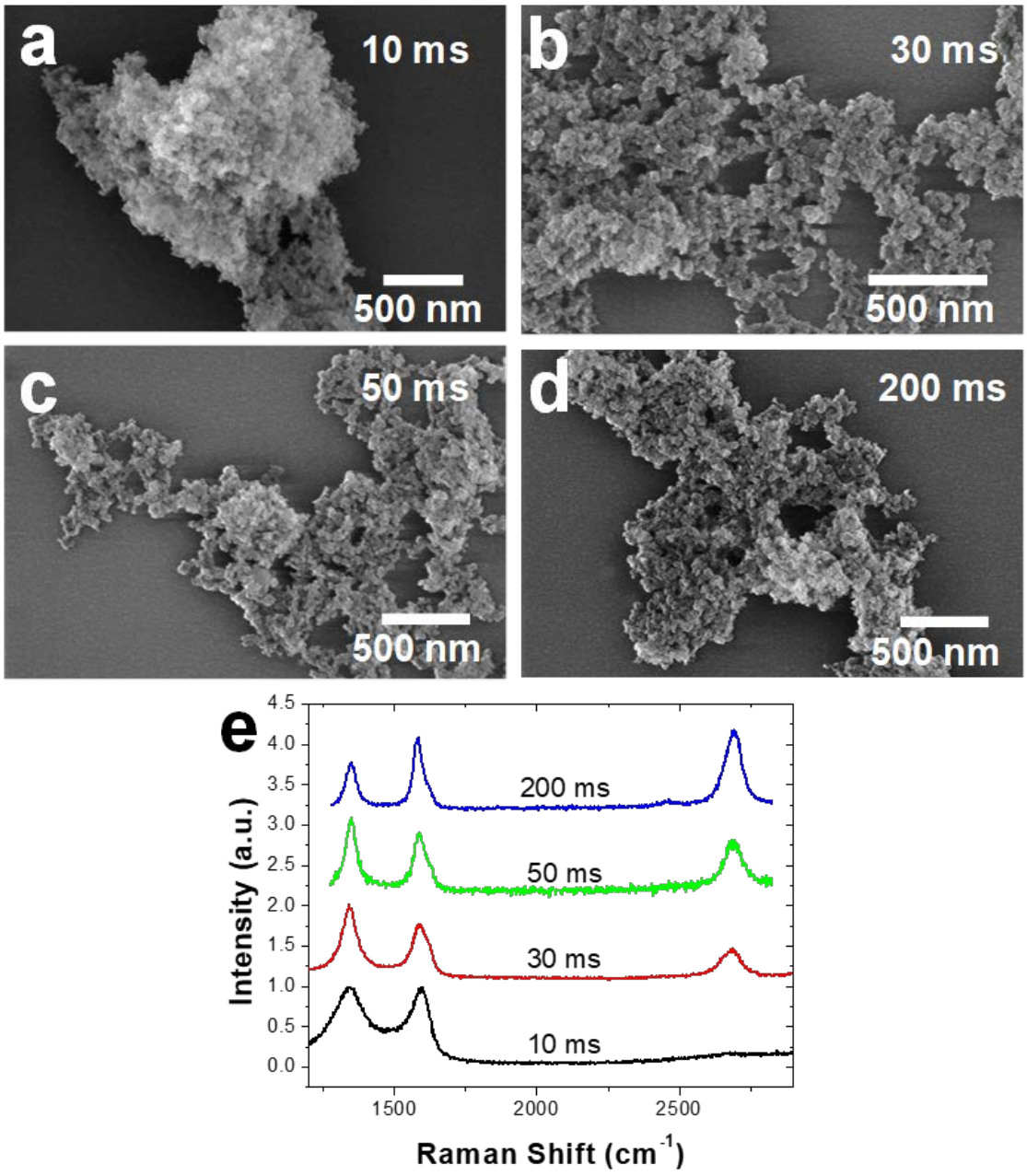

Figure A1.9. (a-d) Images of fine black FG powder as a function of flash duration. Flash voltage was 120 V. (e) Representative Raman spectra of fine black FG power.

SEM images and Raman spectra of tFG sheets

Figure A1.10 shows SEM images of tFG sheets. This material is characterized by a faceted surface and a visible layered structure.

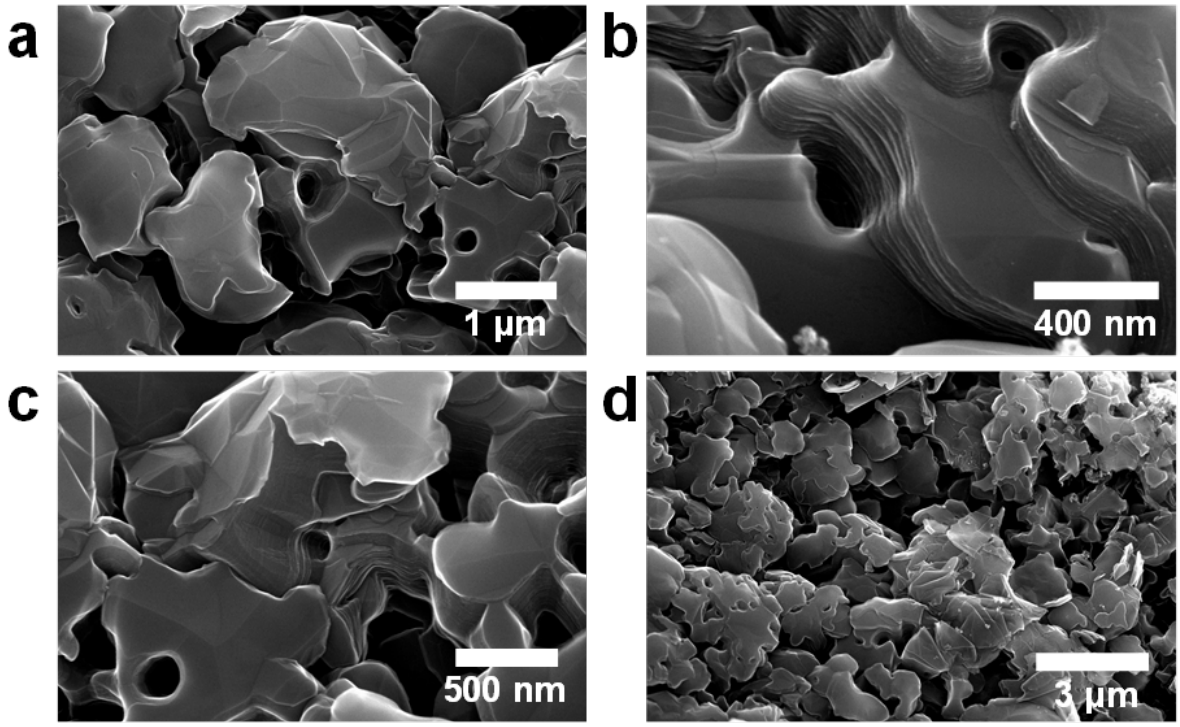

Figure A1.10. Various images of tFG sheets.

Figure A1.11 reports SEM images and Raman spectral mapping of tFG. Turbostratic crystals have pits that may indicate that the carbon source for crystallization originated from the bed of carbon particles on top of which that material crystallizes (**Figure A1.11a**). Smooth stacks of turbostratic material have high 2D/G ratio in the Raman map (**Figure A1.11b**). 2D/G ratios as high as 15.3 were observed, which is among one the largest values recorded in the literature.[1]

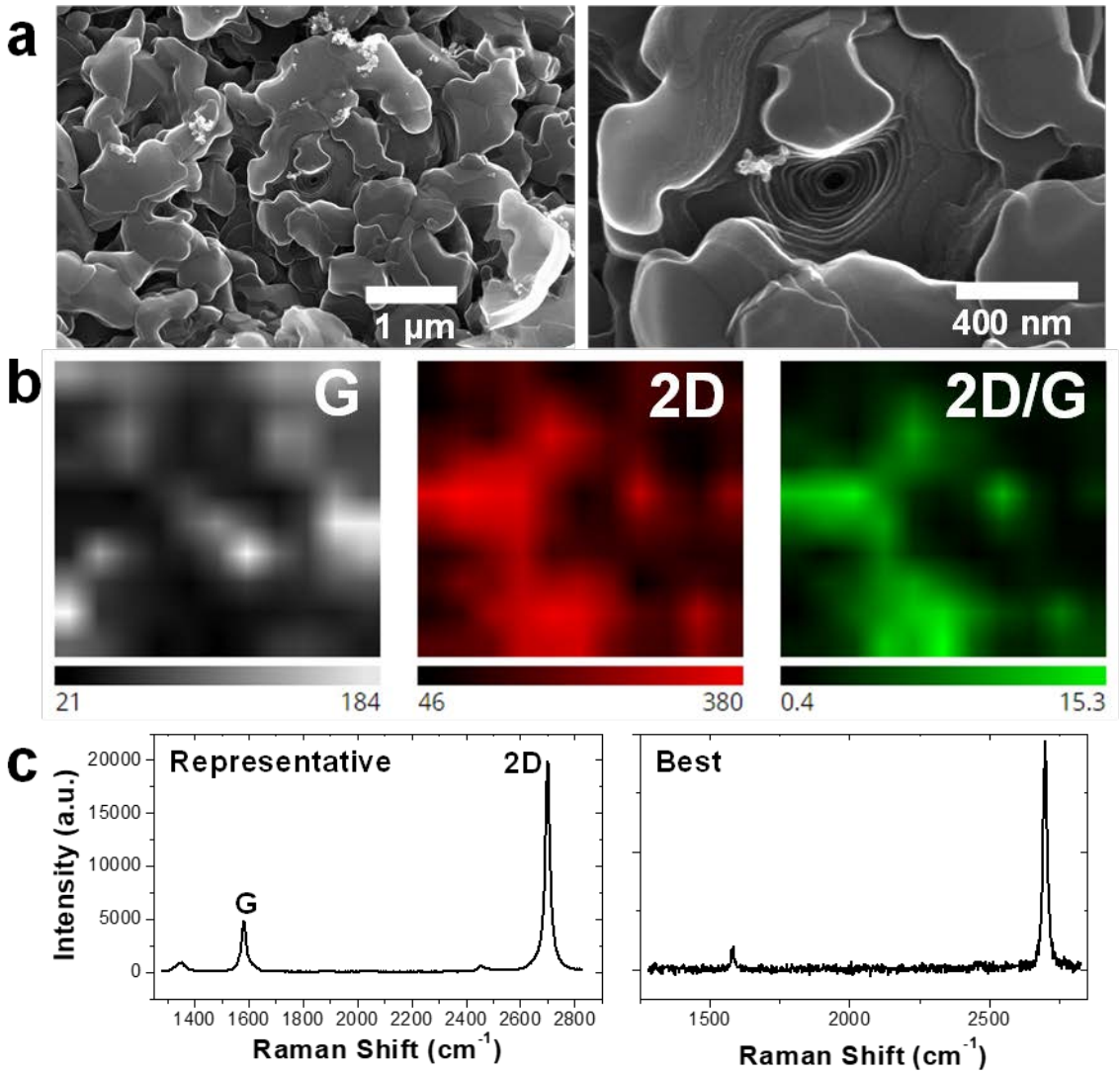

Figure A1.11. (a) SEM image of tFG. (b) Raman maps showing G, 2D, and 2D/G for a 20 x 20 μm area. (c) Raman spectra from representative and good regions.

Some regions of tFG exhibited a morphology that was readily exfoliating as shown in **Figure A.12a**. These regions have a representative 2D/G ratio of ~ 1.3, with regions having as high a ratio as 4.69. The small D-peak suggests that this material is high-quality graphene that was readily exfoliating and only loosely bound.

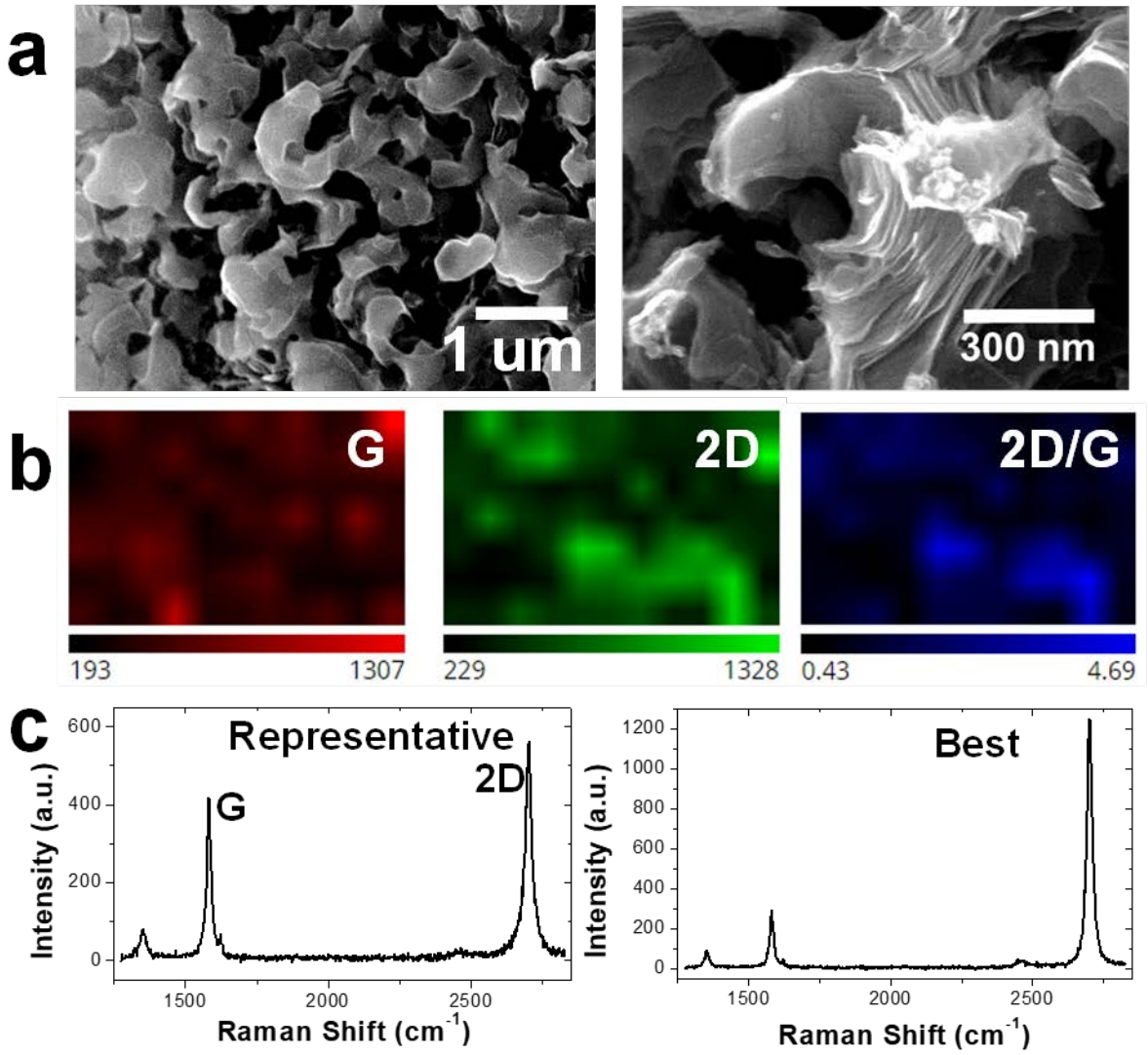

Figure A1.12. (a) SEM images of tFG from CB. (b) Raman mapping for a 20 x 20 μm area. (c) Raman spectra for this material.

Some regions from a batch of FG formed densely packed graphite polyhedral crystals (GPCs). **Figure A1.13** shows that the GPCs form faceted rods. The Raman spectra typically displayed a 2D/G ratio of ~ 1.0. **Figure A1.14** shows more images of various GPC morphologies ranging from cones to high aspect-ratio rods.

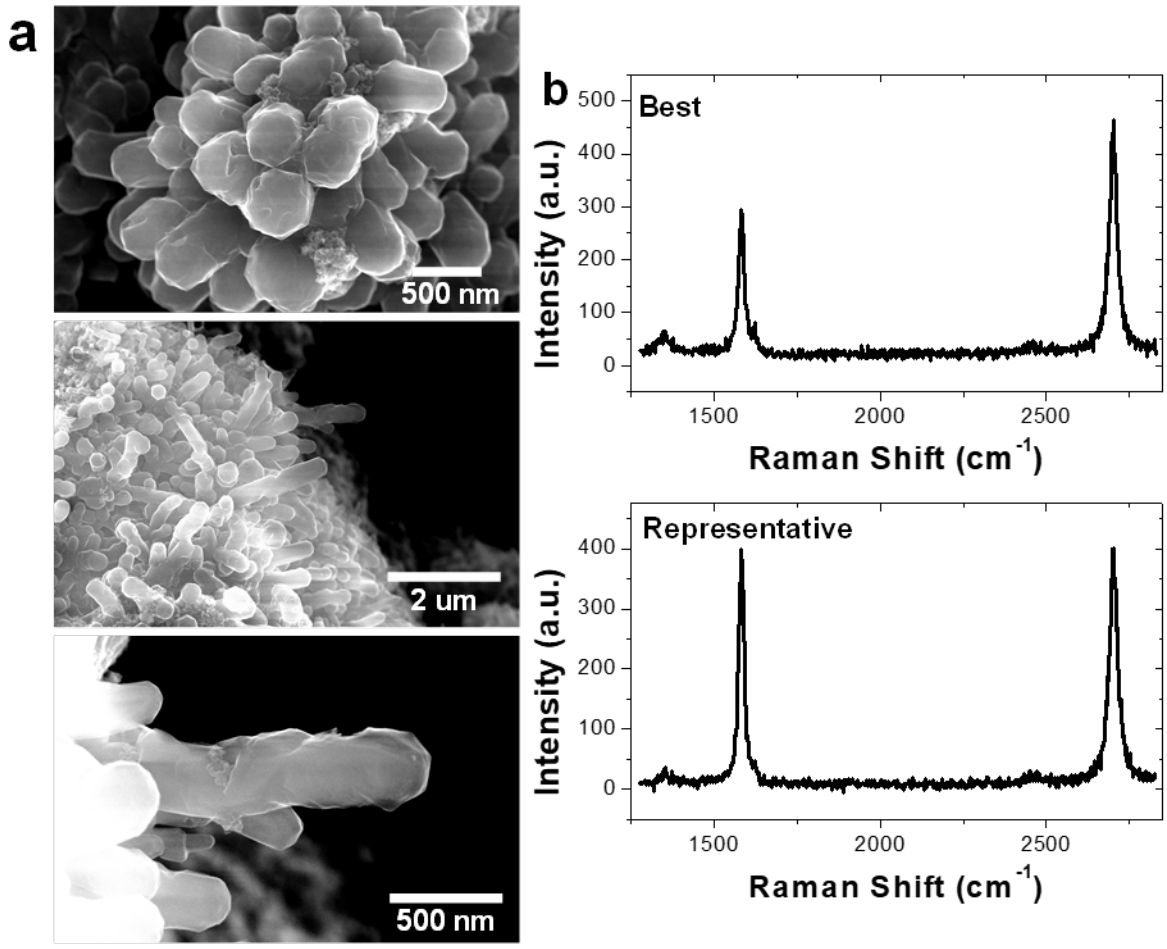

Figure A1.13. (a) SEM images of FG particles that exhibits rod-like structures with hexagonal faceted shape. (b) Typical Raman spectra for the FG particles.

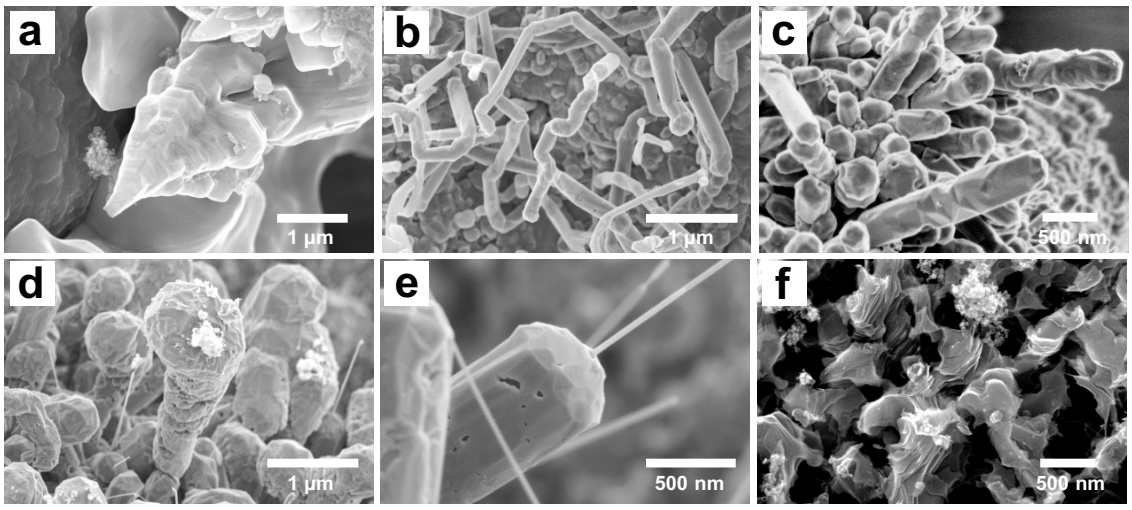

Figure A1.14. (a-e) SEM images of isolated graphite polyhedral crystals found on the surface of graphitized crystals. (f) SEM image of flakey, loosely bound FG.

Raman spectra of specific regions

To collect Raman spectra of specific morphologies, Si chips were patterned with alignment markers. This enabled single particles of FG to be found in a Raman microscope. **Figure A1.15** shows SEM images and the corresponding Raman spectra. This confirms that the crystal shown in the SEM image is composed of tFG sheets with high 2D/G ratio (~ 8). **Figure A1.16** reports an optical image, SEM image, and Raman spectra from a particle of wrinkled graphene. This material exhibits a 2D/G ratio of ~ 1 with a sizable D peak.

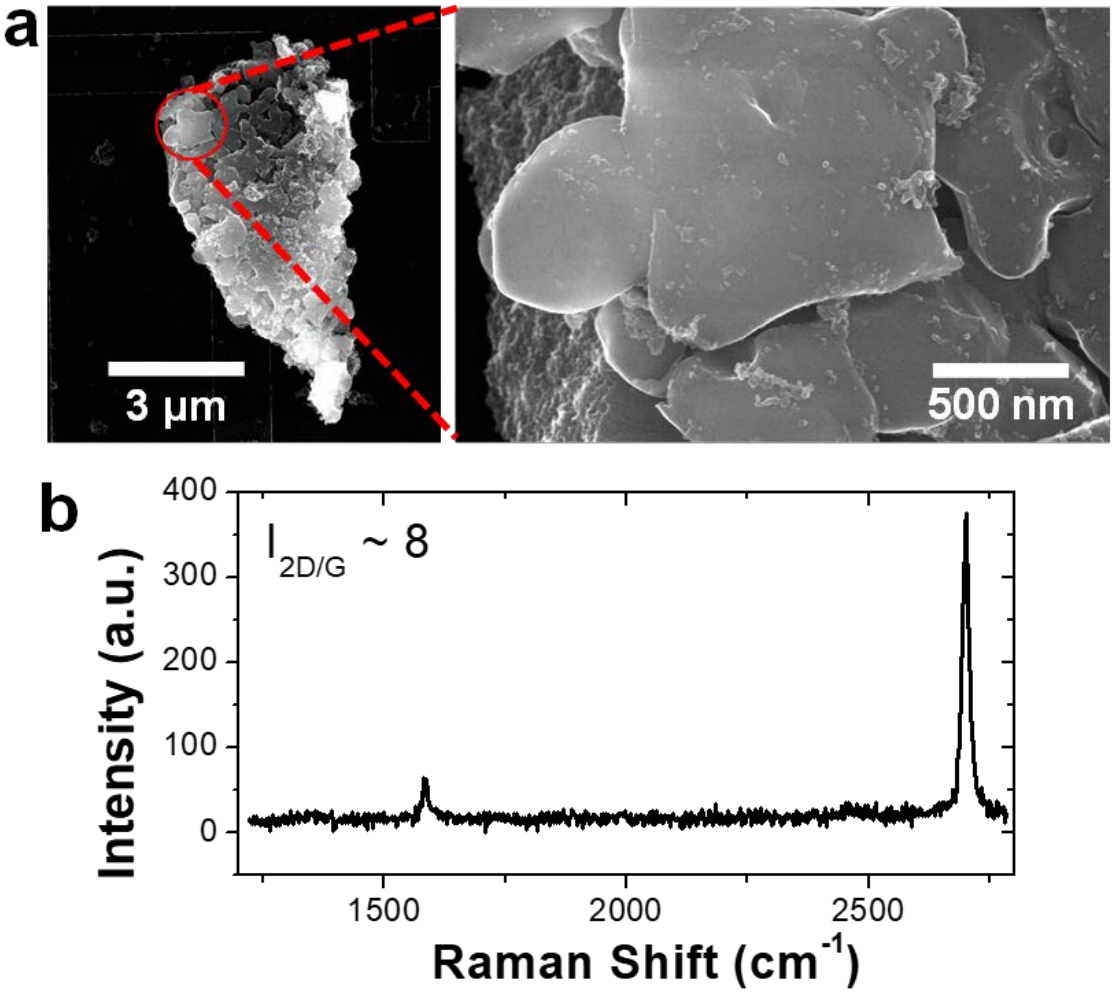

Figure A1.15. (a) SEM images of FG particle found with smooth morphology. Red circle indicates approximate location of 532 nm Raman laser. (b) Raman spectra for area shown in part a.

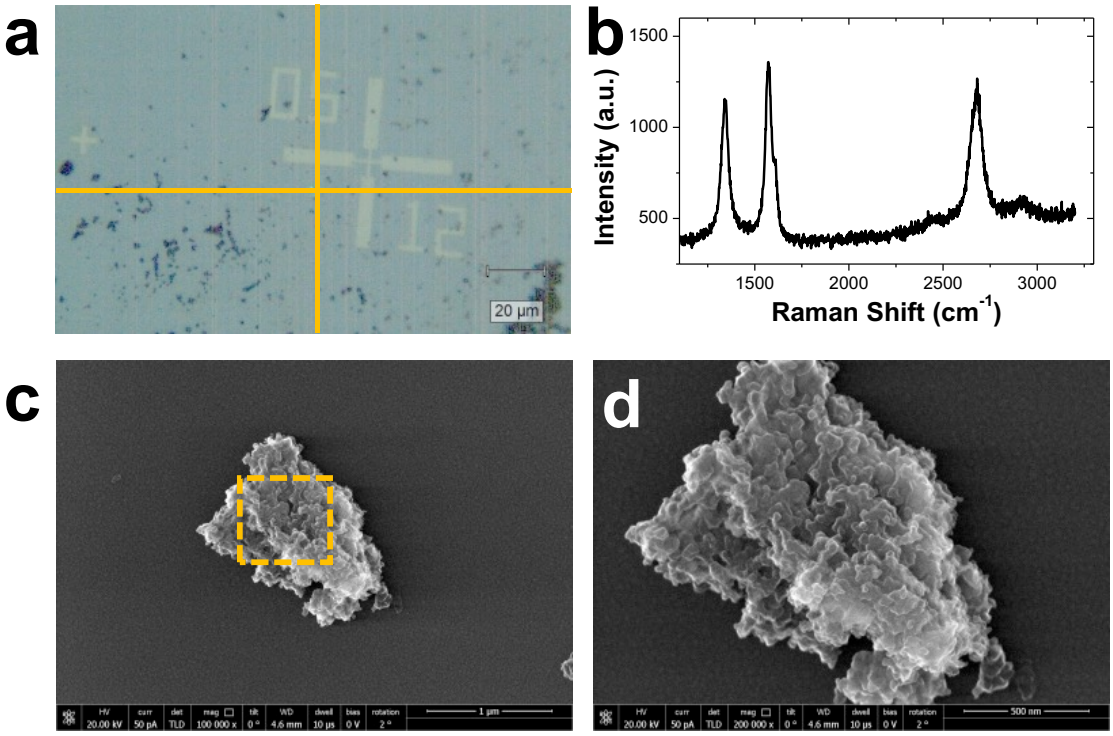

Figure A1.16. (a) Optical image showing FG location on alignment substrate. (b) Raman spectra of particle. (c-d) SEM images of FG particle.

Mechanism of flash graphene formation

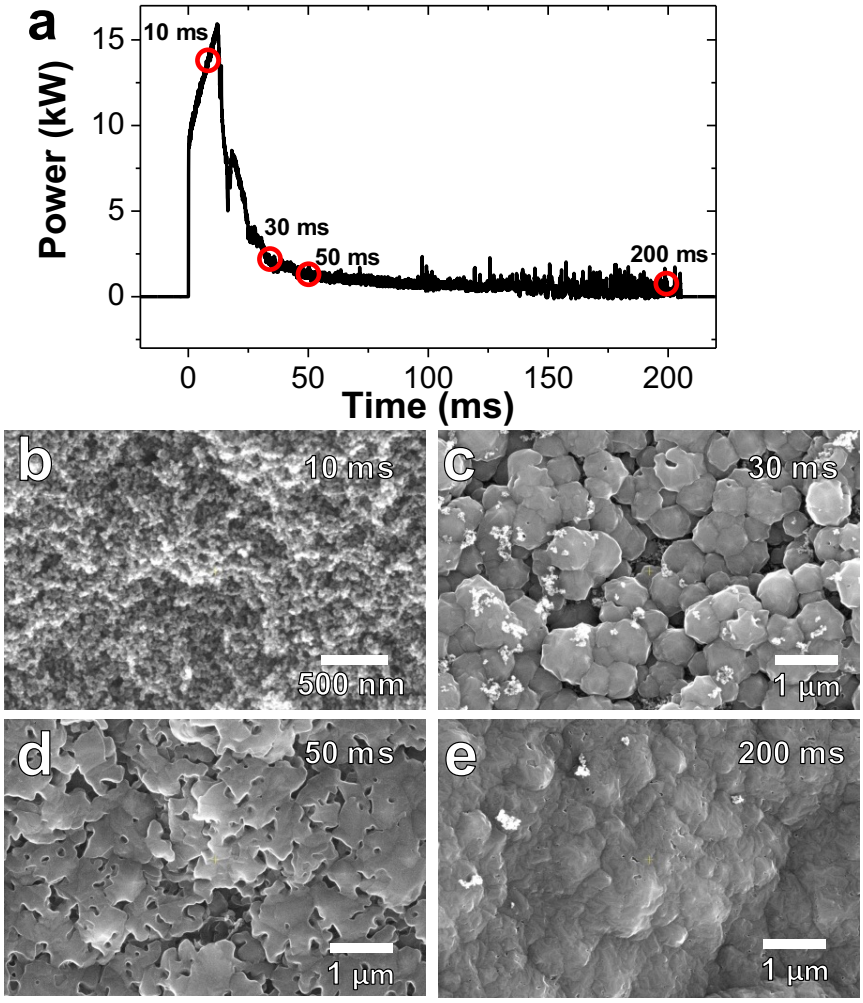

Figure A1.17. (a) Power dissipated in carbon black starting material as a function of flash duration. Representative SEM images of tFG crystals at (b) 10 ms, (c) 30 ms, (d) 50 ms, and (e) 200 ms.

Figure A1.17a reports the typical power dissipation *vs* time curve for a batch of FG which was flashed for 200 ms. A spike in power dissipation occurs after ~ 15 ms. The morphology of FG produced at various flash durations was observed and compared to this power dissipation plot in Figure 5a to propose a mechanism for FG formation. **Figure A1.17b** shows the typical morphology after a 10 ms flash. This material does not experience the peak power dissipation and therefore does not achieve the maximum temperature (~3000 K).[1] Raman spectra reveal incomplete graphitization of the starting material. At the peak power dissipation (~15 ms), we propose that the junction between neighboring carbon particles rapidly heats due to high interfacial resistance. This then causes the interfacial carbon to sublime, increasing the total resistance of the carbon particles, and reducing current and power dissipation at longer flash durations. Once carbon begins to sublime, the evidence suggests that faceted crystals of tFG form by 30 ms (**Figure A1.17c**) and

these crystals nucleate to a percolating layer of tFG sheets by 50 ms (**Figure A1.17d**). Flashing the material for 200 ms (**Figure A1.17e**) results in the formation of a continuous graphitic film, for which Raman spectra reveals that AB-stacking occurs, an indication that the material is no longer turbostratic. Previous work has shown that sublimed carbon will form turbostratic particles similar to those seem in **Figure A1.17c**.[2] Additionally, the point of peak power dissipation must be achieved in order to find the grey crystals of tFG sheets in the batch of FG. This suggests that it is critical to drive carbon sublimation for the tFG sheets to form.

Exfoliated tFG sheets

Crystals of tFG were placed on a gold substrate and subjected to shear force. This resulted in the widespread exfoliation of the material as shown in the SEM images in **Figure A1.18**. **Figure A1.19** shows a region on a tFG crystal that was exposed to shear force. The material is readily exfoliated and wrinkles. The weak adhesion can be attributed to the turbostratic nature of the material. **Figure A1.20** shows tFG and wrinkled graphene that was exfoliated on a Si surface. **Figure A1.21** reports SEM images and an AFM scan taken from the same region. The thickness of the tFG is less than the surface roughness of the Au substrate and suggests monolayer or few-layer exfoliation. Raman spectra of the exfoliated tFG (**Figure A1.22**) shows a 2D/G ratio indicative of high-quality graphene and the presence of a TS1 and TS2 peak suggests that it is multilayer and turbostratic.

The tFG can also be dispersed into a solvent such as Oleum for exfoliation. Drop cast sheets of tFG can be seen in **Figure A1.23**).

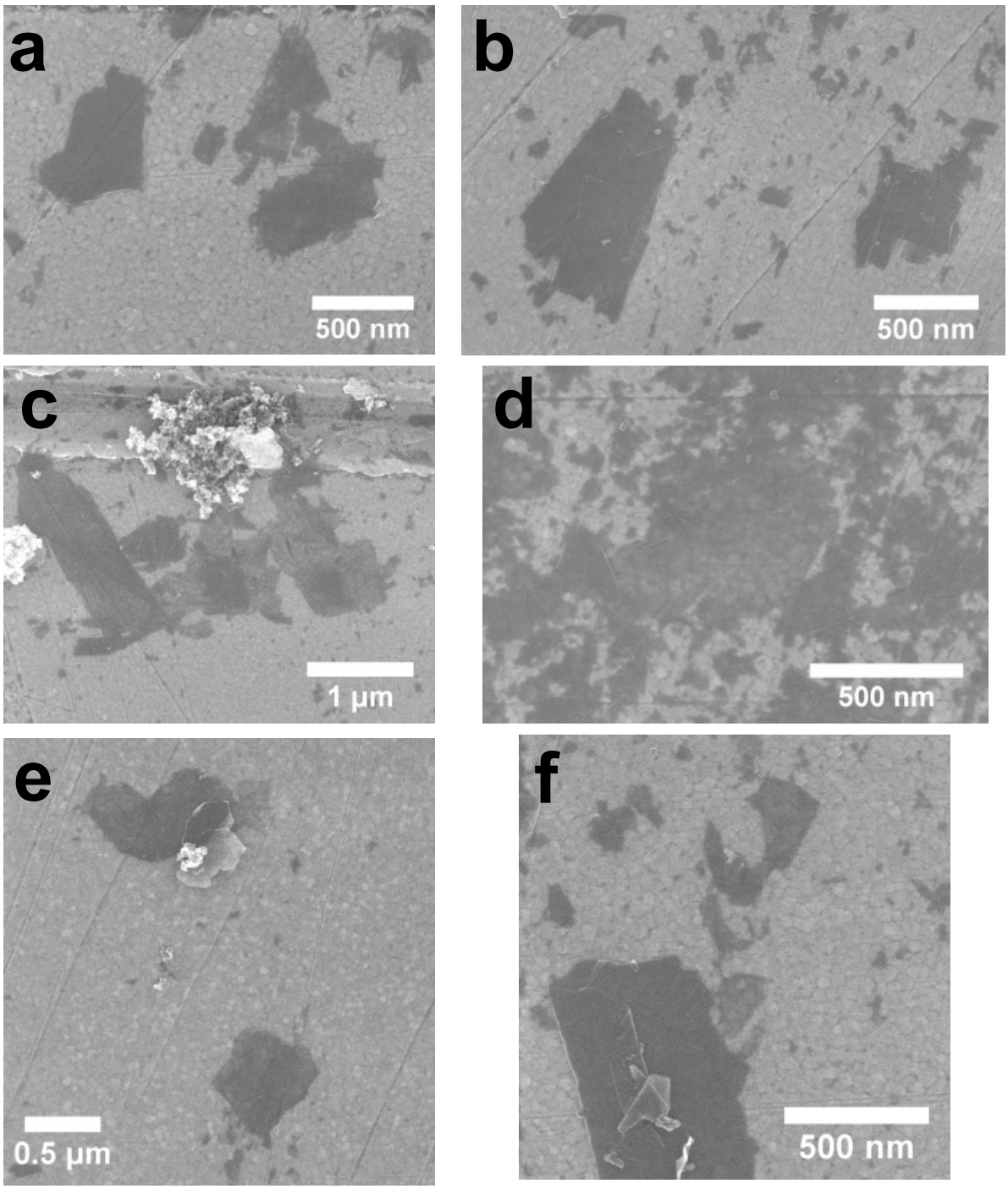

Figure A1.18. (a-f) Various SEM images of FG that were exfoliated onto gold.

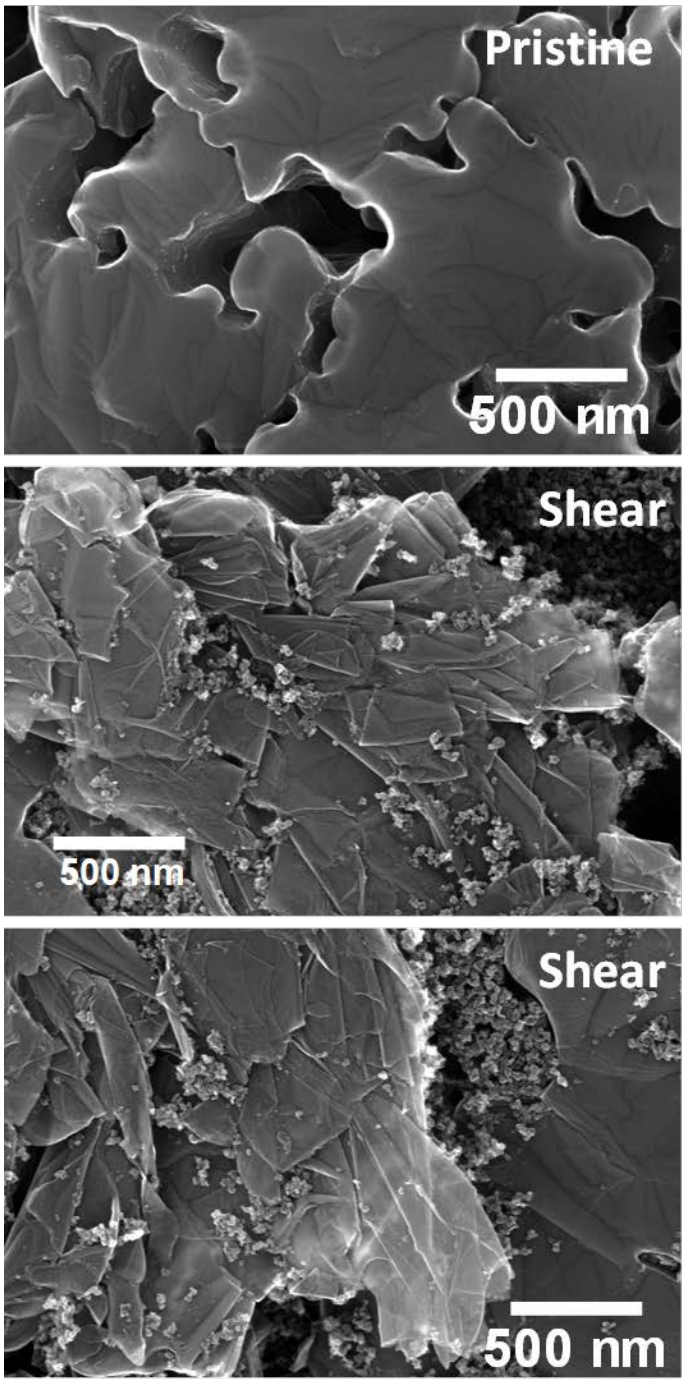

Figure A1.19. SEM images of FG that is (top) pristine and that has been exposed to (middle, bottom) mechanical shear.

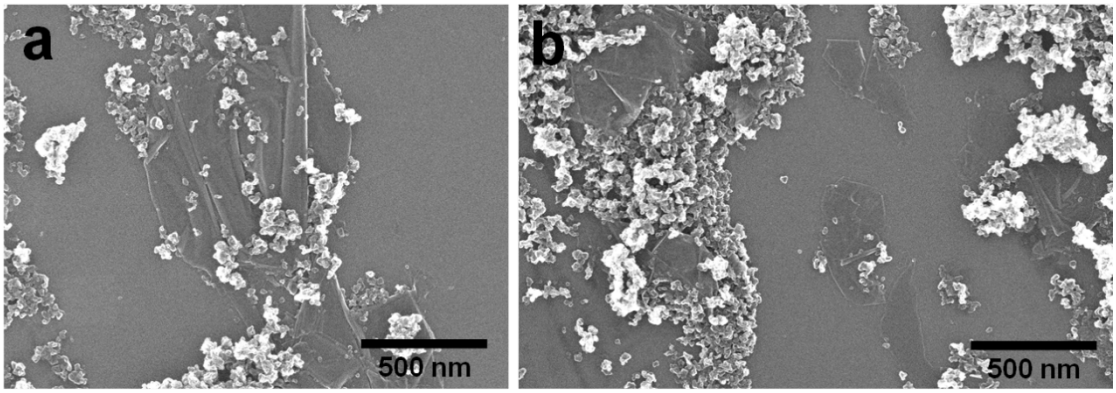

Figure A1.20. (a-d) SEM images of FG from carbon black that has been mechanically sheared between two silicon wafers.

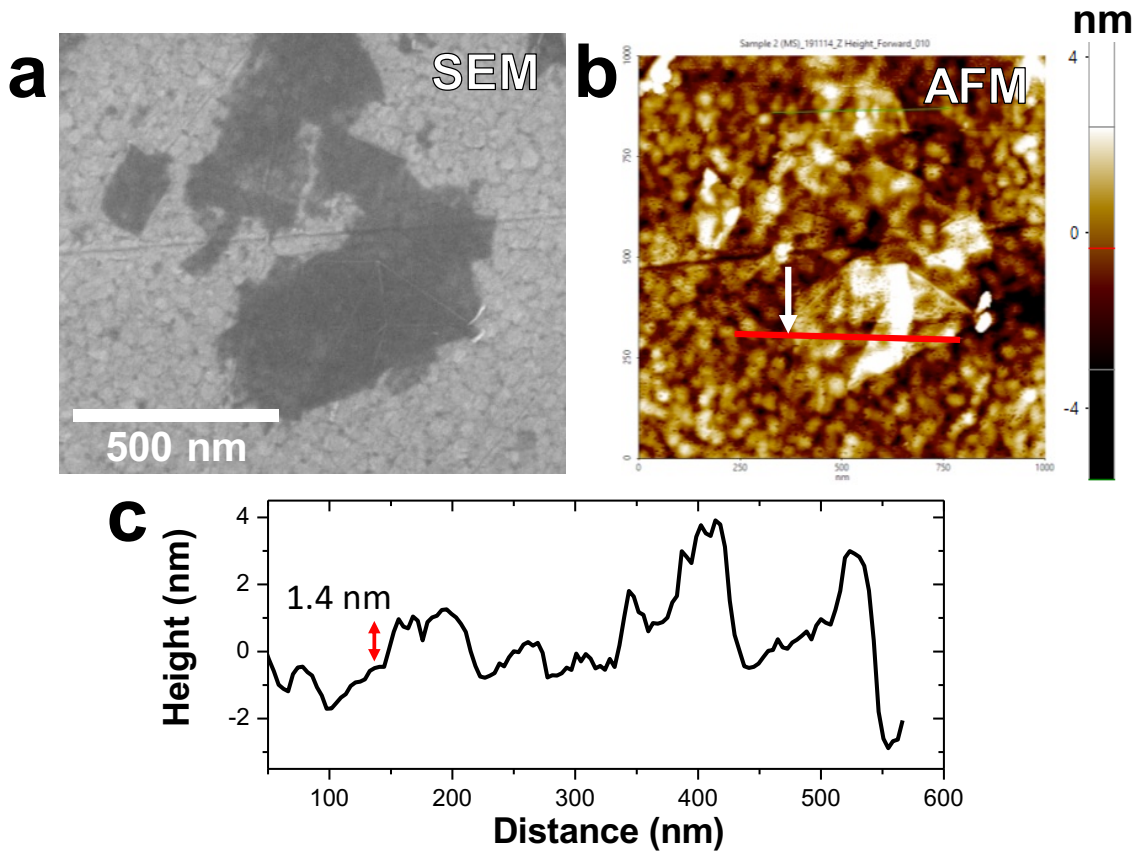

Figure A1.21. (a) SEM and (b) AFM image of a FG sheet. (c) Line scan from AFM showing sheet height of ~ 1.4 nm.

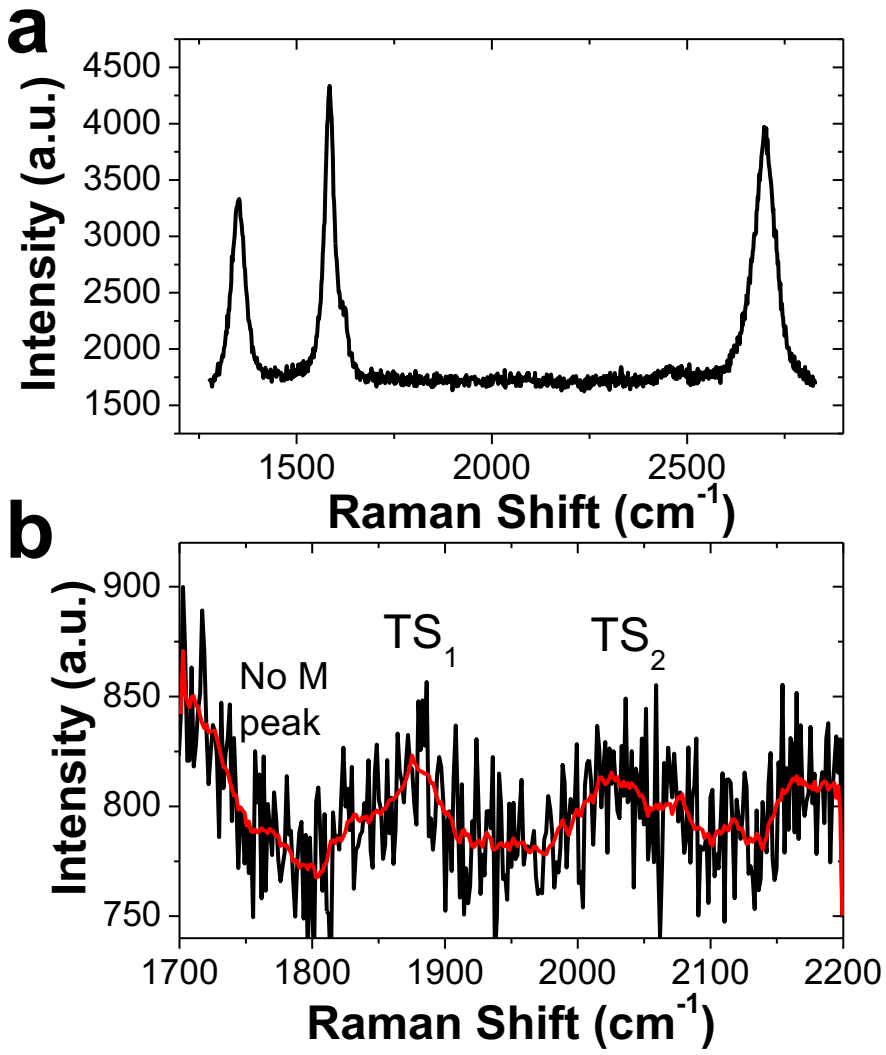

Figure A1.22. (a,b) Raman spectra of mechanically exfoliated FG on gold substrate.

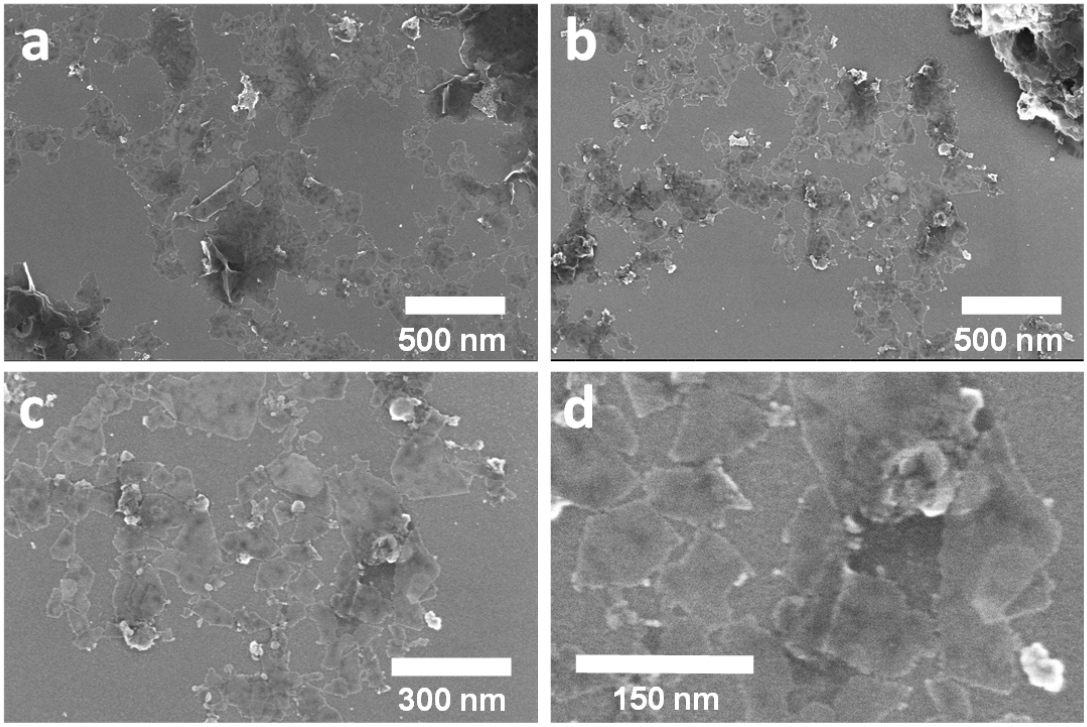

Figure A1.23. (a-d) SEM images of FG dispersed in oleum and dropcast onto Si substrate.

References A1.

1. Luong, D. X. et. al. Gram-scale bottom-up flash graphene synthesis. *Nature* **577**, 647–651 (2020).
2. Kokai, F., Ishihara, M., Koshio, A., Nakayama, A. & Koga, Y. Fabrication of some graphitic polyhedra and balloon-like particles. *Diam. Relat. Mater.* **16**, 1264–1268 (2007).

Scale-Up of the FJH FG Process 2.

As described in the Statement of Work, one of our tasks is to scale-up the production of the FG to a rate of 1kg/day. Here we detail our approach to develop the scaled-up process.

Sample Size Calculation

Table 2.1. First Design of Scale-Up Reactor for 10 g Flash, Sample Size Calculation

Batch size (g)	Cycle time (h)	Working hour	Total batch	Production per day (kg)
10	0.25	8	32	0.32
20	0.25	8	32	0.64
50	0.25	8	32	1.6
100	0.25	8	32	3.2

To fulfill the 1 kg/day goal set by the DOE, we will need at least 50 g/batch based on calculations shown in **Table 2.1**.

Table 2.2 Calculations for Scaling Up – Voltage and Amperage Needed for Each Batch Size.

Size (cm)	Area	Length	Weight (g)	Density		Length	Voltage	V square	Mass		Current
1.5	1.76625	2.1	5	1.348027		1	150	22500	5		500
2	3.14	3	12.69816			2	220	48400	12.7		865.9091
						9	466.6905	217800	97		3117.698
2x4	8	9	97.056			25	777.8175	605000	1011		19496.86
2x15	30	25	1011			60	1204.99	1452000	4853		60411.31
2x30	60	60	4852.8			200	2200	4840000	53920		367636.4
2x100	200	200	53920								

Using the parameters from the FJH reactions with sample size <1 g, in **Table 2.2** we calculated the parameters needed for achieving the production of 10-100 g product sizes. Calculations show that a 500 V and 3000 A capability system will be needed.

FJH System Design Including Circuit and Components

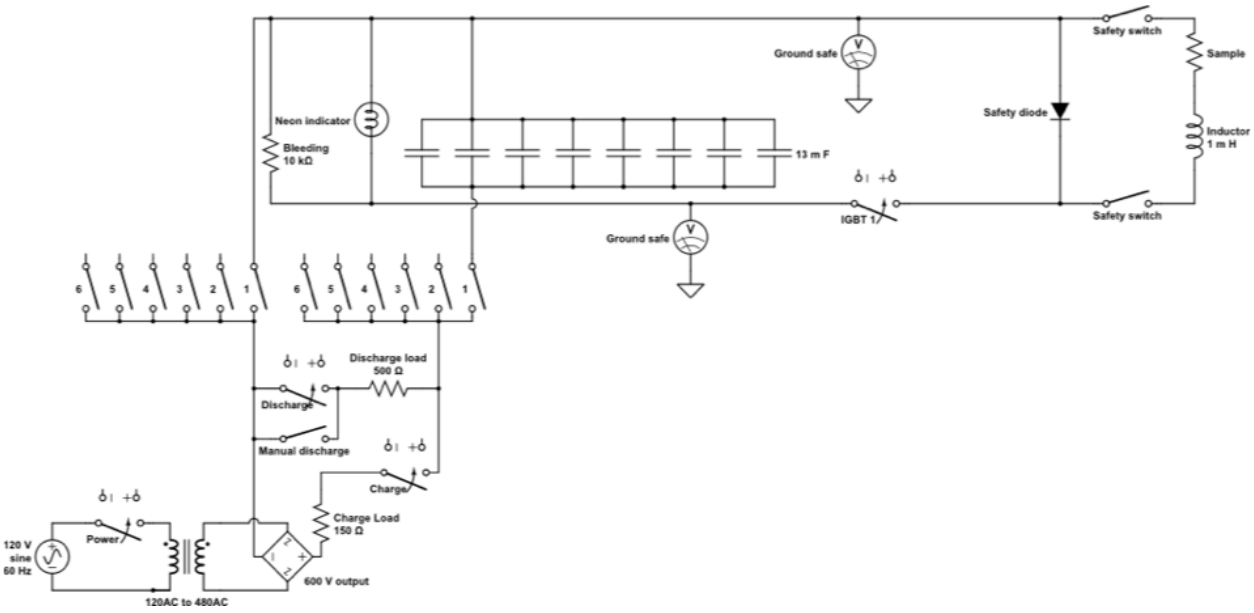

Figure 2.1. Circuit design for large scale FJH reactions.

There will be 6-12 banks of capacitors, each bank containing 8 capacitors as shown in **Figure 2.1**. All components after the transformer are floated and need to be contained without electrical exposure. The system will be controlled in the charge, discharge, and flash stages by a computer through an insulated DAQ. The user will be in safe distance from the whole system. The design is being checked by a Rice University certificated electrical engineer specialized with high power.

Capability of the various components

Table 2.3. Calculation of Number of Capacitors Needed.

Sample size (g)	Energy (kJ)	Voltage (V)	Capacitance (F)	Capacitor No
50	100-150	500	0.8-1.2	64-96
100	200-300	500	1.6-2.4	128-192

We learned that the energy for conversion to FG can be reduced as we progress to larger sample sizes. We are expecting an energy conversion of 2-3 kJ/g. With commercial capacitors, we will need ~96. Capacitors will be arranged into banks of 8. Calculation shows that, in a failure scenario when all 7 capacitors dump their energy into one, the failed capacitor should not explode. Capacitor banks are separated from each other with circuit breakers to prevent cross-bank discharge.

Insulated Gate Bipolar Transistor (IGBT) switches

Each capacitor bank will have its own IGBT switch. Each switch is rated 900 V 600 A continuous current. The first system built will have 6 banks with 6 switches. Total current rating will be 3600 A, matched with the current rating from calculation.

Inductor and Safety diode

An inductor is crucial in the FJH system since it prevents a spike current that could destroy switching components. The increase in current from 0-3000 A will be limited to >1 ms; this presumes the inductor inductance > 0.3 mH. However, the kick back voltage from the inductance when shutting off the current and the oscillation caused by inductor needs to be avoided. Therefore, a reverse diode is put parallel to the inductor and sample for dual purposes: prevent the oscillation and kick back voltage. The diode is rated 3000 A.

Wiring

To carry such a large current, we will use AWG #1/0 for the main wire that conducts 3000 A in a short amount of time. AWG #6 wire will be used to conduct current from single capacitor bank.

Containment

The system will be contained inside the fume hood. The fume hood is designed for shock absorption and ventilation needed in case of failure. Calculation shows that even if all of the capacitors are used to heat up the air inside the fume hood, the temperatures will only increase ~30 °C, not enough to cause an explosion.

Charging

A transformer with a bridge rectifier will be used to provide DC charging voltage. The load resistor is important to limit the charging current. A circuit breakers bank is employed to prevent the high flow back current to the transformer as well as between capacitor banks.

Discharging

The discharging resistor allows the capacitor to be fully discharged in 10 min and the bleeding resistor in each capacitor bank allows 1 h of passive discharge.

Data Acquisition Computer (DAQ)

A National Instruments (NI) DAQ 6218 will be used for isolated DAQ and control of the FJH system. All charging, discharging, and flashing is controlled by this DAQ.
The computer is placed a safe distance from the system.

Grinding of Coal

It was found that the coal needed to be ground into finer particles and possibly formed into a pellet before being flashed. This would ensure the best contact between particles and the most efficient flash. A sample of coal was sent to MSE, a company that sells planetary mills, right before the shutdown of the labs on March 20. The company was successful in grinding the sample to micron size. Based on these results, a laboratory scale planetary mill (shown at left) was ordered. The analyses of the starting coal and final mill product are shown in **Figure 2.2**.

Research During COVID Shutdown

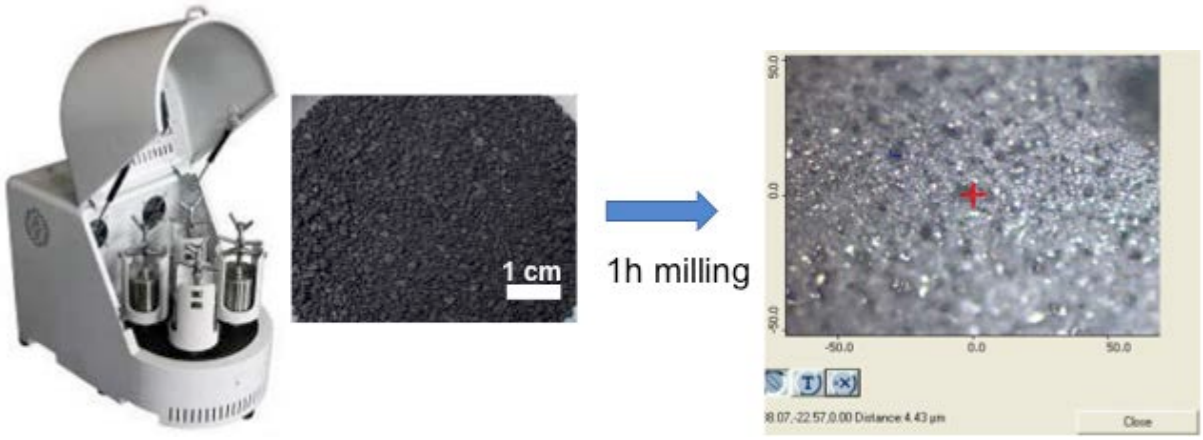

Figure 2.2. The MSE planetary mill and the results from grinding coal.

The research labs were closed by Rice University on March 20 due to the COVID-19 pandemic. This caused delays in meeting goals, as communicated to the Program Manager. The labs reopened in Rice Phase 1 at partial capacity on May 26 with rotating laboratory work shifts due to extreme social distancing of 500 sq ft per person of laboratory workspace. Rice Phase 2 opening occurred August 3 with continued COVID precautions such as taking temperature before reporting to work (and staying home if ill), wearing masks, full gloves, and lab coat always while in the lab, 250 sq ft of lab space per researcher, and other precautions as required by the University.

Flash Graphene Energy Efficiency

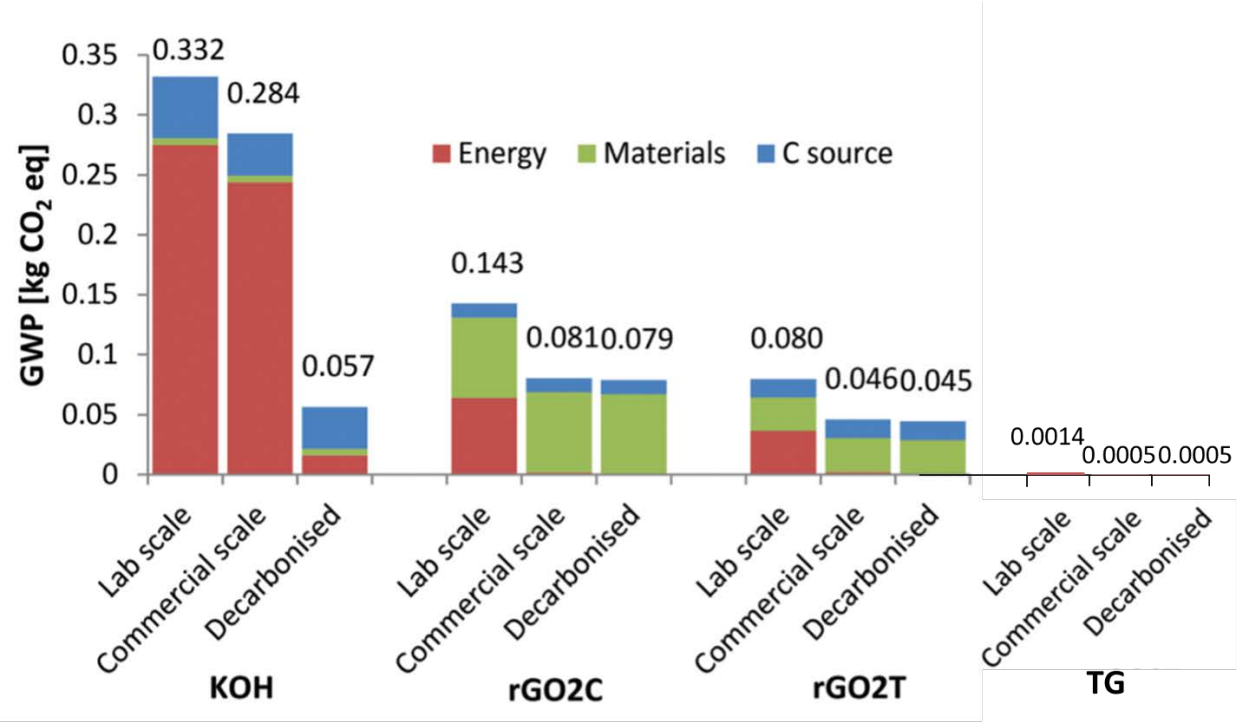

Figure 2.3. The graph shows the estimated energy (equivalent to CO_2 emission) to produce 1 g of graphene using different methods: (from left to right) electrochemical exfoliation, chemical exfoliation, chemical/thermo exfoliation and FJH.

In order to produce 1 g of graphene using conventional methods, > ~50 g of CO_2 is emitted to the environment. While using FJH method, the amount of CO_2 emitted is approximately the amount of graphene produced. The energy efficiency comes from the process itself that converts the electrical energy directly to breaking carbon-carbon bonds.

Modulus Rig

Using a 3D printer, an instrument to measure the elastic modulus and strength of the compressed coal pills (as reported below, the use of the pills was later abandoned because the results were found to be inferior to those that used powered starting materials in forming FG) was built and several materials were tested (**Figure 2.4**). The 3D printer was a very valuable tool for making parts that were used in almost every aspect of the project (**Figure 2.5**).

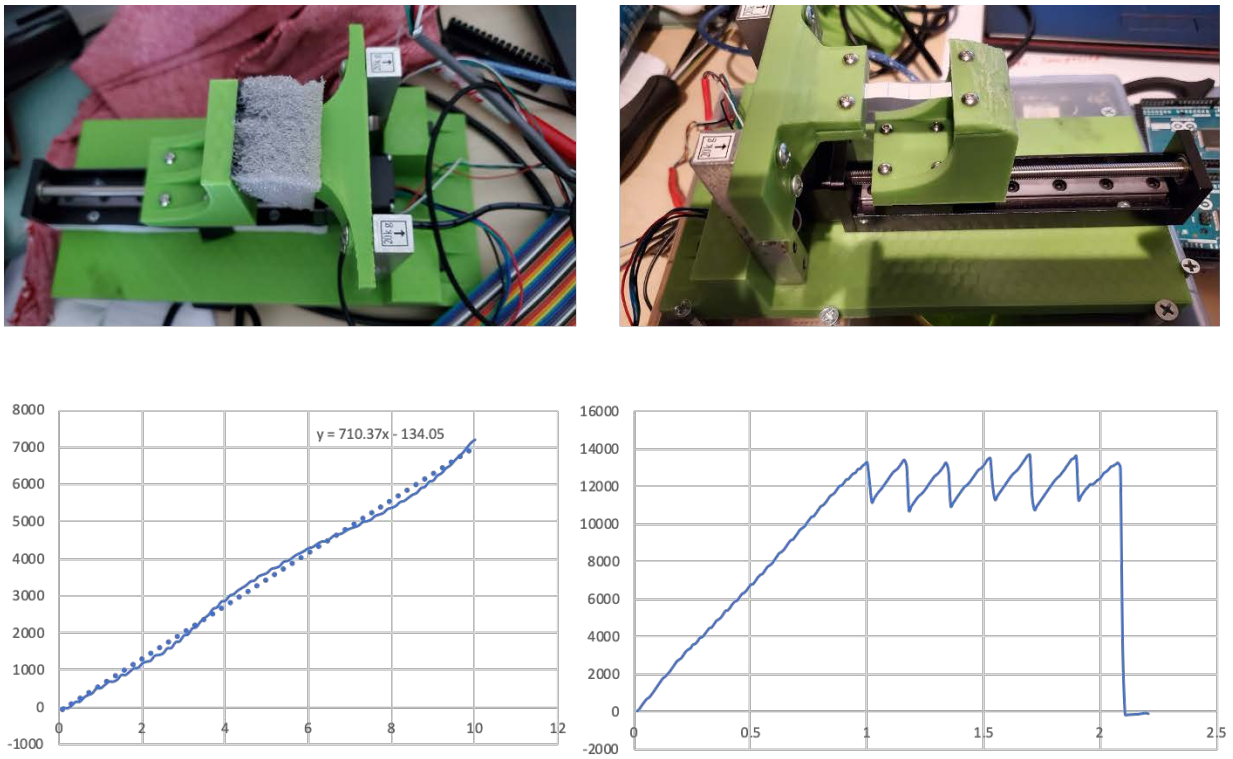

Figure 2.4. (top) Photos of the 3D printed modulus rig used to measure the elastic modulus and strength of the compressed coal pills. (bottom) Using the graphic output, one can measure the elastic modulus by the angle of the linear fit or the breaking point of the sample. We needed this data to measure the exact pressure at which the compressed pills break.

3D Printed Vacuum Chamber for Flashing Compressed Pills

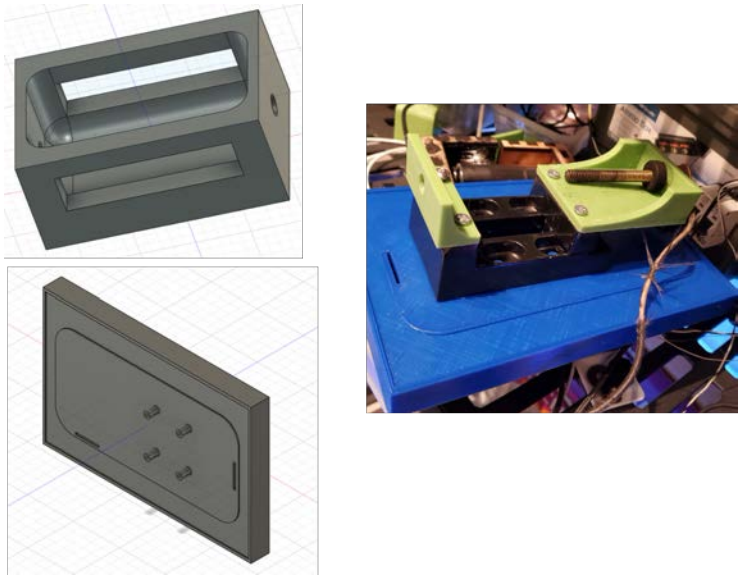

Figure 2.5. (left) The design and (right) a photo of the 3D printed vacuum chamber designed specifically for flashing the compressed coal pills. This will be used to compress the coal pill at a

certain pressure to maintain good electrical contact but keep the coal pill intact. The compressed pill approach is further discussed below.

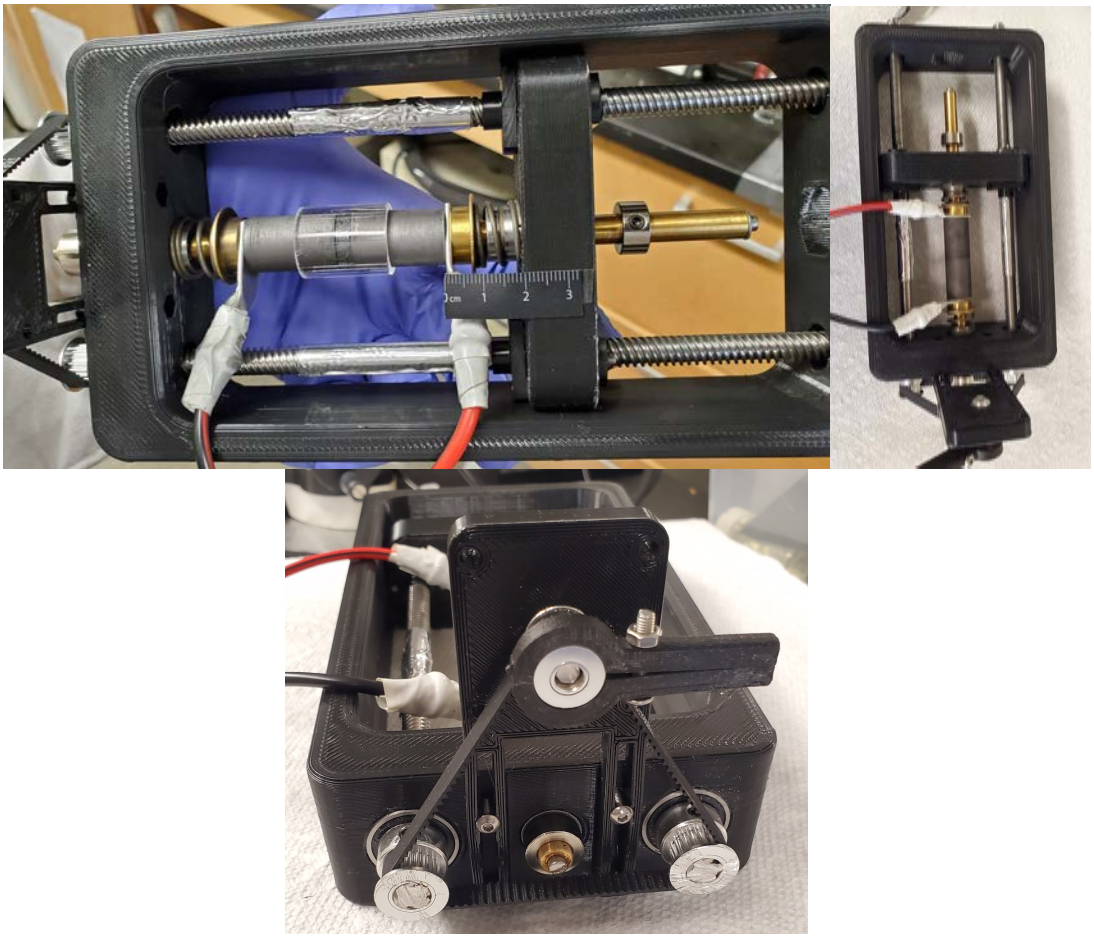

Figure 2.6. Detailed photos of the FJH reactor that uses compressed pills as the feedstock. (Upper left) A compressed pill between two electrodes. The pill is covered by a small section of tubing to prevent collapse of the product from between the electrodes and to control the outgassing that occurs during the reaction. (Upper right) A top view that shows the electrodes without the pill. (bottom) A view of the mechanical system that is used to compress the electrodes with the pill to achieve the proper conductance.

The FJH 5.0 reactor in the lab

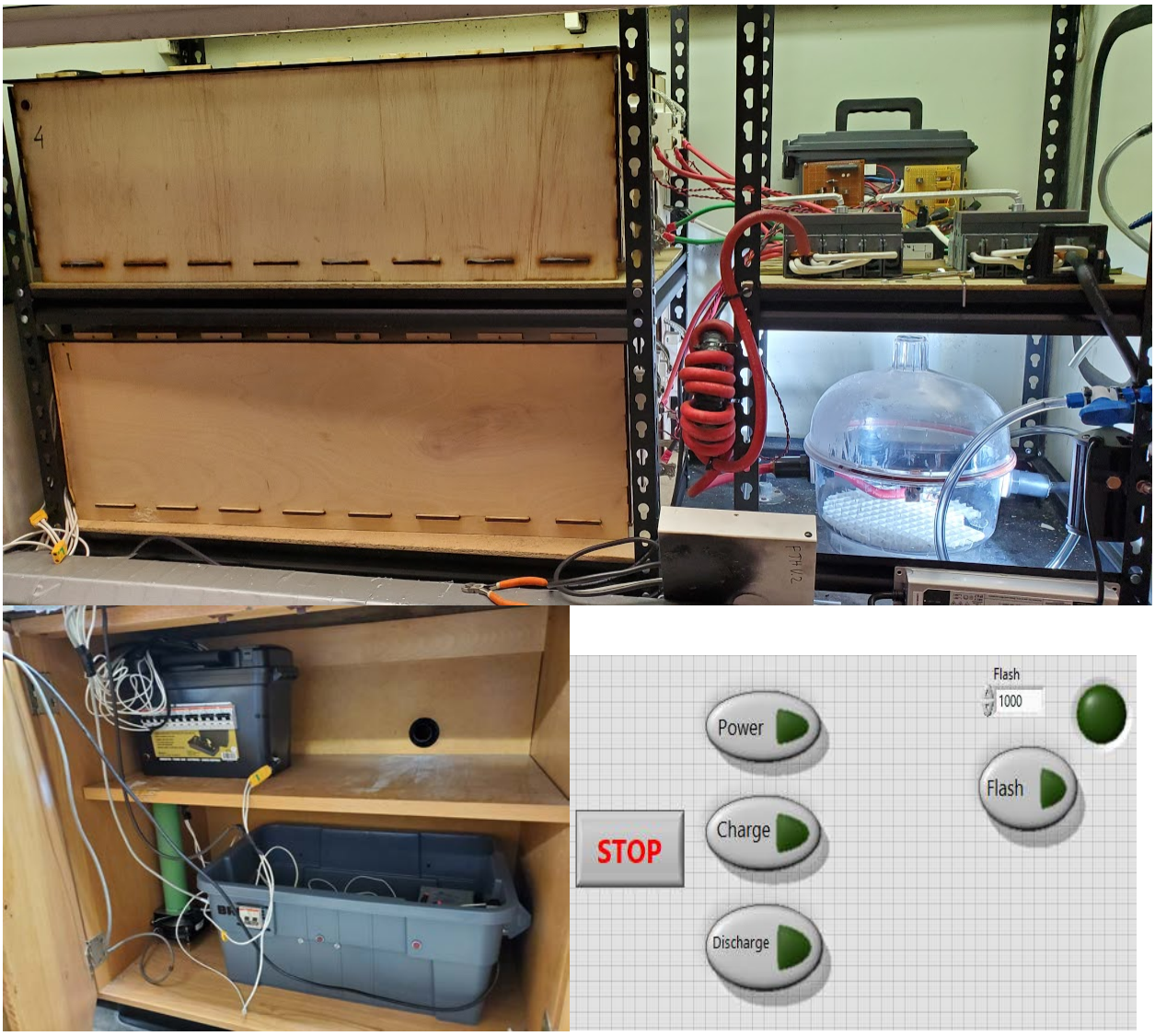

Figure 2.7. The FJH Version 5 System as Built. Upper image (left): 48 capacitors in 6 banks were placed on the left rack in the hood. (right) The right rack in the hood has the safety features: kill switches, inductor, safety diode; and IGBT drivers. Under the safety rack is the vacuum chamber that is used to contain the off gases of the FJH process, with an LED to illuminate the reaction so that a high-speed camera can capture the process in detail. On the lower left image is the charging system: transformer from 120 V to 480 V, bridge rectifier to turn AC to DC to charge the capacitors, and solid-state relays to control the charging and discharging. On the lower right is the *LabView* interface with the system that is used to control the power, charge, discharge and flash of the reactor. The user can control the reaction a safe distance from the system that is contained in the hood

FJH 5.0 performance overview

- Capable of delivering 3000 A
- All IGBTs synchronize well

- Flashed several hundreds of pressed pill samples
- Flashed nearly one hundred samples quartz tubes
- Sample flashed up to 5 g

Comments from users:

- Easy to use, friendly system
- Powerful system
- Much safer system

One unexpected incident occurred when electrodes shorted across a sample as the sample collapsed and fell away. All six IGBTs were lost. However, the system failed safely just as designed. All safety features worked to protect the overall system without loss of other components, and it was never a danger to personal safety since the system was fully contained, the capacitors were separated from the short circuit, and all electronics were in a closed hood. The electrodes have been redesigned such that they can never touch each other even if the sample crumbles

FJH 5.0: Comparison of Pill to Powder flashing

Pill flashing: Reaction of compressed pill in free form

- **Pros**: Independent of quartz tube, desirable for scale up system
- **Cons**: Need to find a good binder that is less volatile and the electrical contacts need to be precise.

Powder flashing Reaction of powder inside a quartz tube

- **Pro**: Less volatile material in the feedstock leads to ease of optimization
  Con: Depends on the quartz tube that is less favorable for scale up

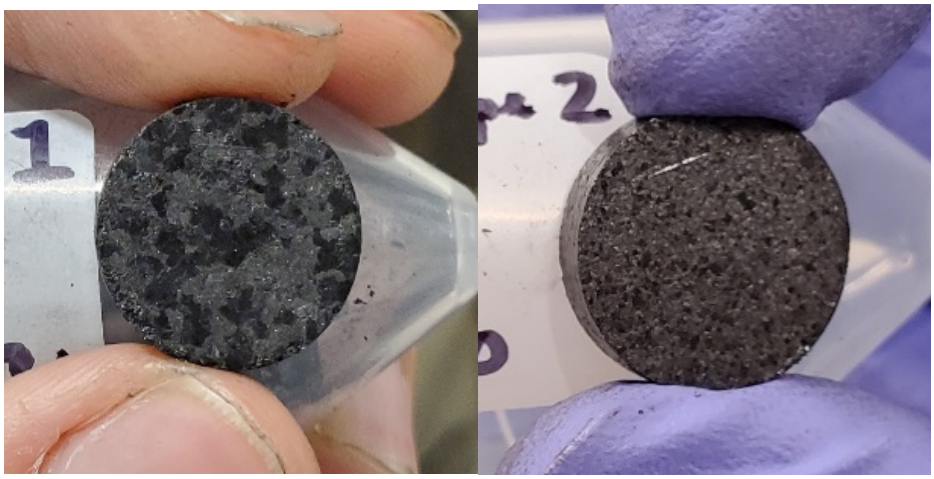

Figure 2.8. Metallurgical coke (MC, made from coal) and raw (green) petroleum coke (GPC) are mixed and pressed into a 1 g pill for use in the 5.0 FJH reactor. GPC acts as a binder while MC acts as a conductor. Both are graphene sources. From the photos, it is noted that GPC and MC need to have the same grain size to make consistent pills. (left) A too large grain size of the GPC and MC produces pills that are inconsistent in composition while (right) a smaller, matching grain size produce pills that appear consistent in composition Pills are compressed with a 15 mm die under 5 tons pressure

Table 2.4. FJH 5.0 optimization of reaction of pills of various compositions and grain sizes from 9 pills.

Mix of MC/GPC	#20-30 (0.6-0.84 mm)	#30-50 (0.3-0.6 mm)	#50-70 (0.21-0.30 mm)
50/50	Flashable	Flashable	Flashable
30/70	Inconsistent	Inconsistent	Inconsistent
70/30	Pill break	Flashable	Flashable

Table 2.5. A summary from hundreds of reactions recorded during optimization and preliminary machine language compilation.

Voltage	Frequency (Hz)/ duty cycle (%), ON/OFF (ms)					
	200/10 0.5/4.5	200/20 1/4	200/50 2.5/2.5	1000/10 0.1/0.9	1000/20 0.2/0.8	1000/50 0.5/0.5
160 reactions	20-30%	30-40%	Blows up	10-20%	20-40%	20-40%
200 reactions	30-40%	Blows up	Blows up	30-40%	30-40%	Blows up

Variable Frequency Drive flashing

Using pulse width modulation, we can turn DC flashing into AC flashing or variable frequency drive (VFD) flashing (**Figure 2.8 and Figure 2.9**). The result is a homogeneous and controllable flash where the Raman analysis shows a FG yield >80%. Using variable duty cycle in the same flash, we can further optimize the flash. Freestanding flash is demonstrated for the first time with multiple VFD flashing. The process yield is 40% with a 100% FG yield

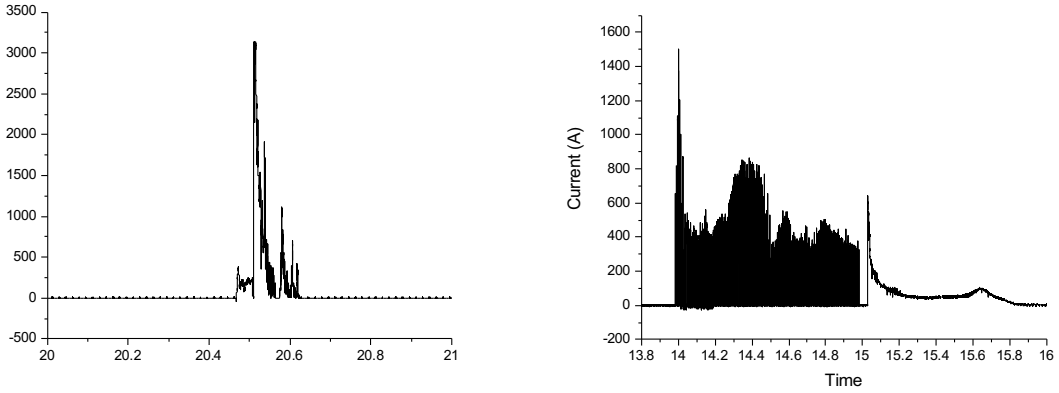

Figure 2.8. (left) Simple DC flash brings the current up to more than 3000 A and results in uncontrollable thermal runaway. (right) Variable frequency drive (VFD) flash allows controllable current and stops the thermal runaway.

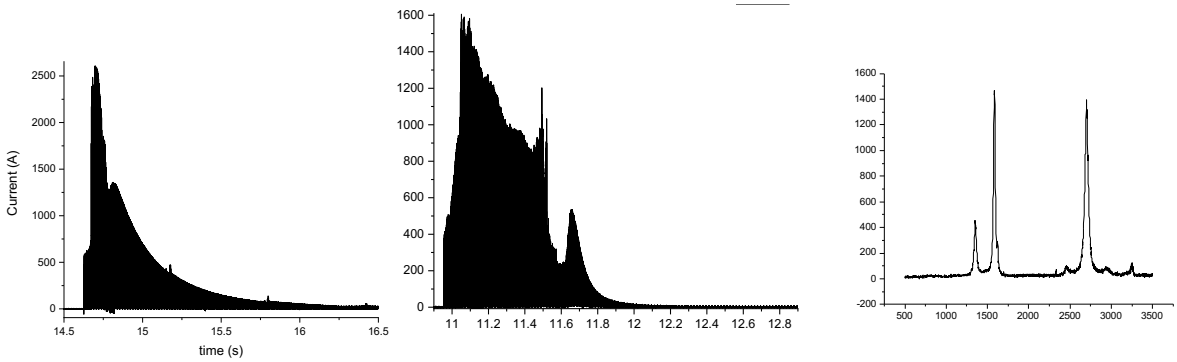

Figure 2.9. (left) A single VFD results in triangular current profile. (middle) Multiple VFD pulses result in a more desirable square shaped current profile. (right) Average Raman spectrum of graphene derived from VFD process.

FJH 5.0 powder reactions using VFD

- 5 g batch
- Homogeneous grain size powder provides an even flash
- High product yield (flashed material/feedstock) of 90%
- 100% conversion to graphene as determined by Raman spectroscopy.
- With VFD flashing no pretreatment is needed while graphene yield increases; this leads to a faster overall process. In 2 h we have made 30 g of FG (0.25 g/min).
- Further manual flashing optimization should result in 1 g/min production rate

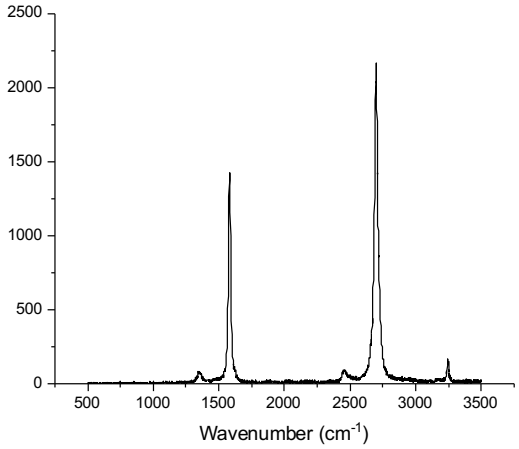

Figure 2.10. Average Raman spectrum from FJH 5.0 powder flashing shows high quality of graphene with low D peak and high 2D peak.

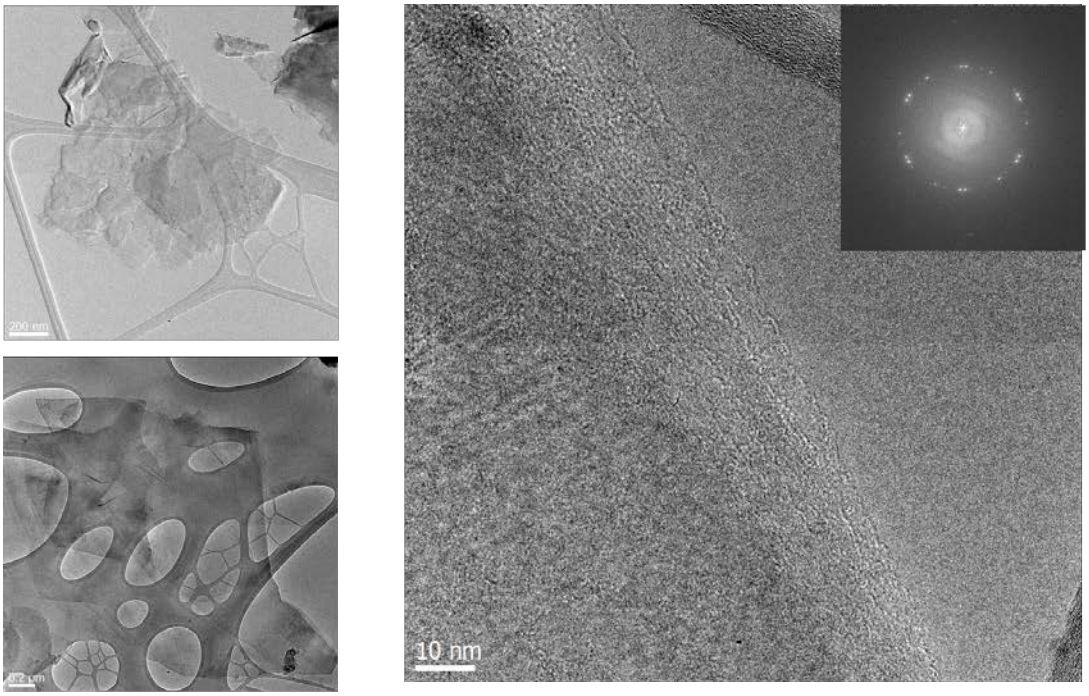

Figure 2.11. Turbostratic FG with 0.2-1 μm size particles.

Automation of FJH Reaction Using Powdered Feedstock

The automated system for producing 1 kg/day was built_using the 3D printer. The goal was 1 batch/min (5 g/min, 7.2 kg/24 h). 5.7 g of MC per batch to provide >5.0 g MC flash graphene per batch. Voltage: 350-400 V, VFD flashing at 1000 Hz, 20% duty cycle. Process yield is >90% with a graphene yield ~100%. Installed new Renishaw Raman Spectrometer system. Capable of autofocus and mapping. 121 Raman spectra in 10 minutes, 10 times faster than before

Energy Efficiency

- Small scale (0.1 g) batch has the conversion energy of 7.2 kJ/g at the beginning of the project
- Without VFD flashing, we can flash 5 g of sample with 0.62 F at 240 V. Conversion energy = 3.6 kJ/g, double the energy efficiency first demonstrated
- For VFD flashing, pre-treatment and flashing are done in one flash. A 5 g sample with 0.62 F at 300-330 V. Conversion energy = 5.6-6.8 kJ/g. Still better than the original work but not half. But again, the process yield is >90% with a graphene yield ~100%.
- The conditions and settings for each flash are being saved to a database so that they can be used in AI machine learning training.
- For this process it appears that a powder is preferable over a solid compressed pill to produce higher yields.

Machine Learning-Guided Synthesis of Flash Graphene 3.

Summary of Section 3.

Advances in nanoscience have enabled the synthesis of nanomaterials, such as graphene, from low-value or waste materials through FJH. Though this capability is promising, the complex and entangled variables that govern nanocrystal formation in the Joule heating process remain poorly understood. In this work, we construct machine learning (ML) models to explore the factors that drive the transformation of amorphous carbon into graphene nanocrystals during FJH. An XGBoost regression model of crystallinity achieves an r^2 score of 0.8051 ± 0.054. Feature importance assays and decision trees extracted from these models reveal key considerations in the selection of starting materials and the role of stochastic current fluctuations in FJH synthesis. Furthermore, partial dependence analyses demonstrate the importance of charge and current density as predictors of crystallinity, implying a progression from reaction-limited to diffusion-limited kinetics as FJH parameters change. Finally, we show a practical application of the ML models by using Bayesian meta-learning algorithms to automatically improve bulk crystallinity over many Joule heating reactions. These results illustrate the power of ML as a tool to analyze complex nanomanufacturing processes and enable the synthesis of 2D crystals with desirable properties by FJH.

Introduction to Machine Learning

The scalable synthesis of nanomaterials is a crucial goal in materials science. To achieve the widespread use of nanotechnology, nanomaterials must be synthesized by rapid and scalable processes that do not deleteriously affect their properties. To address this challenge, we and others

recently reported the synthesis of graphene,[1–3] as well as mixed-phase MoS_2 and WS_2,[4] high-entropy alloy NPs,[5,6] nanodiamond,[7] and other nanomaterials using the electrothermal FJH effect. The graphene product is called flash graphene (FG) after the intense black body radiation produced during the electrical discharge. FJH permits the conversion of amorphous carbon, including waste such as pyrolyzed rubber tires,[8] ash by-products from plastic recycling,[9] or landfill-grade mixed plastic waste,[10] into graphene crystals. Furthermore, flash graphene crystals are turbostratic and exhibit varying degrees of layer-to-layer misorientation along the c-axis.[1] Such turbostratic graphene possesses nanostructure-dependent properties, including enhanced solubility in surfactant solutions[1] and altered band structure.[11] The scalable and environmentally friendly nature of the Joule heating process, as well as the turbostratic nature of the synthesized product, make FJH an intriguing synthetic technique that warrants further study and analysis.

Although FJH has immense practical utility, it is intrinsically difficult to study. The FG formation process occurs in just hundreds of milliseconds. Furthermore, present-day FJH reactors do not offer control over the current discharge profile, adding a stochastic element to each reaction that depends on momentary fluctuations in circuit-to-sample contact. These fluctuations are difficult to control experimentally, making it challenging to map process-structure-property relationships by a traditional grid-search. Due to these factors, the parameters that drive bulk nanocrystal formation during FJH remain ambiguous.

At the same time, an emerging body of literature indicates that machine learning (ML) is a powerful tool for fundamental studies in materials science.[12–18] While ML is classically considered an industrial tool for process failure prevention, the use of ML to interrogate large parameter spaces can yield insights on new technologies at a low time-cost. For example, Tang *et al.* used ML to explore the process-structure-property relationships governing well-understood processes, such as chemical vapor deposition and quantum dot synthesis, and argued based on their results that ML would allow researchers to investigate them more efficiently than was previously possible.[16] This work is emblematic of a growing acknowledgement that ML possesses tremendous potential even in exploratory research.

Immense progress has been made by utilizing ML in materials engineering,[19] especially in theoretical studies,[20-21] where ML is commonly used to approximate solutions to partial differential equations and enhance predictions of materials properties. These ML-enhanced property predictions can then serve to identify promising candidate materials.[22] Furthermore, Bayesian model-based optimization techniques offer new avenues for materials discovery and property improvement.[23-24] Such optimization techniques leverage ML's propensity for function approximation to minimize or maximize a given objective function, in many cases opening new opportunities for automated materials processing. In previous studies, Bayesian optimization algorithms were used to design shape-tailored gold nanocrystals,[25] optimize composite designs for various force-loading conditions,[26] and uncover novel syntheses for organic compounds.[27] Some Bayesian learning algorithms have even been designed specifically for scientific exploration, using boundary-free methods to facilitate identification of out-of-trend observations in high-throughput computational studies.[28]

Here, we construct ML models to predict the effects of FJH process parameters on the crystallization of flash graphene from low-value materials or waste. The unique capabilities of ML enable a detailed study of direct-current FJH despite the large parameter space involved and the presence of uncontrollable stochastic elements. Furthermore, we demonstrate the use of a Bayesian optimization algorithm to iteratively improve graphene crystallization over many trials. These

results offer useful insights regarding the FJH technique and provide a potent demonstration showing how ML can enhance the study of new materials synthesis technologies.

Machine Learning—Results and Discussion

As shown in **Figure 3.1a**, we first synthesized FG from four low-to-negative value amorphous carbon starting materials in N = 173 separate Joule heating reactions. FJH was performed on a custom-built direct-current Joule heating station (**Figure A3.1**). The starting materials employed in these reactions were: carbon black,[1] plastic waste-derived pyrolysis ash,[9] pyrolyzed rubber tires,[8] and MC. Then, we assessed the structural character of each sample by wide-area Raman mapping. Each of the >20,000 spectra collected in this study was pre-processed (**Figure A3.2**) and analyzed by custom-written scripts, which compiled a metric to estimate the proportion of the amorphous starting material in each sample that had crystallized into graphene. This metric was termed the "graphene yield." Finally, we constructed a suite of ML models to predict the graphene yield of each reaction.

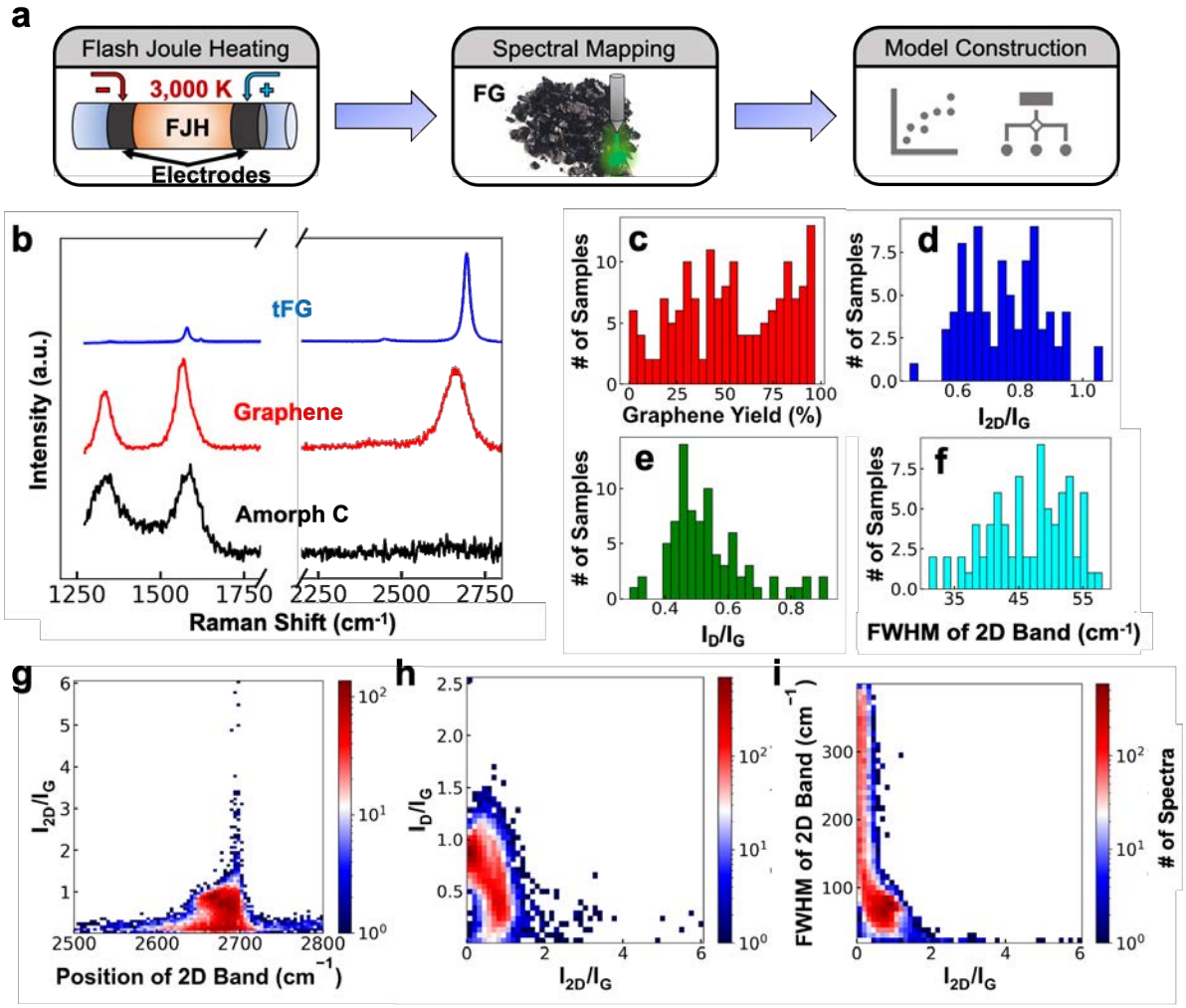

Figure 3.1. Scheme and analysis of dataset. **(a)** Schematic depiction of study. **(b)** Sample Raman spectra of amorphous carbon, graphene, and turbostratic flash graphene, exemplifying the distinction between typical flash graphene spectra (red) and spectra from highly turbostratic

graphene crystals (blue). These Raman spectra were collected from flashed samples of carbon black. **(c-f)** Bulk average statistics of the graphene yield, I_{2D}/I_G, I_D/I_G, and FWHM of the 2D band of each sample analyzed in this study. **(g-i)** 2D histograms showing statistics from ~16,000 Raman spectra obtained from spots of flash Joule heated material, showing relationships between **(g)** the 2D band position and I_{2D}/I_G, **(h)** I_{2D}/I_G and I_D/I_G, and **(i)** I_{2D}/I_G and the FWHM of the 2D band. These plots show the blue shift, narrowing, and resonance enhancement of the 2D band in spectra from highly turbostratic graphene crystals.

Sample Raman spectra of amorphous carbon, graphene, and highly turbostratic graphene are shown in **Figure 3.1b**. Raman spectroscopy is a powerful technique for the structural characterization of carbon, especially graphitic materials.[29–31] Spectra of amorphous carbon contain two bands: the G and D bands. The D band is forbidden by selection rules, but it commonly appears due to symmetry disruptions, such as armchair edges or point defects. Raman spectra of graphene and graphite contain the second-order overtone of the D band, referred to as the 2D band. The appearance of this band is a positive indicator for the formation of a graphitic lattice, and its shape and intensity offer important nanostructural information. Spectra of high-quality turbostratic flash graphene contain a resonance-enhanced single-Lorentzian 2D band with a narrow full width at half maximum (FWHM; ~16 cm^{-1}) and a magnified I_{2D}/I_G peak intensity ratio (up to a maximum of 17) as compared to pristine single-layer graphene (which possesses I_{2D}/I_G of ~3).[32]

Histograms in **Figure 3.1c-f** show sample-level statistics compiled from Raman mapping, including the graphene yield, the average I_{2D}/I_G, the average I_D/I_G, and the average FWHM of the 2D band. Statistics on individual spectra (shown in **Figure 3.1g-i**) illustrate relationships between the I_{2D}/I_G ratio, the FWHM of the 2D band, and the position of the 2D band, showing a blue-shifted and narrowed 2D band at high I_{2D}/I_G which is indicative of resonance-enhanced turbostratic graphene.[2,10,32] Wide-area mapping is used to assess crystallinity because the Raman spectra of flash graphene samples can vary quite widely throughout individual samples (**Figure A3.3**). The high-throughput nature of the mapping assay ensures that the compiled metric accurately captures the bulk character of each sample. From these mapping assays, the "graphene yield" can then be calculated as the percentage of Raman spectra from each sample that can be classified as graphene rather than amorphous carbon (a detailed discussion of selection criteria can be found in the Experimental Section). This graphene yield metric was then validated quantitatively by thermogravimetric analysis and qualitatively by scanning electron microscopy. Thermograms show that higher-yield flash graphene samples were typically more thermally stable than their lower-yield counterparts (**Figure A3.4**), while scanning electron micrographs reveal a visible microstructural evolution from low-to-high crystallinity (**Figure A3.5**). Flashed materials were additionally characterized by X-ray diffraction (**Figure A3.6**) and X-ray photoelectron spectroscopy (**Figures A3.7-A3.10, Table A3.1**).

Model Construction and Performance.

ML regression models were constructed to predict the graphene yield metric derived from Raman spectral mapping. First, a total of five features were empirically selected from the available parameters tested for the prediction of graphene yield (see **Table A3.2** and **Figures A3.11-A3.14** for a summary of the features attempted and dataset characteristics). Then, the five selected features were used to train six ML regression models for the prediction of graphene yield. Linear regression (LR-R),[33] Bayesian regression (BR-R),[34] multilayer perceptron (MLP-R),[35] decision

tree (DT-R),[36] random forest (RF-R),[37] and eXtreme Gradient Boosting (XGB-R)[38] regression models were trained using 5-fold cross-validation. Hyperparameters were tabulated in **Table A3.3.**

Figure 3.2a-b shows the performance of regression models predicting graphene yield. For this task, decision tree-based models, including DT-R, RF-R and XGB-R, achieved the best performance. RF-R models achieved RMSE of 12.7% $\pm$ 1.3% and an r^2 score of 0.7808 $\pm$ 0.064. XGB-R models, such as the example shown in **Figure 3.2c**, achieved even better performance, with a RMSE of 11.3% $\pm$ 2.2% and an r^2 score of 0.8051 $\pm$ 0.054. The error distribution was skewed, since ~40% of the samples tested showed predictions that were <5% off from the true value (**Figure 3.2d**). Sample performances of other ML regression models are shown in **Figure A3.15**.

ML models arrive at their predictions based on the algorithms upon which they are constructed. Decision tree-based models, *i.e.,* DT-R, RF-R, and XGB-R, make predictions based on a series of if/then statements derived from the input features, which together form a "tree" of many branches that yield different predictions of the output metric. The DT-R model uses a single decision tree, while the RF-R model uses an ensemble of trees to produce a weighted average prediction. The XGB-R model also uses an ensemble of trees, but it constructs trees and sequentially weights their prediction. This sequential weighting, called "gradient boosting," enhances model accuracy and has led XGB-R to be one of the most widely used ML models since its introduction in 2016.[17,38,39] In contrast to decision tree-based models, linear regression models, such as LR-R and BR-R, make predictions based on linear combinations of the input features. Decision trees systematically outperform linear models in this study, suggesting that the relationships between crystallinity and the input parameters used to train the model are nonlinear (**Figure A3.16**).[40] An artificial neural network (MLP-R) also achieves satisfactory predictions of crystallinity, but is outperformed by the decision tree-based models in this study.

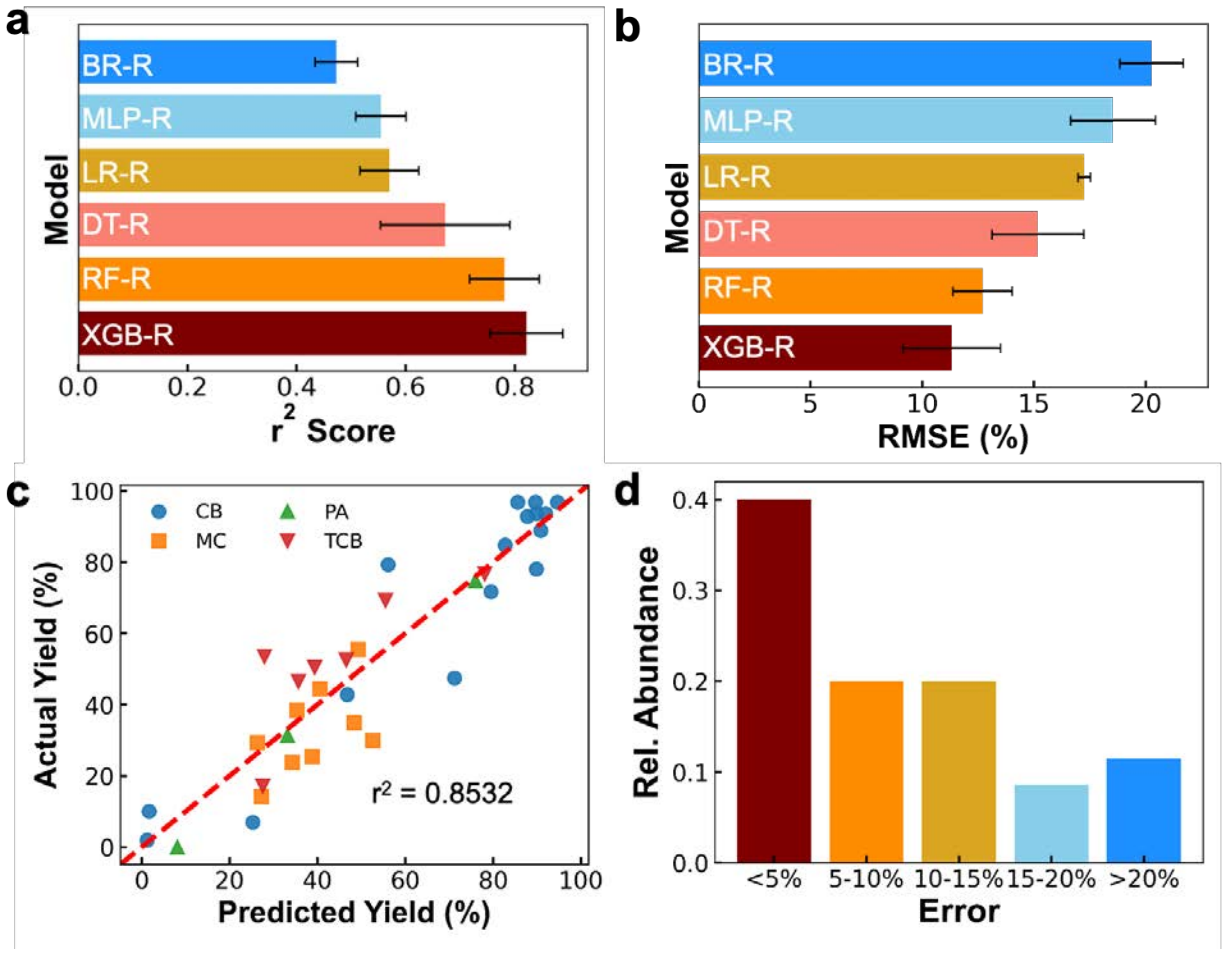

Figure 3.2. Performance of regression models predicting graphene yield. **(a)** Typical r^2 scores of six types of regression models for the prediction of graphene yield from flash parameters. Error bars represent the standard deviation of the r^2 scores across 5 train/test split iterations. **(b)** Root mean squared error (RMSE) of the six models presented in (a). **(c)** Performance of an XGB-R for the prediction of graphene yield. CB: carbon black; PA: pyrolysis ash; MC: metallurgical coke; TCB: tire-derived carbon black. **(d)** A typical error distribution for an XGB-R model of graphene yield.

Model Interpretation & Analysis.

Feature Importance Analysis.

Feature importance analysis provides an estimate of the predictive power of all the features used to train an ML model. **Figure 3.3** introduces the features used to train ML models predicting crystallization. The selected features were the charge density (CD), the material type (M), the area under the time-current curve divided by the sample mass (A_{IT}), the maximum current divided by the sample mass (I_{Max}), and the final current divided by the maximum current (I_F/I_{Max}). Two of the features, CD and M, were derived from controllable FJH experimental variables. The other three features, A_{IT}, I_{Max}, and I_F/I_{Max}, were derived from time-current curves recorded during the reaction by a Hall effect sensor (**Figure 3.3a**) and extracted using custom-written scripts. While predictions of crystallinity could be made with the experimental parameters alone, the time-current curves

offered complementary information regarding changes in the sample resistance over time, as well as fluctuations in contact between the sample and the circuit due to outgassing. These changes are difficult to control experimentally. Consequently, the inclusion of current-derived statistics in the feature set boosted model performance (**Table A3.2**). **Figure 3.3b** shows the correlation matrix between the five empirically selected features.

Figure 3.3c shows a feature importance analysis for the features used to train the XGB-R model, which indicates that CD was the most crucial feature for predictions of bulk crystallinity. CD represents the amount of charge inside the FJH station's capacitor bank at $t = 0$ per g of carbon. It is calculated by multiplying the initial voltage (V_0) by the capacitance of the system (C) and dividing by the sample mass (m). Since Joule heating produces thermal energy from collisions between electrons and atomic nuclei,[41] CD is likely related to heat or energy density. Previously, charge and current density were found to control the rate of transformations of carbon materials on smaller scales.[42,43] Moreover, prior experiments in other non-equilibrium graphene synthesis techniques showed that laser-induced graphene synthesis depended on the reaction reaching a critical irradiation fluence to achieve sufficient energy density.[44] **Figure 3.3d** shows that, generally, FJH reactions with low CD produce fewer graphene crystals, while most FJH reactions with high yield employ high CD. Decision trees extracted from the XGB-R model further support the hypothesis that high CD leads to high yield predictions (**Figure 3.3e**). **Figure A3.17** explores the relationship between CD and graphene yield, showing that the specific combination of C, V_0, and m into CD produces a metric that is more correlated with crystallinity.

The chosen starting material, denoted "M," also plays a critical role in predicting FJH efficacy as shown in **Figure 3.3c**. This is also apparent from **Figure 3.2c**, which shows that, generally, carbon black-derived FG possessed high crystallinity, while MC-derived FG possessed low crystallinity even in conditions of high CD. This precursor-dependent crystallization likely cannot be attributed to differential heating abilities, since the low resistance of MC allows the generation of higher current compared to the other three feedstocks (**Figure A3.18**). Therefore, the lower crystallinity of coke-derived flash graphene likely arises from the large size of the MC particles (150-210 μm).

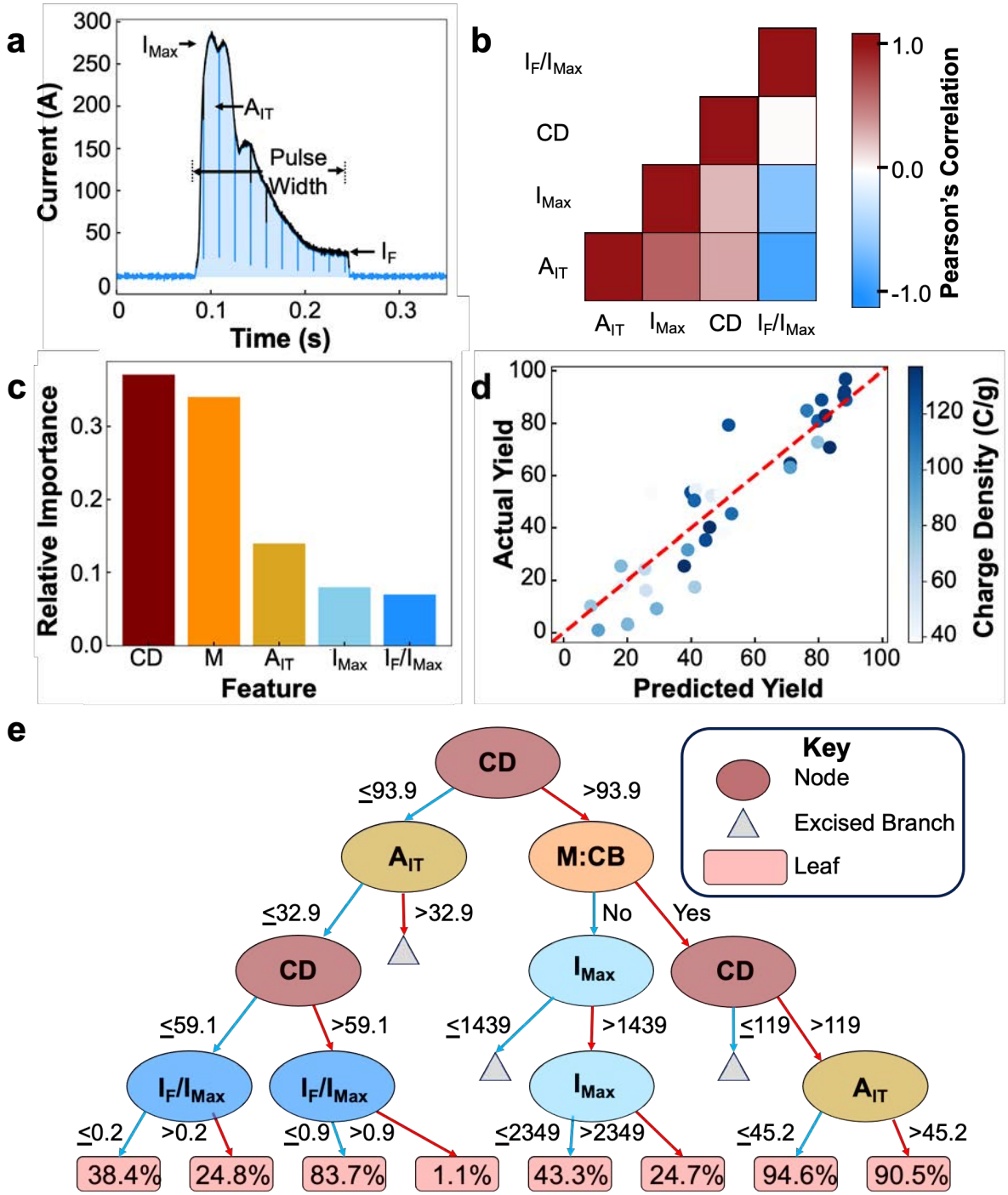

Figure 3.3. Feature analysis of XGB-R model for prediction of graphene yield. **(a)** A sample time-current curve showing features extracted from the discharge profile of each flash. **(b)** A correlation map of the five features used to train ML models. **(c)** Relative feature importance of the five empirically chosen features included in this model. **(d)** Color map of the graphene yield prediction of the test data set after train/test splitting and training of the model on the training data. The color map illustrates the effect of charge density on the predicted and actual yields. **(e)** Map of a typical decision tree derived from XGB-R showing the effects of various process parameters on the final

predicted value. Individual decision trees are weighted according to their accuracy to assemble a final prediction value. CD: charge density; M: material type; A_{IT}: area under the time-current curve normalized to the sample mass; I_{Max}: maximum current normalized to the sample mass; I_F/I_{Max}: final current divided by maximum current.

The other three features, i.e., A_{IT}, I_{Max}, and I_F/I_{Max}, make smaller but still significant contributions to model predictions of graphene yield. A_{IT} is the area under the time-current curve divided by the mass, while I_{Max} is the peak current divided by the mass. Ergo, three of the five features used to train the model, CD, A_{IT}, and I_{Max}, represent metrics of charge or current density. CD and A_{IT} are conceptually similar, both representing measurements of charge per unit mass, but they convey different information and are not correlated ($r = 0.36$). CD, which is calculated using the initial voltage V_0, represents the charge present in the capacitors at $t = 0$. Conversely, A_{IT} represents the charge that passes through the sample during the reaction, which relates to the voltage drop ΔV rather than V_0. As a result, CD offers information about the initial state of the system, while A_{IT} offers information about the system while the reaction is taking place. The large dependence of graphene yield on CD might indicate that most of the crystallization reaction occurs near the beginning of the FJH reaction, which has previously been predicted theoretically.[1] Alternatively, the lack of a neat dependence on the Joule-Lenz power, which scales with V_0^2 rather than V_0 (**Table A3.2**), could offer evidence that electrostatic effects[41] contribute in tandem with Joule heating to the formation of large flash graphene crystals.[45] Nevertheless, the predictive power of CD, A_{IT}, and I_{Max} suggests that charge and current density are the key considerations in the prediction of FJH reaction efficacy. Finally, I_F/I_{Max} likely conveys whether the reaction was forced to stop prematurely due to stochastic contact disruptions or outgassing.

Partial Dependence Analysis.

Partial dependence (PD) analysis is a powerful analytical tool accessible through ML. PD represents the average model prediction for given values of each feature. Partial dependence plots (PDPs) map relationships between features and the target output, giving additional insight as to how ML models arrive at their conclusion. For example, PDPs from decision tree models show sharp dips and wrinkles at the nodes of prominent trees, whereas PDPs from other models show a smoother PD surface (**Figure A3.19-A3.20**). Multivariable PDPs of the quantitative features included in the XGB-R model are shown in **Figure 3.4**. They reveal that the three metrics related to charge or current density (CD, A_{IT}, and I_{Max}) have similar relationships with crystallinity. At low values of "*x*", graphene yield systematically increases with the values of these features. Then, at higher values, this relationship plateaus.

Justification for the behavior observed in PD functions of CD, A_{IT}, and I_{Max} can be found by taking inspiration from wet nanocrystal synthesis. Since charge or current in FJH is related to energy density, increasing the values of these metrics is analogous to increasing the temperature in a classical synthesis reaction. Following this analogy, such a dynamic relationship between energy density and crystallinity could suggest a shift in reaction kinetics from surface reaction-controlled nucleation to a diffusion-controlled regime.[46] At low reaction energies, nucleation occurs selectively at hotspots, and increasing the energy density can dramatically affect the bulk crystallinity of the product. However, at higher reaction energies, the entire sample volume receives sufficient energy for nucleation. In this regime, increasing the reaction energy no longer affects the crystallinity of the end-product (**Figure A3.21**). The PDPs shown in **Figure 3.4** suggest that such a transition may occur at CD values between 100 and 120 C g^{-1} where PD ceases to

increase with CD. Consequently, this range might serve as useful benchmarks for new FJH syntheses or systems. Additionally, it is possible that increasing the FJH reaction energy beyond this transition point would move the nucleation process further into the realm of diffusion control, causing disperse nucleation and allowing some degree of size control over flash graphene crystals.

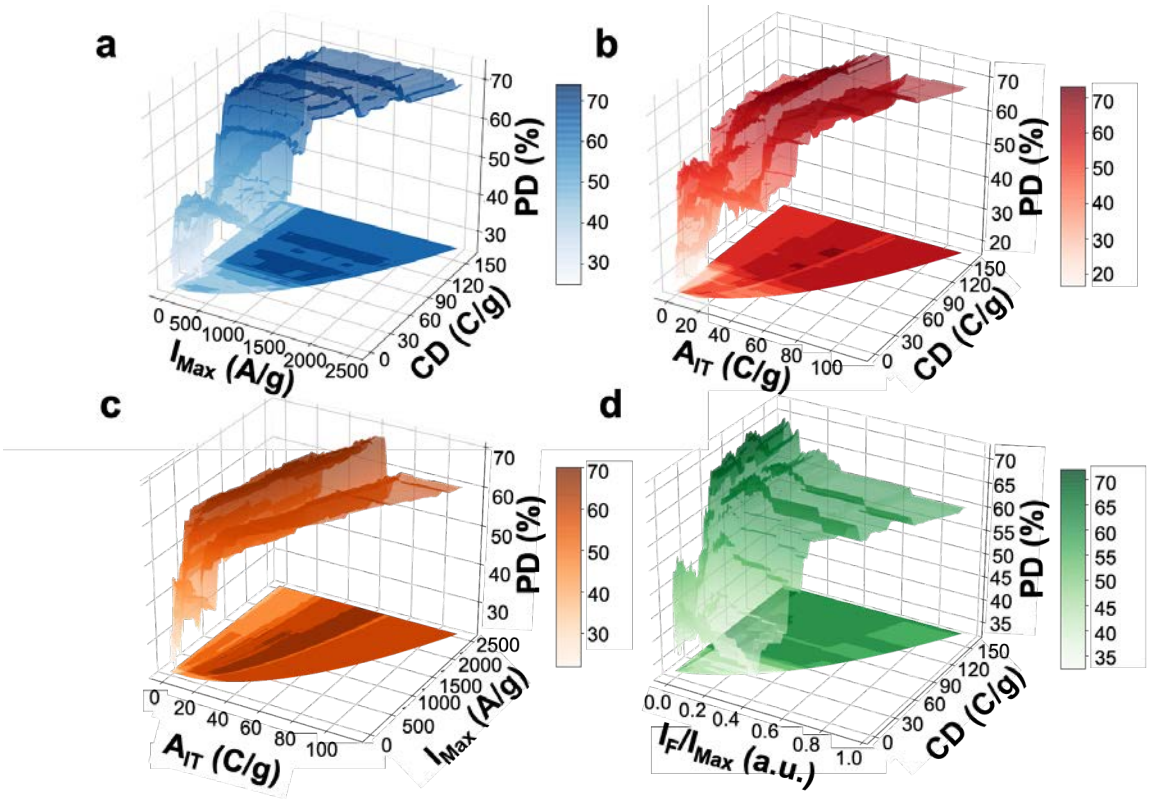

Figure 3.4. Multivariable partial dependence plots (PDPs) of **(a)** charge density and normalized maximum current, **(b)** charge density and normalized area under the current/time curve, **(c)** normalized maximum current and area under the current/time curve, and **(d)** charge density and the final current divided by the maximum current. PDPs were constructed based on the predictions of models for samples in the test data set. Each plot maps PD (on the z-axis) for given values of two features (on the x and y axis). The color map overlaid on the xy-grid reflects the value of PD as a function of the two chosen features and serves as a visual aid.

Bayesian Optimization.

The previous analyses show ML's ability to derive process-structure-property relationships in FJH synthesis. However, from a practical point of view, it is vital that these relationships can guide new syntheses using the knowledge they provide. Therefore, we sought to use ML predictions of flash graphene crystallinity to recommend synthesis reaction conditions for new feedstocks using Bayesian model-based optimization (**Scheme 3.1**). First, a "starter" data set compiled using randomly generated parameters was fed to the algorithm. Then, the algorithm generated predictions based on an RF-R surrogate model and suggested a new set of parameters. The algorithm leverages experience from past trials to explore the parameter space, trading off expected performance and exploration of uncertainty according to an assigned acquisition

function.[24,47] Eventually, this exploration yielded an enhanced graphene yield. Altogether, this automation process results in a system that can robustly synthesize flash graphene from waste with no prior knowledge about the starting material.

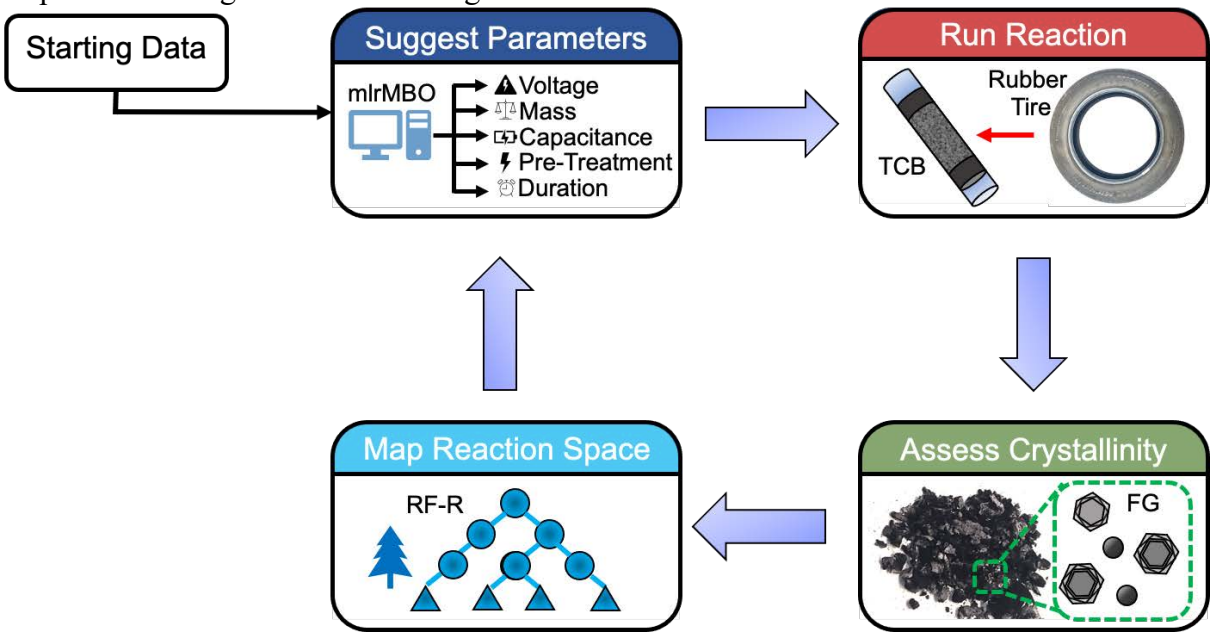

Scheme 3.1. Scheme showing the feedstock-blind automatic optimization of flash graphene synthesis using a Bayesian meta-learning algorithm.

Toward this end, we implemented the process in **Scheme 3.1** using pyrolyzed rubber tires as a model waste material. **Figure 3.5a-b** shows that, after just 30 iterations, the mean graphene yield of tire carbon black-derived flash graphene synthesized using parameters suggested by the Bayesian optimization algorithm is 79%. This is significantly ($p<0.0001$) higher than that achieved by random parameter values (36%). The improvement of crystallization efficacy throughout the optimization process is additionally verified by X-ray diffraction analysis (**Figure A3.22**) and scanning electron microscopy (**Figure A3.23**). **Figure 3.5c** shows that the improvements in flash graphene crystallinity depend on the identification of a favorable region in the FJH parameter space, with an optimal pre-treatment, mass, pulse width, and charge density. **Figure 3.5d-i** shows PD relationships derived from the RF-R model used to suggest new parameters. The relationships derived from the learner model are consistent with findings from the full dataset, as prediction values show direct correlations to voltage and capacitance but inverse correlations to sample mass.

The efficacy of the Bayesian optimization algorithm offers a promising outlook for automated flash graphene synthesis. Since flash graphene is commonly synthesized from waste materials,[1,8-10] advantageous precursors for FJH are diverse and likely to continually evolve as new exploitable wastes are identified for upcycling. Furthermore, many waste streams, such as those derived from household waste, will likely possess a high degree of heterogeneity. Therefore, it is vital to be able to readily synthesize flash graphene from scratch with new starting materials and processes. The Bayesian optimization algorithm demonstrated here shows the ability to take waste materials with no prior identification or characterization and produce high-quality flash graphene in a low number of trials. Further development of this technique, potentially including the use of principal component analysis to process the Raman spectral profile of the produced graphene more

directly,[48] may streamline the FJH process even further and lead to higher accuracy in optimization. These results show the capability of ML to accelerate the synthesis of nanomaterials by FJH.

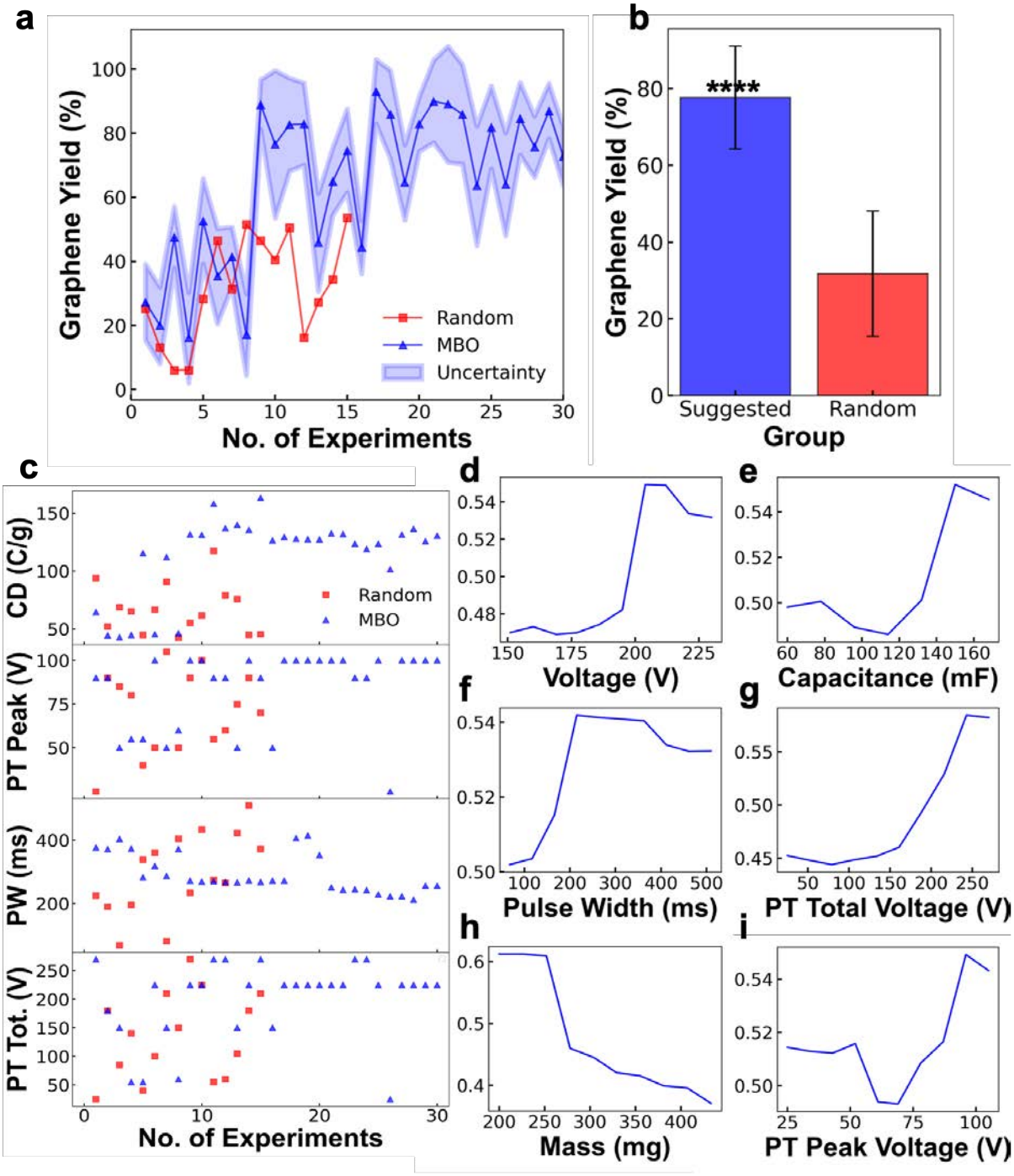

Figure 3.5. Model-based optimization according to graphene yield. **(a)** Graphene yield of FJH reactions from tire-derived carbon black using randomized parameters and parameters suggested by a model-based optimization algorithm (MBO). Error bars represent the estimated uncertainty

by the algorithm. **(b)** Mean values of the yields given by the randomized parameters and the MBO-suggested parameters. The mean values are different with a significance level of $p<0.0001$. **(c)** Parameters suggested by the model-based optimization algorithm and random parameters. Mass, voltage, and capacitance are grouped into charge density (CD), calculated as C×V/m. The pre-treatment (PT) total voltage, the PT peak voltage, and the pulse width (PW) are also presented. **(d-i)** Partial dependencies of experimental parameters affecting the model-based optimization results, calculated by the RF-R learner algorithm implemented in R.

Conclusion for ML Section

This study provides a framework for the use of ML to predict the efficacy of FJH reactions in nanomaterial synthesis. ML models have been used to predict the extent of crystal formation, extract fundamental information, and drive process optimization. Feature analyses from these models showed that metrics of charge and current density primarily dictated the extent of crystallization. Furthermore, the contributions of starting material properties and the current delivery profile were analyzed. Model-based optimization has been demonstrated to autonomously improve the crystallinity of flash graphene over many trials. These results offer both fundamental insight and practical utility for advancing the use of FJH in nanomaterials synthesis. We anticipate that the framework laid out in this study can be expanded, potentially *via* the use of principal component analysis for dimensionality reduction of both the time-current curve and the output Raman spectra. This strategy would allow more advanced ML algorithms to deal directly with collected data, improving accuracy, offering more interpretable conclusions, and streamlining the interplay between ML and FJH. Overall, the use of ML demonstrates synergy with the FJH technique, and the continued use of ML models for its study and optimization may maximize its potential for graphene commercialization.

Experimental Section.

Materials

Four low-or-negative-value feedstocks were employed for conversion to FG: carbon black (Cabot BP2000), MC (SunCoke Energy Inc., 70-100 mesh size, 150-210 μm grain size), pyrolysis ash (Shangqiu Zhongming EcoFriendly Equipment Co.), and pyrolyzed rubber tire-derived carbon black (Ergon Asphalt and Emulsion Co.). All materials were ground with a mortar and pestle before and after FJH but otherwise used as delivered. Commercial graphene nanoplatelets used for comparisons were obtained from XGSciences (xGnP-15, serial #5051209) and used without further modification.

FJH Reactor

A custom-built direct-current FJH reactor was employed for all experiments. Precursor powders ($100 \leq m \leq 400$ mg) were sandwiched between two graphite electrodes and compressed inside an 8” diameter quartz tube. Then, the samples were placed in a series circuit with ten 6 mF capacitors (Mouser #80-PEH200YX460BQU2) and six 18 mF capacitors (Mouser # 80-ALS70A183QS400). The ten 6 mF capacitors, typically employed for small-scale FJH reactions in our lab, were used as the minimum-size capacitor bank in our experiments, while the six 18 mF capacitors were

connected and disconnected from the circuit *via* circuit breakers to modulate the capacitance employed in each flash reaction. This resulted in C of 60 mF $\leq$ C $\leq$ 204 mF. Voltage to charge the capacitors was supplied by a DC source consisting of an AC wall outlet fed through an AC-DC converter. Samples were subjected to FJH treatments using a variety of pre-treatments, voltages, pulse durations, and reaction atmospheres which are included in the full dataset. FJH reactions were conducted inside a desiccator filled with the atmosphere chosen for each reaction. The atmosphere was modulated between argon, CO_2, air, or light vacuum (10 mm Hg), which was not found to have a strong effect on the graphene yield (atmospheres for each individual reaction are tabulated in the full dataset, available on GitHub). The residual voltage after each flash was recorded, resulting in an initial voltage value (V_0) and a voltage drop during FJH (ΔV) calculated by subtracting the final voltage from the initial voltage. Resistance of the sample was measured before and after each flash to monitor electrical contact between the electrodes and the sample, as well as to assess changes in the conductivity of the carbon products. Mass yields of >80% were typically observed, though this was dependent on the chosen feedstock. Pulse duration was modulated by insulated gate bipolar transistors (IGBTs) with programmable millisecond-level delay time that were connected to a Hall effect sensor through an inductor and controlled via custom *LabView* scripts. The Hall effect sensor was employed to collect information about current fluctuations over time (time-current curves). These time-current curves were then analyzed *via* custom-written Python scripts to provide features for the machine learning models.
NOTE: The FJH reaction employs high voltage with possibility of electric shock or electrocution. See the SI for a detailed discussion of safety protocols and component selection considerations.

Material Characterization and Analysis

Raman Spectral Mapping

Wide-area Raman spectral mapping was chosen as the principal metric of characterization for this study. Spatial inhomogeneities can bias results obtained from low numbers of sample spectra taken from small areas. Hence, mapping was employed in an area of 1 mm^2, with a minimum of N = 64 spectra per map. Spectra were taken with a Renishaw inVia Raman microscope through a 50x lens and using a 5 mW 532 nm Nd:YAG laser for excitation. Renishaw Wire 5.5 LiveTrack software was used to maintain laser focus across large areas. Maps were analyzed *via* custom-written Python scripts employing the RamPy package.[49] Each of the spectra were baseline-corrected using a RamPy polynomial fit and smoothed using a Savitsky-Golay filter prior to analysis. Each Raman spectrum was classified as either "graphene" or "amorphous carbon" based on I_{2D}/I_G ($I_{2D}/I_G > 0.3$), the full-width at half max of the 2D band ($15 < FWHM_{2D} < 70$ cm^{-1}), and the signal-to-noise ratio ($SNR_{2D} > 8$). Spectra without a sufficiently strong G band ($SNR_G > 8$) were attributed to poor focusing of the laser beam and were not included in the analysis. The "graphene yield" (GY) metric for each sample was calculated as the total number of Raman spectra classified as graphene divided by the total number of Raman spectra taken of that sample, giving an approximate numerical indicator of the sample's bulk crystallinity.

Additional Characterization

Scanning electron micrographs were taken with an FEI Helios Nanolab 660 Dual-Beam Scanning Electron Microscope operating in immersion mode and using a through-the-lens detector optimized for high secondary electron yield. Thermogravimetric analysis was conducted using a

Q-600 Simultaneous TGA/DSC from TA instruments. A temperature ramp of 10 °C min^{-1} was employed in air. X-ray diffraction (XRD) spectra were taken using a Rigaku SmartLab II using a zero-background holder, a scan rate of 8º per min, and step size of 0.005º per step. X-ray photoelectron spectroscopy was conducted using a PHI Quantera X-ray Scanning Microprobe. C 1s and Auger spectra were collected at a step size of 0.1 eV.

Machine Learning (ML)

ML models

A total of six different types of ML models (BR, LR, MLP-R, DT-R, RF-R, and XGB-R) were trained to predict graphene yield. All models were constructed directly in Python using the package Scikit-Learn. Models were trained on 80% of the initial dataset and tested on the remaining 20%. Hyperparameter optimization was performed using 5-fold cross validation. Models with variable performance at different random seeds using the train/test split method were trained in five separate instances, and their performance was reported as mean $\pm$ standard deviation. Partial dependence was calculated using the Scikit-Learn extension for PD. All data was retained except for FJH reactions where quartz tubes shattered, resulting in loss of sample. This occurred ~5% of the time. All data was made publicly available following suggested guidelines.[50]

Feature Engineering.

Features were empirically selected based on their predictive efficacy in regression models for graphene yield. Five selected features included the charge density (CD), materials type (M), the area under the time-current curve normalized to the mass (A_{IT}), the maximum current value normalized to the mass (I_{max}), and the final current value divided by the maximum current value (I_F/I_{max}).

CD is defined as Equation (1):

$$CD = \frac{V_0 \times C}{m} \qquad \text{(Equation 1)}$$

where V_0 is the voltage, C is the capacitance of the system, and m is the mass of the precursors. M constitutes the starting material employed in each flash and is separated using one-hot encoding. A_{IT} was calculated by trapezoidal integration of the discharge curve collected by a Hall effect sensor. As mentioned in the discussion of **Figure 3.3**, A_{IT} and CD are conceptually similar quantities with the same units, but they convey different information about the system. The calculation of CD uses the initial voltage V_0. By contrast, measurement of A_{IT} depends on the voltage drop during the reaction ΔV. V_0 and ΔV are different values because complete discharge was rare in the FJH reactions run in this study. They differ by the value of the residual voltage. An alternative version of CD was constructed using the voltage drop ΔV instead of the initial voltage V_0, but this metric was less predictive of crystallinity (**Table A3.2**) and correlated strongly with A_{IT} (Pearson's correlation coefficient of r = 0.85).

I_{Max} was calculated as the maximum current recorded in the discharge divided by the mass. I_F/I_{Max} was calculated as the final recorded current in the flash divided by the maximum current. A visual depiction of how each of the time current curve-derived features were calculated can be found in **Figure 3.3a**. The five selected features were empirically chosen based on their ability to improve model performance. Other features attempted are tabulated in **Table A3.2**. These features

were not included in the final model for one of two reasons: (i) decreased model performance or (ii) high correlation with existing features.

Evaluation metrics.

All regression evaluation metrics were calculated using existing Scikit-Learn plugins. The r^2 score was chosen as the principal metric due to its ability to compare model performance over a performance baseline (a model that predicts the mean output value for every sample). The r^2 score is defined as Equation (2):

$$r^2 = 1 - \frac{\sum_{i=1}^{n}(y_i - \hat{y}_i)^2}{\sum_{i=1}^{n}(y_i - \overline{y}_i)^2} \qquad \text{(Equation 2)}$$

Where y_i is the true value of each sample, $\hat{y}_i$ is the value predicted by the model, and $\overline{y}_i$ is the mean output value. RMSE values were also reported.

Data Inclusion.

At the spectra-level, all spectra identified as having a G peak (a maximum in the range of 1500 $cm^{-1} < x < 1700\ cm^{-1}$ with a signal-to-noise ratio of >8) were included in the analysis. Spectra not containing a G peak were attributed to poor laser focusing. At the individual sample level, all samples with >64 viable spectra, a properly recorded accompanying current/time profile, and which did not cause an explosion of the quartz tube were included in the analysis.

Bayesian Optimization.

Bayesian model-based optimization was implemented in R using the package mlrMBO.[51] Graphene yield (GY) was defined as the objective function, and the sample pre-treatment, voltage, pulse time, mass, and capacitance of the FJH reaction were defined as the inputs. All experiments were performed with carbon derived from pyrolyzed rubber tires. The default RF-R with 500 trees was defined as the surrogate model. Since the number of experiments was low (N=30), the acquisition function was modulated between the expected improvement (EI) and augmented expected improvement (AEI) functions in a human-in-the-loop configuration to encourage exploration of the parameter space.

Code and Data Availability

The Python scripts used to construct the dataset and train the models are available at https://github.com/jlb48249/flash Joule heating_ML. The dataset used to derive the findings in this manuscript are available at https://github.com/jlb48249/flash Joule heating_ML/blob/main/flash Joule heating_ML_Final.csv. The R scripts used to train the mlrMBO learner model and generate partial dependence are available in the same repository. The dataset used for the model-based optimization is available at https://github.com/jlb48249/flash Joule heating_ML/blob/main/flash Joule heating_ML_MBO_Yield2.csv.

References 3.

[1] D. X. Luong, K. V. Bets, W. A. Algozeeb, M. G. Stanford, C. Kittrell, W. Chen, R. V. Salvatierra, M. Ren, E. A. McHugh, P. A. Advincula, Z. Wang, M. Bhatt, H. Guo, V. Mancevski, R. Shahsavari, B. I. Yakobson, J. M. Tour, *Nature* **2020**, *577*, 647.
[2] N. Gupta, S. Walia, U. Mogera, G. U. Kulkarni. *J. Phys. Chem. Lett.,* **2020,** *11,* 8, 2797.
[3] U. Mogera, R. Dhanya, R. Pujar, C. Narayana, G. U. Kulkarni. *J. Phys. Chem. Lett.,* **2015,** *6,* 21, 4437.
[4] W. Chen, Z. Wang, K. V. Bets, D. X. Luong, M. Ren, M. G. Stanford, E. A. McHugh, W. A. Algozeeb, H. Guo, G. Gao, B. Deng, J. Chen, J. T. Li, W. T. Carsten, B. I. Yakobson, J. M. Tour, *ACS Nano* **2021,** *15,* 1282-1290
[5] Y. Yao, Z. Huang, P. Xie, S. D. Lacey, R. J. Jacob, H. Xie, F. Chen, A. Nie, T. Pu, M. Rehwoldt, D. Yu, M. R. Zachariah, C. Wang, R. Shahbazian-Yassar, J. Li, L. Hu, *Science* **2018**, *359*, 1489.
[6] Z. Huang, Y. Yao, Z. Pang, Y. Yuan, T. Li, K. He, X. Hu, J. Cheng, W. Yao, Y. Liu, A. Nie, S. Sharifi-Asl, M. Cheng, B. Song, K. Amine, J. Lu, T. Li, L. Hu, R. Shahbazian-Yassar, *Nat. Comm.,* **2020**, *11*, 1.
[7] W. Chen, J. T. Li, Z. Wang, W. A. Algozeeb, D. X. Luong, C. Kittrell, E. A. McHugh, P. A. Advincula, K. M. Wyss, J. L. Beckham, M. G. Stanford, B. Jiang, J. M. Tour. *ACS Nano* **2021,** *15,* 11158-11167**.**
[8] P. A. Advincula, D. X. Luong, W. Chen, S. Raghuraman, R. Shahsavari, J. M. Tour, *Carbon* **2021**, *178*, 649.
[9] K. M. Wyss, J. L. Beckham, W. Chen, D. X. Luong, P. Hundi, S. Raghuraman, R. Shahsavari, J. M. Tour, *Carbon* **2021**, *174*, 430.
[10] W. A. Algozeeb, P. E. Savas, D. X. Luong, W. Chen, C. Kittrell, M. Bhat, R. Shahsavari, J. M. Tour, *ACS Nano* **2020**, *14*, 15595.
[11] P. Narang, C. A. C. Garcia, C. Felser, *Nat. Mater.,* **2020**, 1, 293.
[12] K. T. Butler, D. W. Davies, H. Cartwright, O. Isayev, A. Walsh, *Nature* **2018**, *559*, 547.
[13] Y. Zhang, C. Ling, *npj Comp. Mater.,* **2018**, *4*, 1.
[14] Y. Dong, C. Wu, C. Zhang, Y. Liu, J. Cheng, J. Lin. *npj Comp. Mater.,* **2019,** *5,* 26.
[15] Y. Dong, D. Li, C. Zhang, C. Wu, H. Wang, M. Xin, J. Chang, J. Lin. *Carbon,* **2020,** *169,* 9.
[16] B. Tang, Y. Lu, J. Zhou, T. Chouhan, H. Wang, P. Golani, M. Xu, Q. Xu, C. Guan, Z. Liu, *Mater. Today* **2020**, *41*, 72.
[17] Y. Xie, C. Zhang, X. Hu, C. Zhang, S. P. Kelley, J. L. Atwood, J. Lin, *J. Am. Chem. Soc.* **2020**, *142*, 1475.
[18] K.-H. Tu, H. Huang, S. Lee, W. Lee, Z. Sun, A. Alexander-Katz, C. A. Ross. *Adv. Mater.,* **2020,** *32,* 52, 2005713.
[19] K. A. Brown, S. Brittman, N. Maccaferri, D. Jariwala, U. Celano. *Nano Lett.,* **2020,** *12,* 1, 2-10.
[20] E. Samaniego, C. Anitescu, S. Goswami, V. M. Nguyen-Thanh, H. Guo, K. Hamdia, X. Huang, T. Rabczuk. *Comput. Methods Appl. Mech. Eng.,* **2020,** *362,* 112790.
[21] C. Anitescu, E. Atroshchenko, N. Alajlan, T. Rabczuk. *Comput. Mater. Contin.,* **2019,** *59,* 345-359.
[22] M. Zhong, K. Tran, Y. Min, C. Wang, Z. Wang, C.-T. Dinh, P. D. Luna, Z. Yu, A. S. Rasouli, P. Brodersen, S. Sun, O. Voznyy, C.-S. Tan, M. Askerka, F. Che, M. Liu, M. Seifitokaldani, Y. Pang, S.-C. Lo, A. Ip, Z. Ulissi, E. H. Sargent. *Nature,* **2020,** *581*, 178-183.
[23] H. Wahab, V. Jain, A. S. Tyrrell, M. A. Seas, L. Kotthoff, P. A. Johnson, *Carbon* **2020**, *167*, 609.
[24] K. Terayama, M. Sumita, R. Tamura, K. Tsuda. *Acc. Chem. Res.,* **2021**, *54*, 1334-1346.
[25] D. Salley, G. Keenan, J. Grizou, A. Sharma, S. Martín, L. Cronin, *Nat. Comm.,* **2020**, *11*, 2771.
[26] A. E. Gongora, B. Xu, W. Perry, C. Okoye, P. Riley, K. G. Reyes, E. F. Morgan, K. A. Brown, *Sci. Adv.,* **2020**, *6*, 1708.
[27] J. M. Granda, L. Donina, V. Dragone, D.-L. Long, L. Cronin, *Nature* **2018**, *559*, 377.
[28] K. Terayama, M. Sumita, R. Tamura, D. T. Payne, M. K. Chahal, S. Ishihara, K. Tsuda. *Chem. Sci.,* **2020**, *11*, 5959-5968.
[29] A. C. Ferrari, *Solid State Comm.,* **2007**, *143*, 47.

[30] L. M. Malard, M. A. Pimenta, G. Dresselhaus, M. S. Dresselhaus, *Phys. Rep.,* **2009**, *473*, 51.
[31] A. C. Ferrari, D. M. Basko, *Nat. Nanotechnol.,* **2013**, *8*, 235.
[32] J. A. Garlow, L. K. Barrett, L. Wu, K. Kisslinger, Y. Zhu, J. F. Puleczio. *Sci. Rep.,* **2016,** *6,* 19804.
[33] I. Kruglov, O. Sergeev, A. Yanilkin, A. R. Oganov, *Sci. Rep.,* **2017**, *7*, 8512.
[34] T. Yamashita, N. Sato, H. Kino, T. Miyake, K. Tsuda, T. Oguchi, *Phys. Rev. Mat.,* **2018**, *2*, 013803.
[35] S. Jaeger, S. Fulle, S. Turk, *J. Chem. Inf. Model.* **2018**, *58*, 27.
[36] M. Ture, F. Tokatli, I. Kurt, *Expert Sys. Appl.,* **2009**, *36*, 2017.
[37] F. Pedregosa, G. Varoquaux, A. Gramfort, V. Michel, B. Thirion, O. Grisel, M. Blondel, P. Prettenhofer, R. Weiss, V. Dubourg, J. Vanderplas, A. Passos, D. Cournapeau. *J. Mach. Learn. Res.,* **2011,** *12,* 2825.
[38] T. Chen, C. Guestrin. *Proceedings of the 22nd ACM SIGKDD International Conference on Knowledge Discovery and Data Mining,* ACM, San Francisco, California, 2016; p. 785– 794
[39] Y. Han, B. Tang, L. Wang, H. Bao, Y. Lu, C. Guan, L. Zhang, M. Le, Z. Liu, M. Wu, *ACS Nano* **2020**, *14*, 14761.
[40] M. Ryo, M. C. Rillig, *Ecosphere* **2017**, *8*, e01976.
[41] P. J. F. Harris, *Carbon* **2017**, *122*, 504.
[42] K. S. Ravi Chandran, *Int. J. Heat Mass Transf.* **2015**, *88*, 14.
[43] J. Y. Huang, S. Chen, Z. F. Ren, G. Chen, M. S. Dresselhaus, *Nano Lett.* **2006**, *6*, 1699.
[44] L. X. Duy, Z. Peng, Y. Li, J. Zhang, Y. Ji, J. M. Tour, *Carbon* **2018**, *126*, 472.
[45] M. G. Stanford, K. V. Bets, D. X. Luong, P. A. Advincula, W. Chen, J. T. Li, Z. Wang, E. A. McHugh, W. A. Algozeeb, B. I. Yakobson, J. M. Tour, *ACS Nano* **2020**, *14,* 10, 13691.
[46] N. T. K. Thanh, N. Maclean, S. Mahiddine. *Chem. Rev.,* **2014,** *114,* 15, 7610.
[47] R. W. Epps, M. S. Bowen, A. A. Volk, K. Abdel-Latif, S. Han, K. G. Reyes, A. Amassian, M. Abolhasani. *Adv. Mater.,* **2020,** *32,* 30, 2001626.
[48] J. L. E. Campos, H. Miranda, C. Rabelo, E. Sandoz-Rosado, S. Pandey, J. Riikonen, A. G. Cano-Marquez, A. Jorio. *J. Raman Spectrosc.,* **2018**, *49*, 54-65.
[49] C. L. Losq. (2018, February 7). Rampy: A Python Library for Processing Spectroscopic (IR, Raman, XAS.) Data. Zenodo.
[50] N. Artrith, K. T. Butler, F.-X. Coudert, S. Han, O. Isayev, A. Jain, A. Walsh, *Nat. Chem.* **2021**, *13*, 505
[51] B. Bischl, J. Richter, J. Bossek, D. Horn, J. Thomas, M. Lang. (2017). mlrMBO: A Modular Framework for Model-Based Optimization of Expensive Black-Box Functions. 1703.03373

Appendix 3.

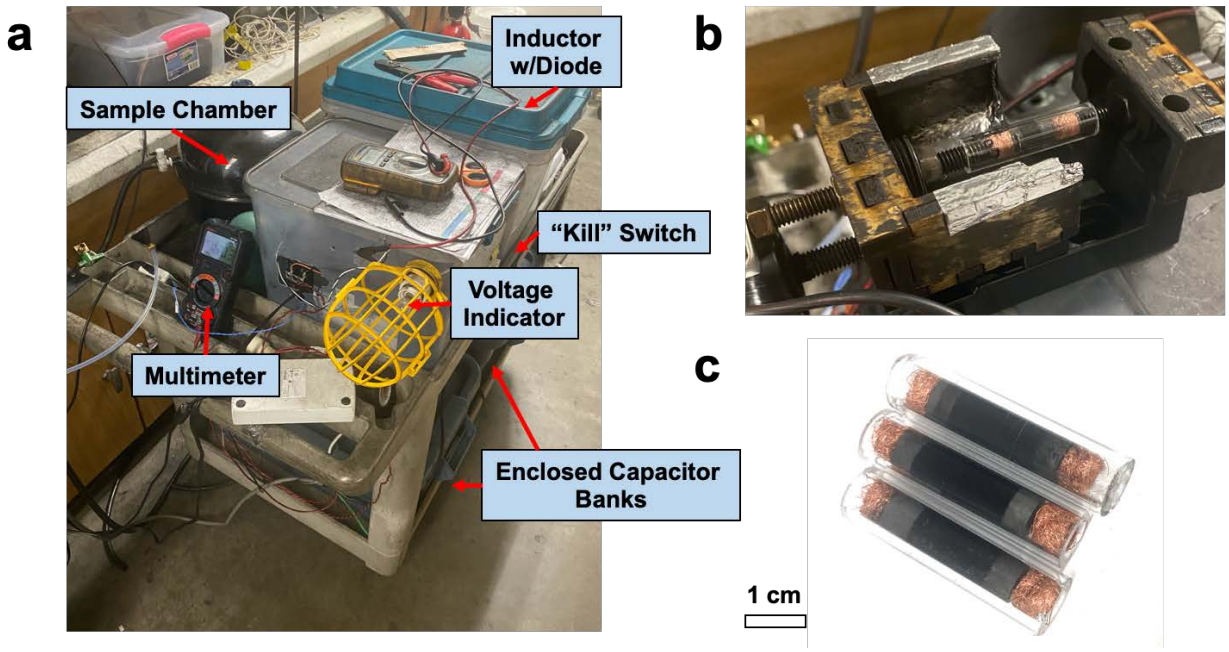

Figure A3.1. Schematic of the custom FJH station used for this study. **(a)** FJH apparatus. **(b)** Sample holder **(c)** sample tubes with carbon starting material, graphite electrodes, and copper electrodes around them.

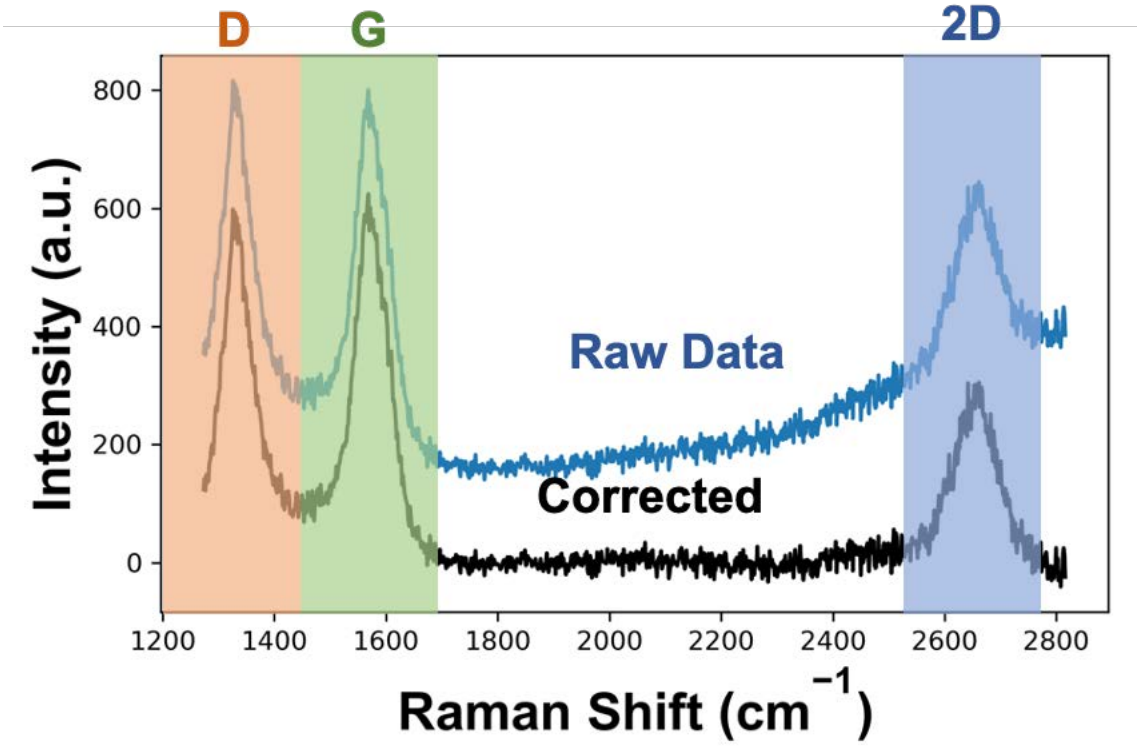

Figure A3.2. Sample pre-processing (background subtraction and smoothing) of individual Raman spectra. The background subtraction of spectra from Raman mapping is essential for accurate calculation of peak ratios and reporting of graphene yield.

Raman Spectra Interpretation and Use of Graphene Yield as a Metric of Crystallinity

Figure A3.3 shows an analysis of the heterogeneity of flash graphene samples as related to other forms of graphene. Commercially available graphene nanoplatelets (GNPs) and synthesized laser-induced graphene (LIG) were analyzed using the same Raman mapping protocol used to analyze flash graphene samples. Average Raman maps with plotted standard deviation reveal that flash graphene samples are noticeably more heterogeneous, indicating that the FJH process is not consistent throughout the bulk of the sample. This observation that the Raman spectra differed widely between and within samples led us to use a threshold value for I_{2D}/I_G and a compositional percentage to approximate crystallinity. While Raman spectra are complex and provide a wealth of information about each sample, in this case each Raman spectrum represents a composite of the spectral fingerprint of many different nanocrystals under the irradiation area of an Nd:YAG laser (~2 μm diameter). Many different particles, including graphene crystals and amorphous carbon, can be present in this area at the same time, all of which contribute to the overall spectrum. An I_{2D}/I_G of 0.3 provides a cutoff point that is well above the value reached by any unreacted amorphous carbon samples (~0.07) and is comparable to values achieved by commercial sources of graphene.[2] Implementing this threshold results in a metric (graphene yield) that was predictive of the overall properties and quality of a sample. In future studies, principal component analysis can likely be used to reduce the dimensionality of the Raman mapping data, potentially extracting further information than the graphene yield approximation can offer.

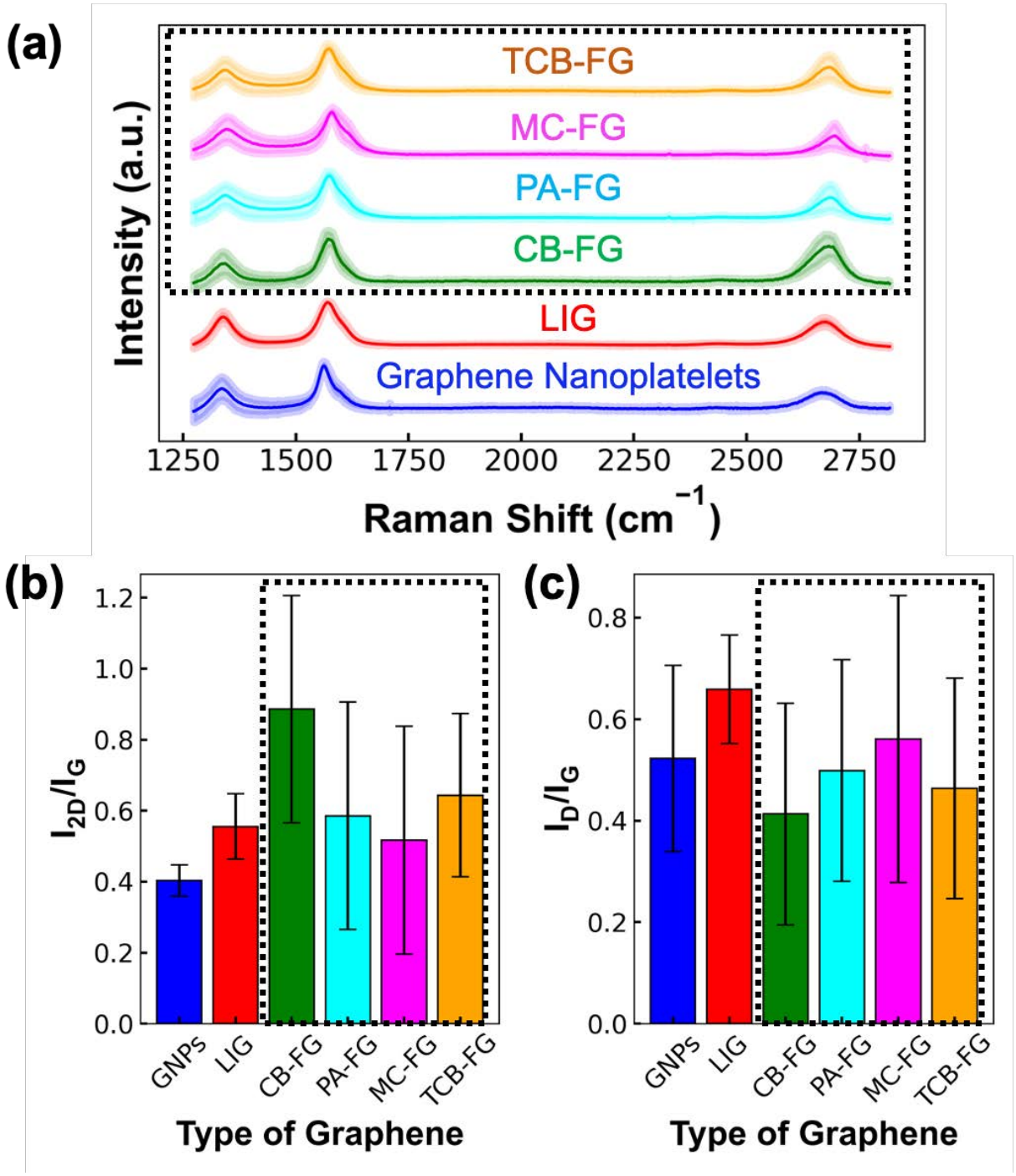

Figure A3.3. Analysis of heterogeneity in samples of graphene derived from various sources. **(a)** Average Raman spectra obtained from samples of commercially available graphene nanoplatelets, laser-induced graphene (LIG),[1] and flash-synthesized graphene from each feedstock employed in this study. LIG was chosen as an additional comparison due to the comparable timescale of the graphene formation process. The shaded regions represent +/- one standard deviation. The flash graphene samples selected were the highest-yield samples obtained from each individual feedstock. Each Raman map was taken with 100 spectra in a 1 mm^2 area. **(b)** I_{2D}/I_G values obtained

from 120 spectra from a single sample of each type of graphene. **(c)** I_D/I_G values obtained from graphene derived from various sources. Samples inside the dotted box represent graphene synthesized by FJH.

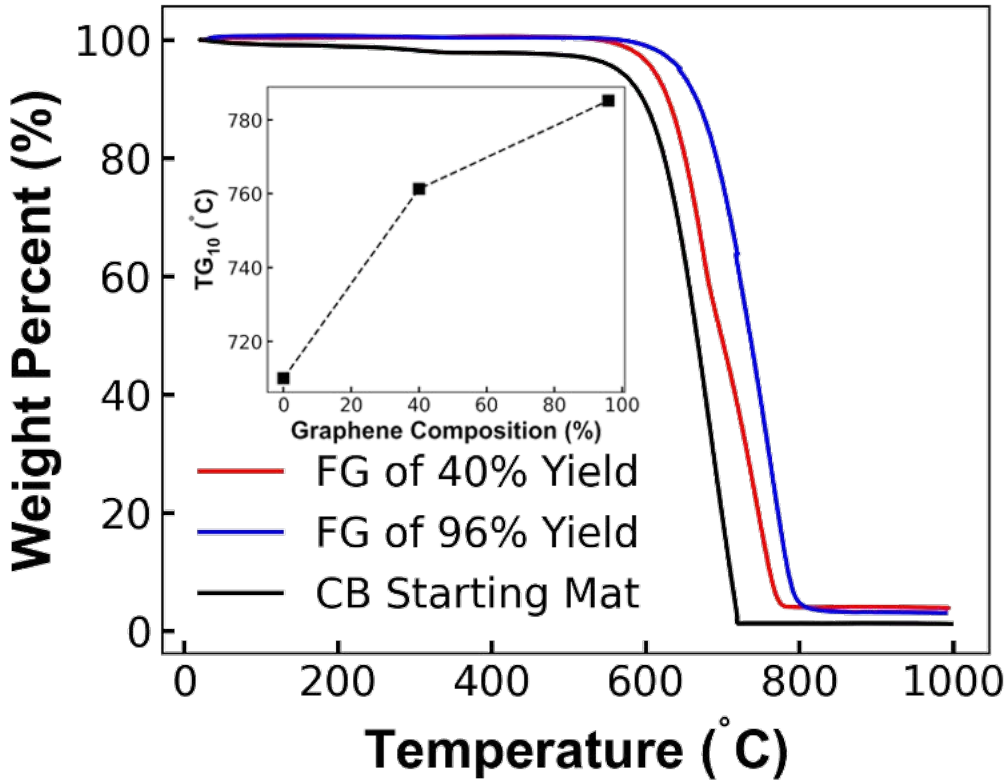

Figure A3.4. The thermal stability of flashed materials generally increases as the measured graphene yield increases. Plot shows TG curves of CB and CB derived flash graphene (FG) pyrolyzed in air. The inset shows the temperature at which each sample reaches 10 wt% plotted against the graphene yield.

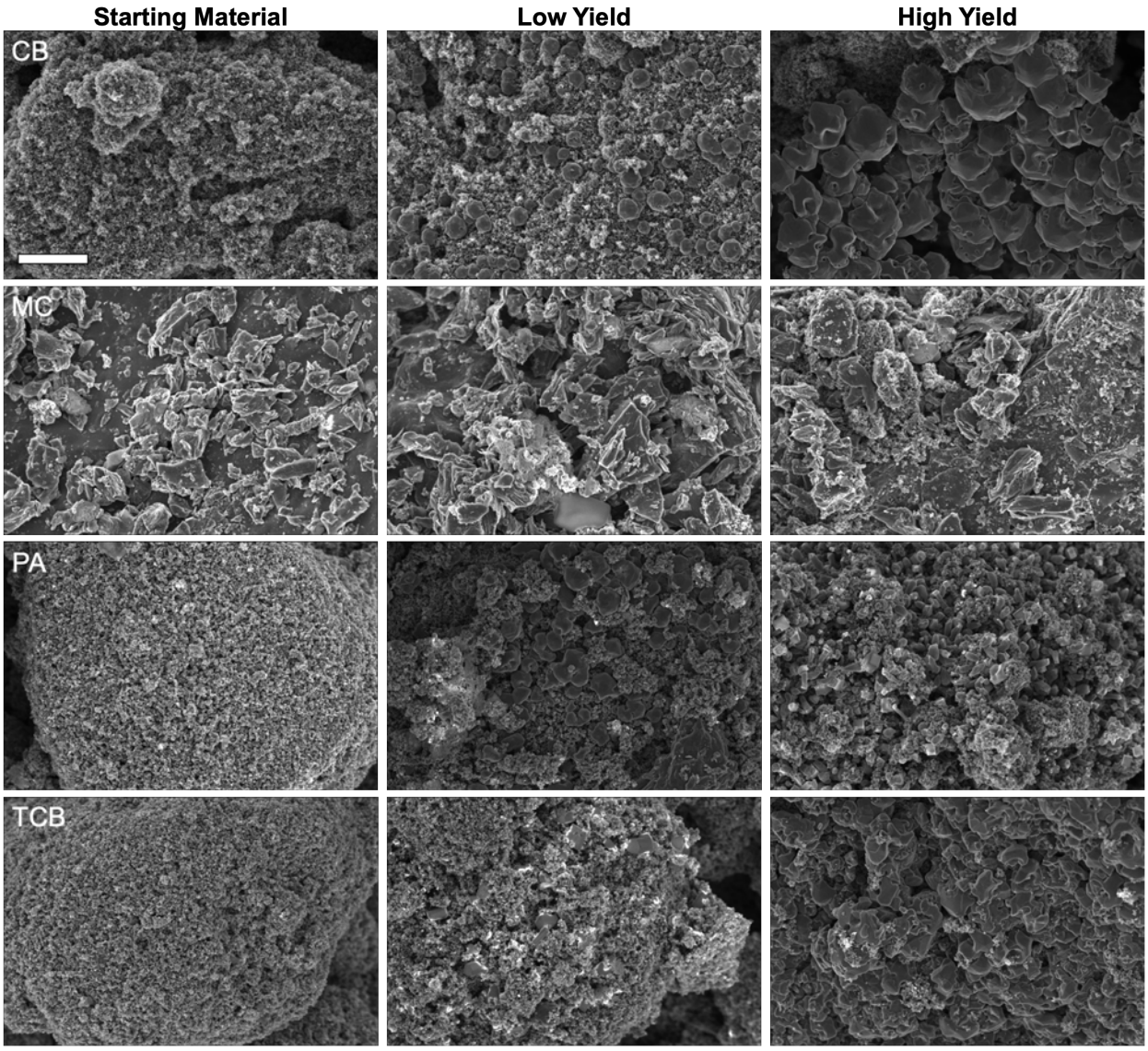

Figure A3.5. Scanning electron micrographs of flashed and unflashed material from each feedstock, correlating the graphene yield measured by Raman spectroscopy ("low" or "high") with the crystallinity observed under SEM. The scale bar applies to all images and is 2 μm. Microstructural evolution in MC is likely less noticeable due to the large particle size and pre-flash calcination in the commercial generation of MC from bituminous coal. CB: carbon black; PA: pyrolysis ash; MC: metallurgical coke; TCB: tire-derived carbon black.

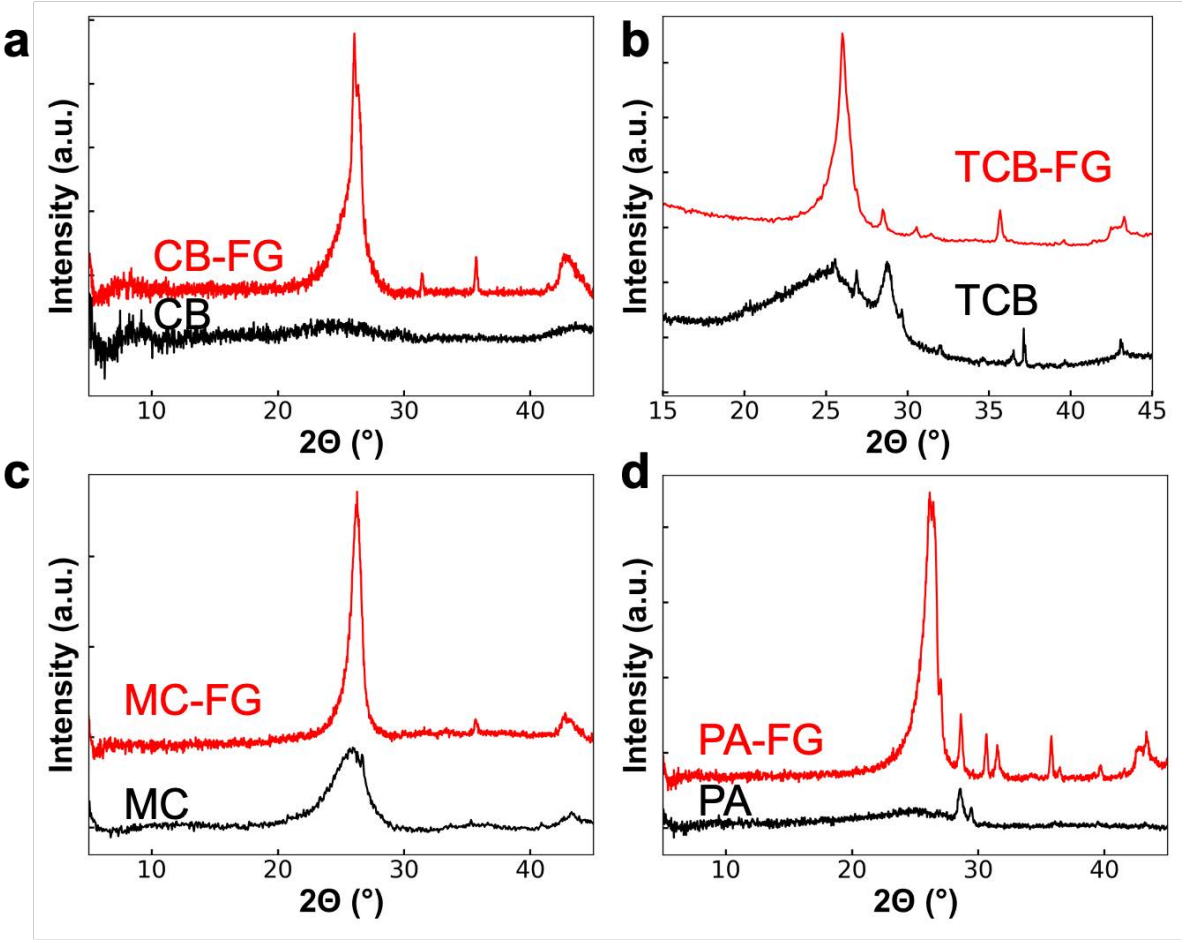

Figure A3.6. X-ray diffraction (XRD) characterization of flashed and unflashed materials of **(a)** carbon black (CB), **(b)** tire carbon black (TCB), **(c)** metallurgical coke (MC), and **(d)** pyrolysis ash (PA), showing the appearance and sharpening of the (002) peak in the XRD spectrum after flashing.

X-Ray Photoelectron Spectroscopic Analysis of Carbon Materials

While the C 1s spectrum of carbon materials is useful for the identification of atoms bonded to carbon (for example, identifying C-O or C=O bonds), identification of sp^2 and sp^3 hybridization using this portion of the XPS spectrum can be difficult.[2] Hence, it is common to quantify the sp^2/sp^3 ratio of carbon nanomaterials using the C KLL spectrum. To accomplish this, the spectrum is commonly differentiated, and the difference (in eV) between the maxima and minima in the resulting curve is quantified. This difference, known as the "d parameter," has been shown to represent the approximate hybridization ratio in the carbon material.[3-5] The d parameter commonly ranges between 13 (for diamond and purely sp^3 C) and 21 (for graphite and purely sp^2 C). The hybridization ratio may be approximated via a linear interpolation between these two extremes. This procedure is expounded on further in reference 3. Here, analysis of the C KLL spectra of flashed materials as compared to unflashed materials demonstrates that the amount of sp^2 carbon increases by ~30-40% in a FJH reaction. This result is comparable to that achieved in our previous studies of FJH.[6]

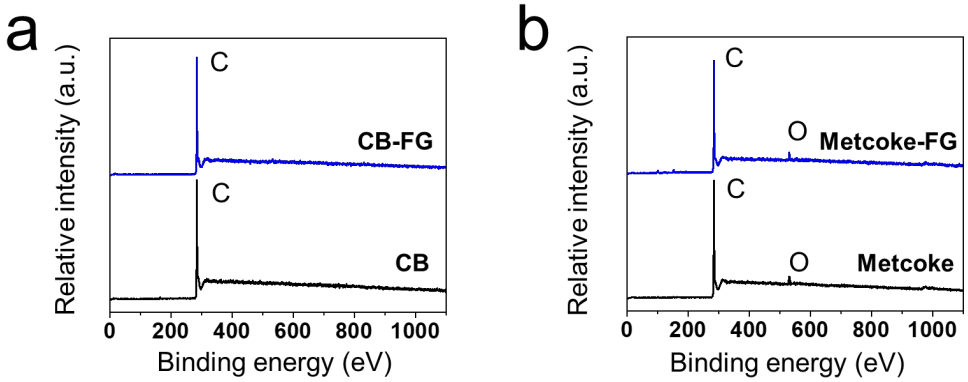

Figure A3.7. X-ray photoelectron spectra of different carbon materials. (a) Carbon black (black) and carbon black-derived flash graphene (blue). (b) Metallurgical coke (black) and metallurgical coke-derived flash graphene (blue).

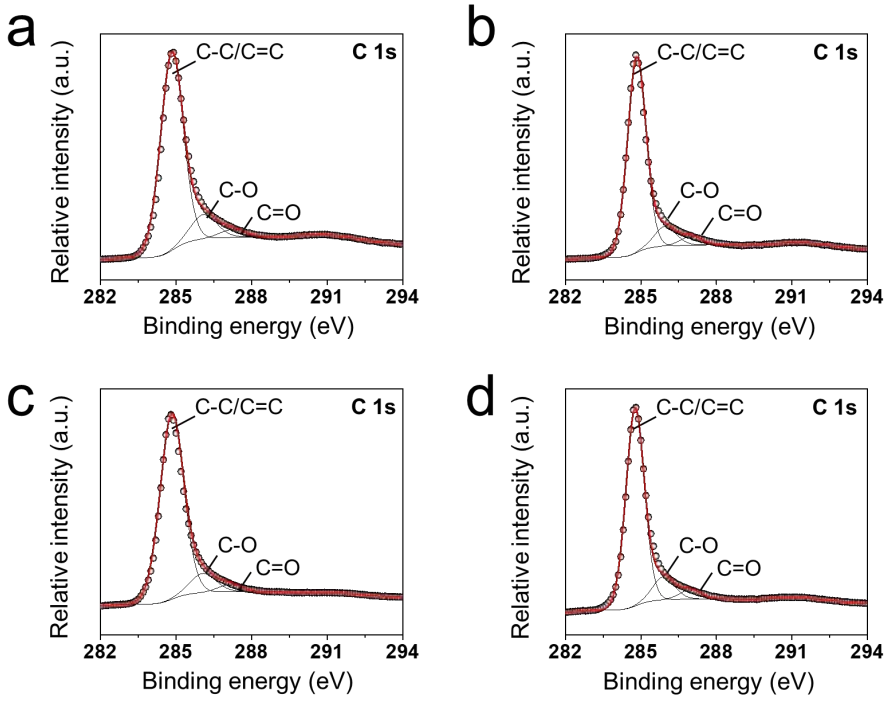

Figure A3.8. High-resolution C 1s spectra of different carbon materials. **(a)** Carbon black. **(b)** Carbon black-derived flash graphene. **(c)** Metallurgical coke. **(d)** Metallurgical coke-derived flash graphene

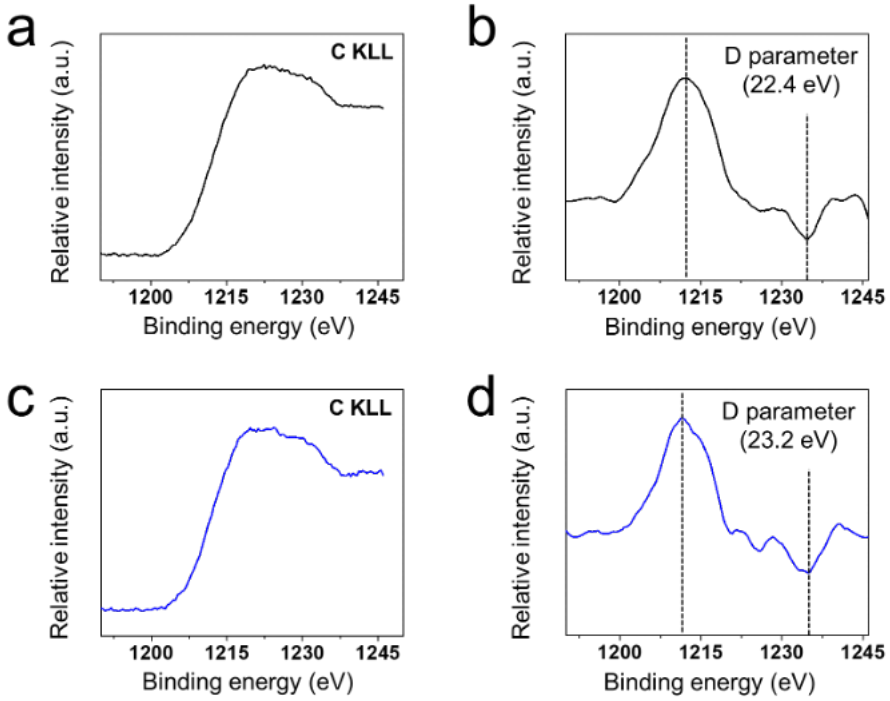

Figure A3.9. The high-resolution C KLL spectra of (a) carbon black and (c) carbon black-derived flash graphene. (b) and (d) are the corresponding derivative curves of the C KLL spectra in (a) and (c). The enhanced D parameter in flashed material indicates a higher prevalence of sp^2 carbon.

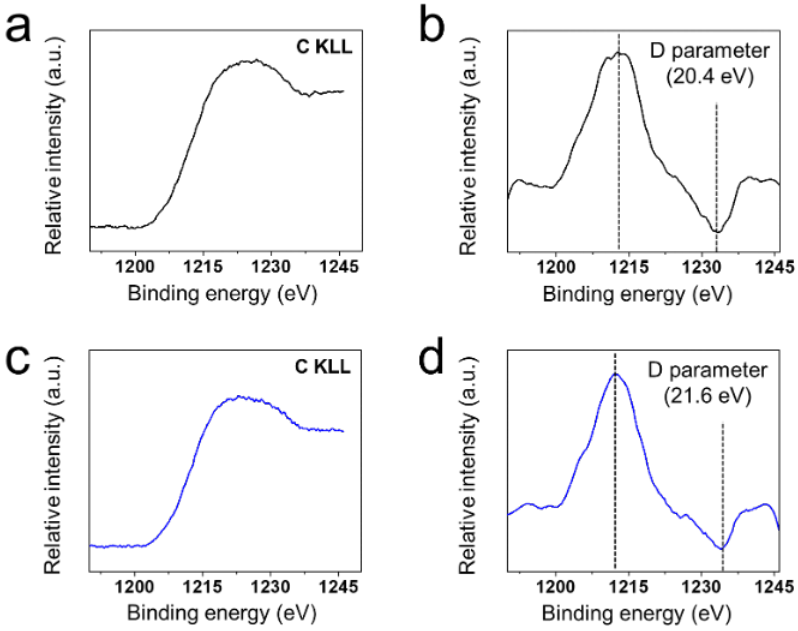

Figure A3.10. High-resolution C KLL spectra of **(a)** metallurgical coke and **(c)** metallurgical coke-derived flash graphene. **(b)** and **(d)** are the corresponding derivative curves of the C KLL spectra

in (a) and (c). The enhanced D parameter in flashed material indicates a higher prevalence of sp^2 carbon.

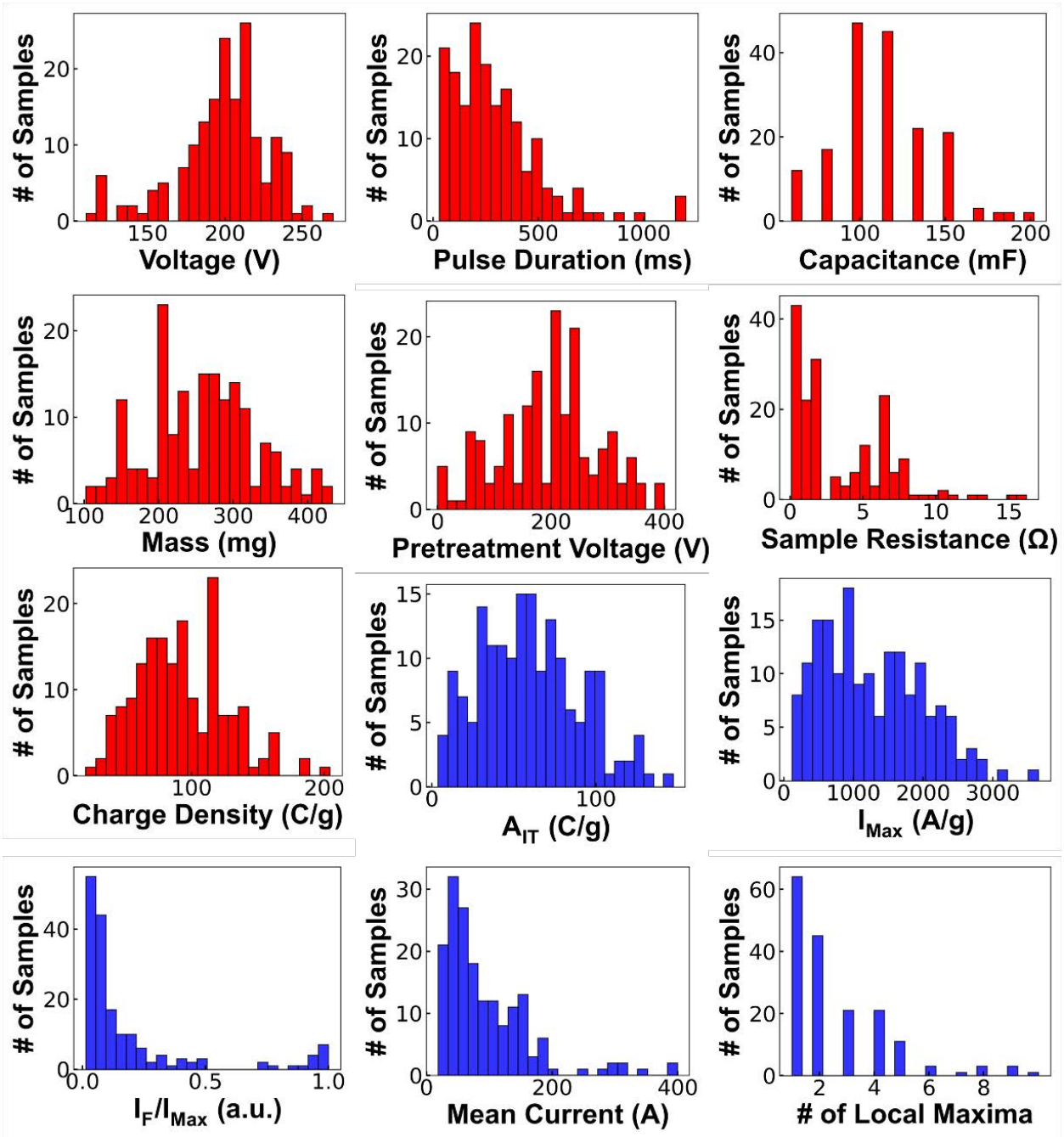

Figure A3.11. Histograms of features tested in ML models. Red histograms represent features collected experimentally. Blue histograms represent features derived from IT curves and calculated using custom scripts.

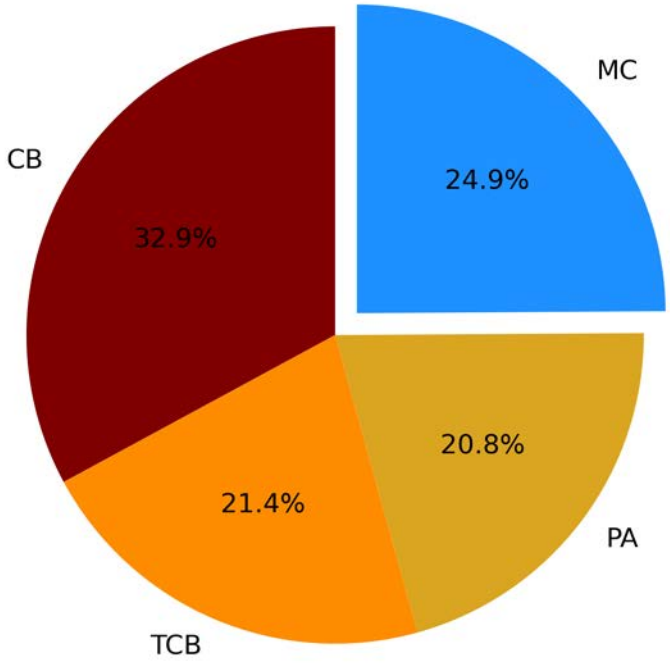

Figure A3.12. Relative contribution of each material type to the final dataset. CB: carbon black; PA: pyrolysis ash; MC: metallurgical coke; TCB: tire-derived carbon black.

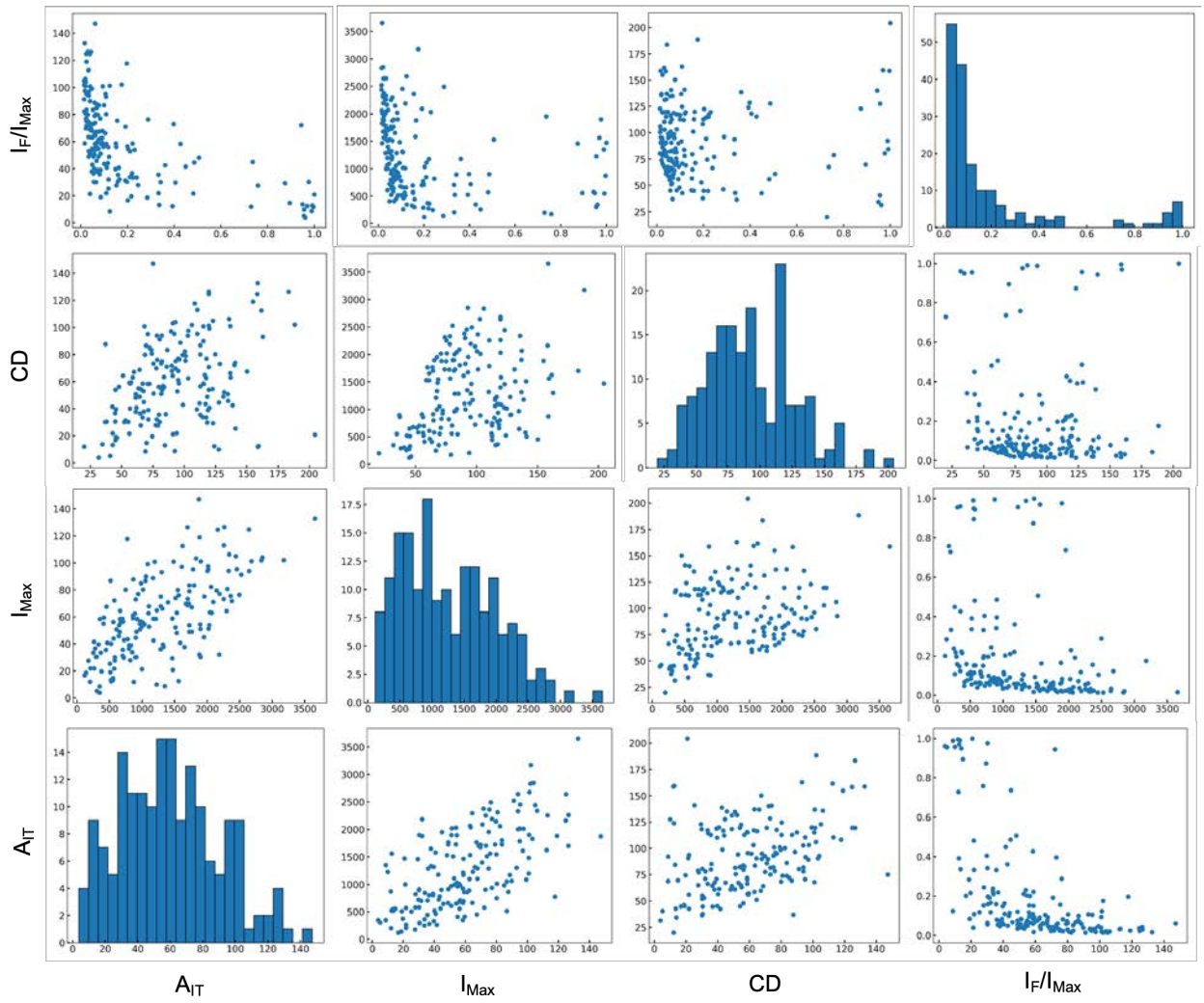

Figure A3.13. Map of all quantitative features plotted against each other for all the samples used to train and test the model.

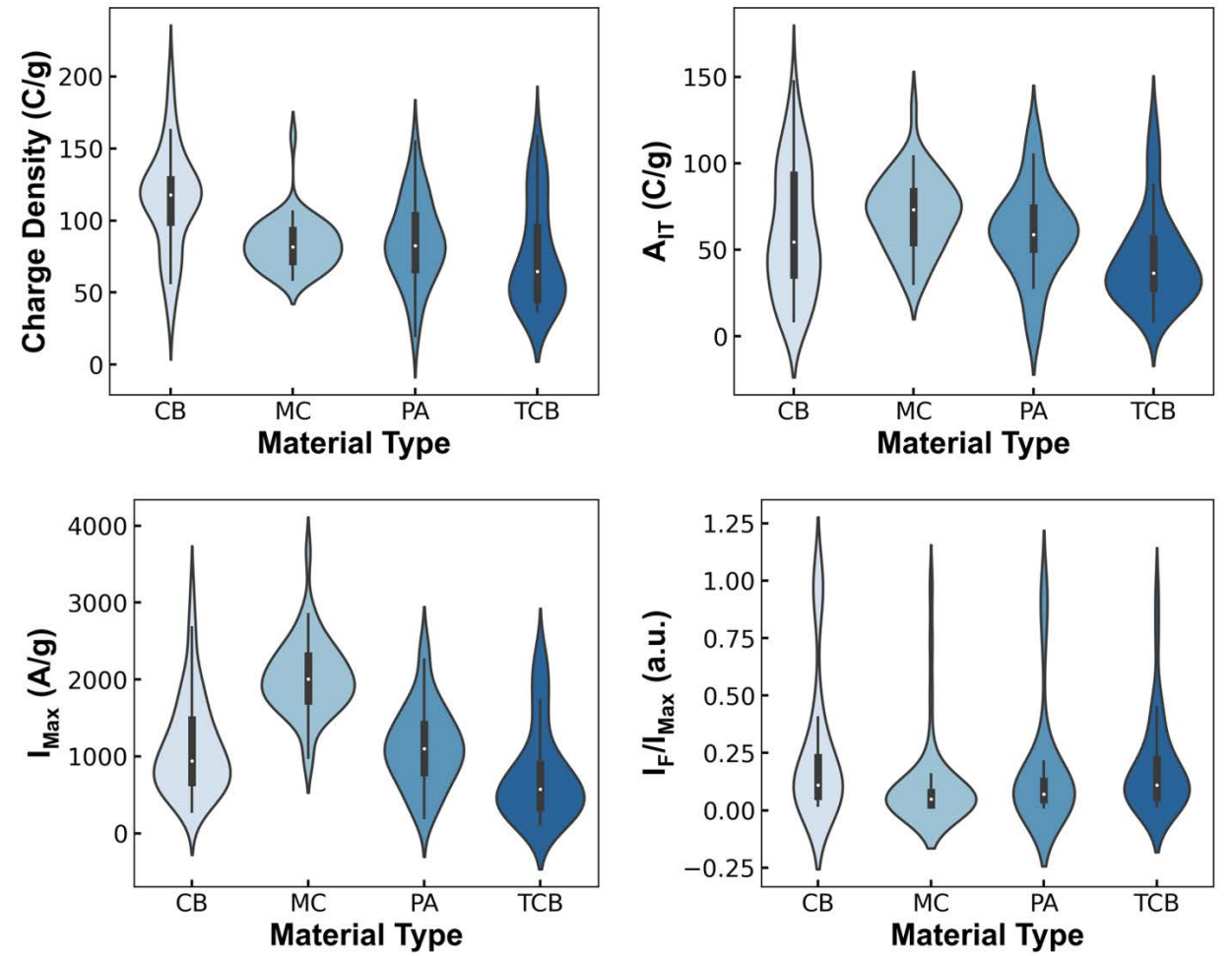

Figure A3.14. Violin plots showing correlations between material type and the quantitative features. Violin plots can be considered a combination of the box plot with a kernel density plot. The median is shown as a white dot on the violin plot; the interquartile range (IQR) is shown as the black bar in the center of violin; the lower/upper adjacent values are shown as black lines stretched from the bar defined as first quartile. Lower and upper adjacent values are defined as the first quartile minus 1.5 times the IQR and third quartile plus 1.5 times the IQR, respectively.[7]

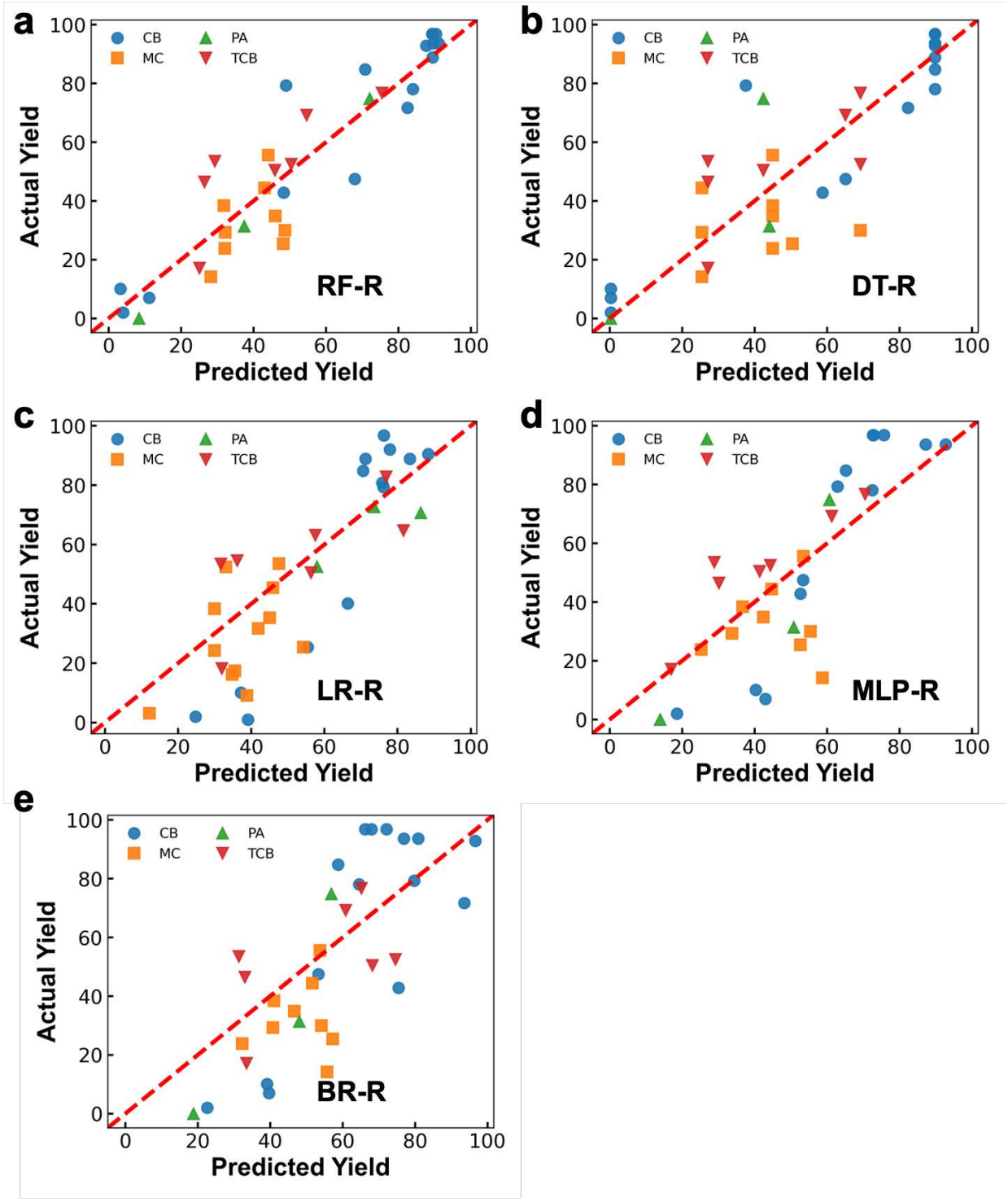

Figure A3.15. Sample performance of **(a)** RF-R (r^2 = 0.85) **(b)** DT-R (r^2 = 0.73) **(c)** LR-R (r^2 = 0.65), **(d)** MLP-R (r^2 = 0.56), and **(e)** BR-R (r^2 = 0.52) models.

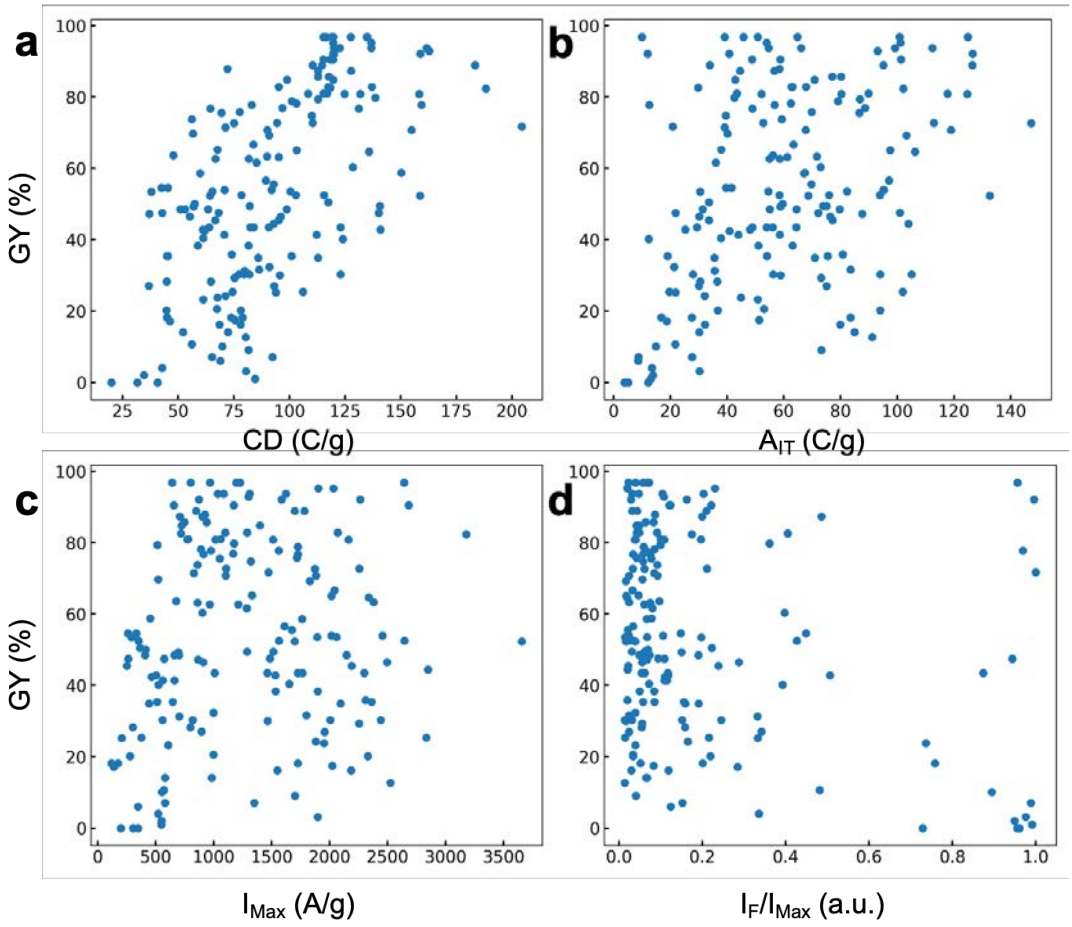

Figure A3.16. Plots of **(a)** CD, **(b)** A_{IT}, **(c)** I_{Max}, and **(d)** I_F/I_{Max} against the graphene yield (GY). The most linearly correlated feature is CD (Pearson's Correlation Coefficient of 0.62). A_{IT} had a PCC of 0.38, I_{Max} had a PCC of 0.13, and I_F/I_{Max} had a PCC of -0.27.

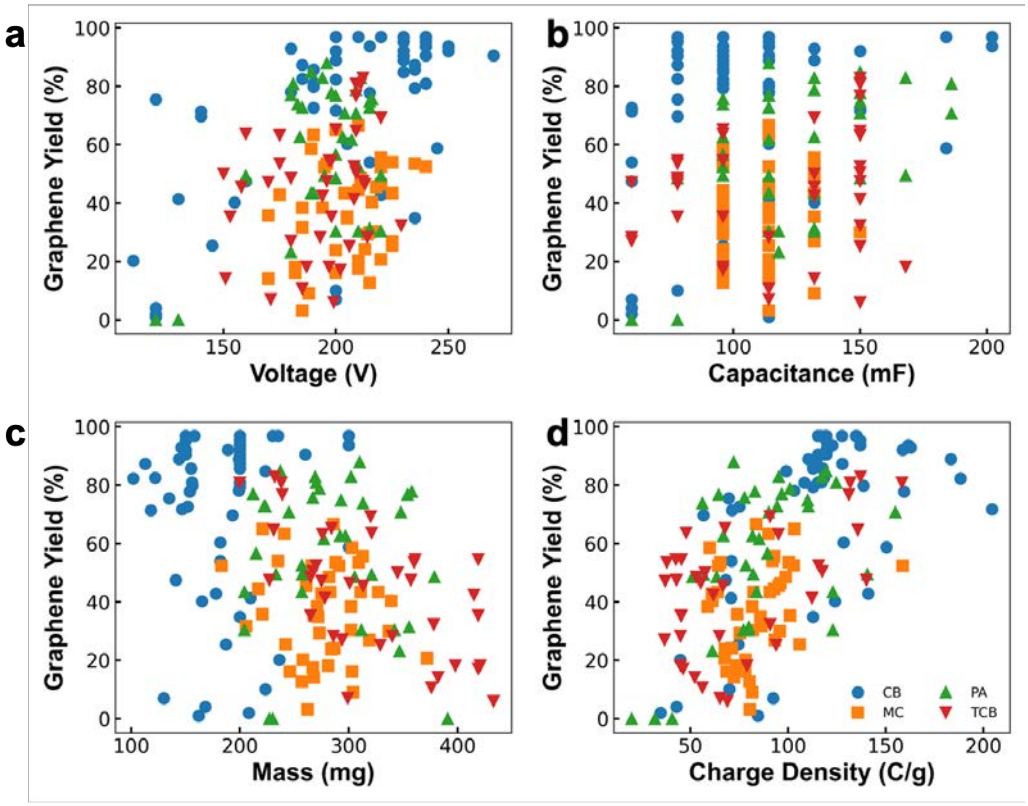

Figure A3.17. Plots of voltage, capacitance, mass, and charge density (V×C/m) against the graphene yield.

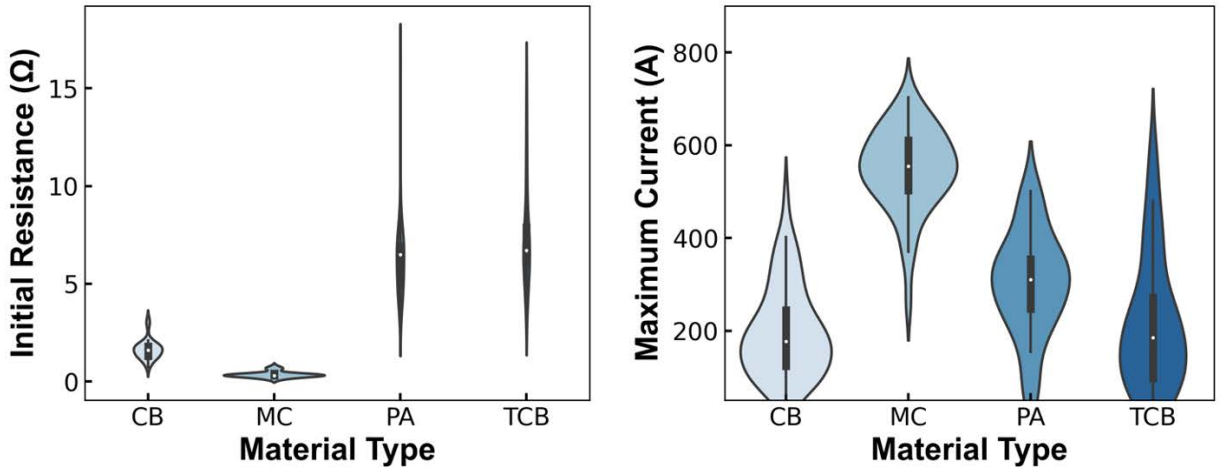

Figure A3.18. Violin plots of the initial resistance and peak current amongst each starting material. Note that maximum current in the right plot is distinct from the feature incorporated in the ML models in that it is not normalized to the sample mass.

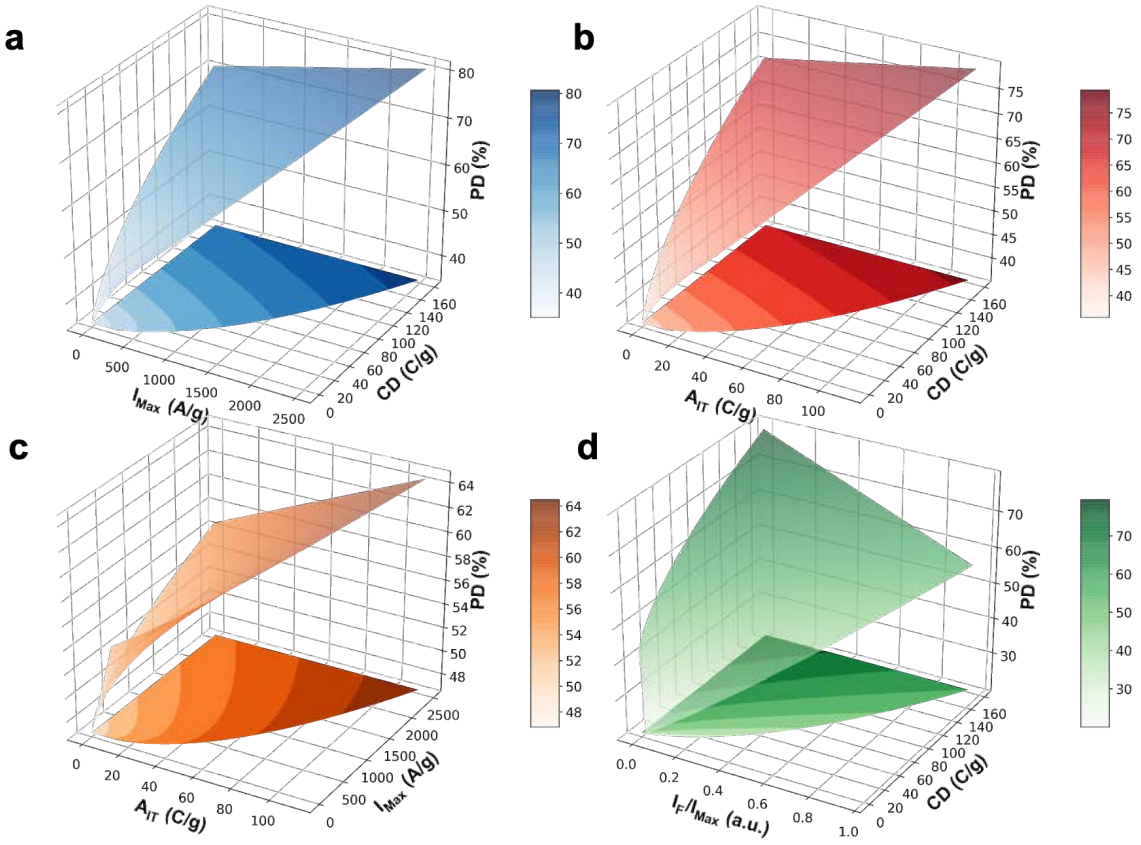

Figure A3.19. PDPs of a linear regression model of graphene yield (r^2 = 0.65). The shape of the PDP relationships reflects the nature of the algorithm used to construct them. Hence, PDPs derived from a linear model show a smooth relationship between each parameter and the PD, while a decision tree model produces a PDP with "wrinkles" corresponding to the nodes of prominent decision trees (**Figure 3.4**).

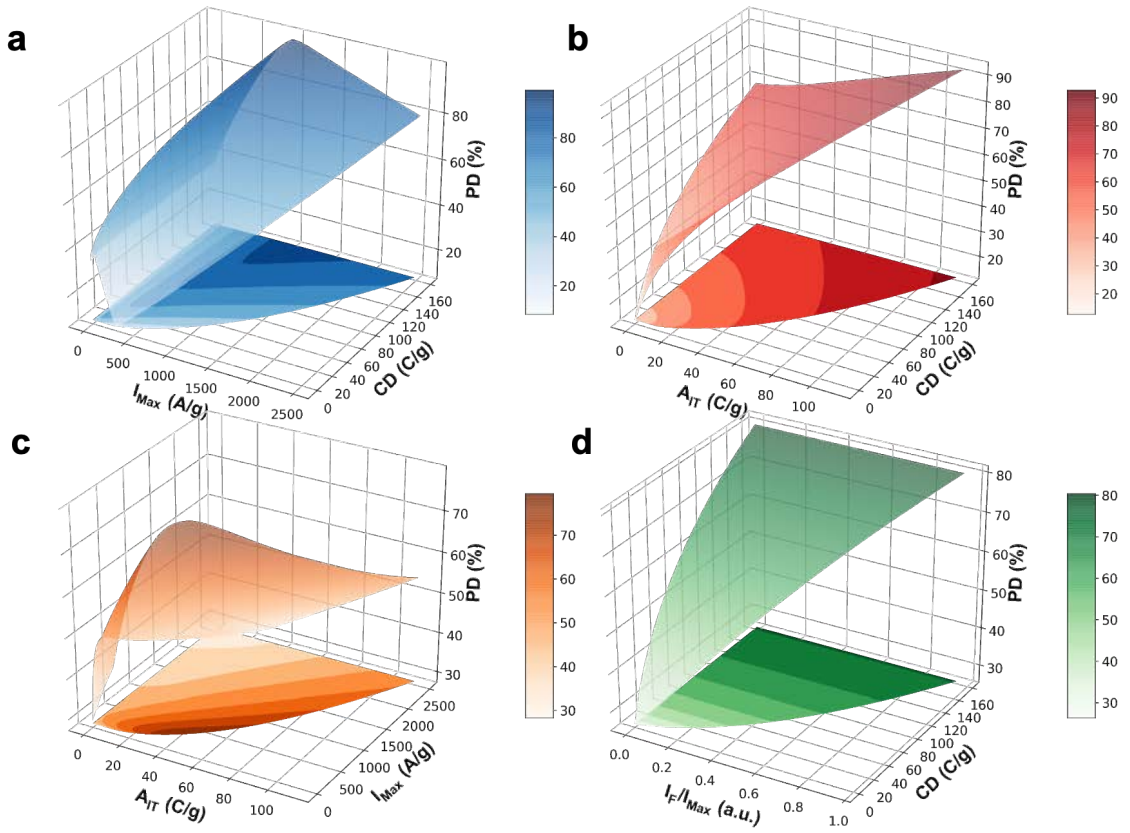

Figure A3.20. PDPs of a multilayer perceptron model of graphene yield ($r^2 = 0.55$).

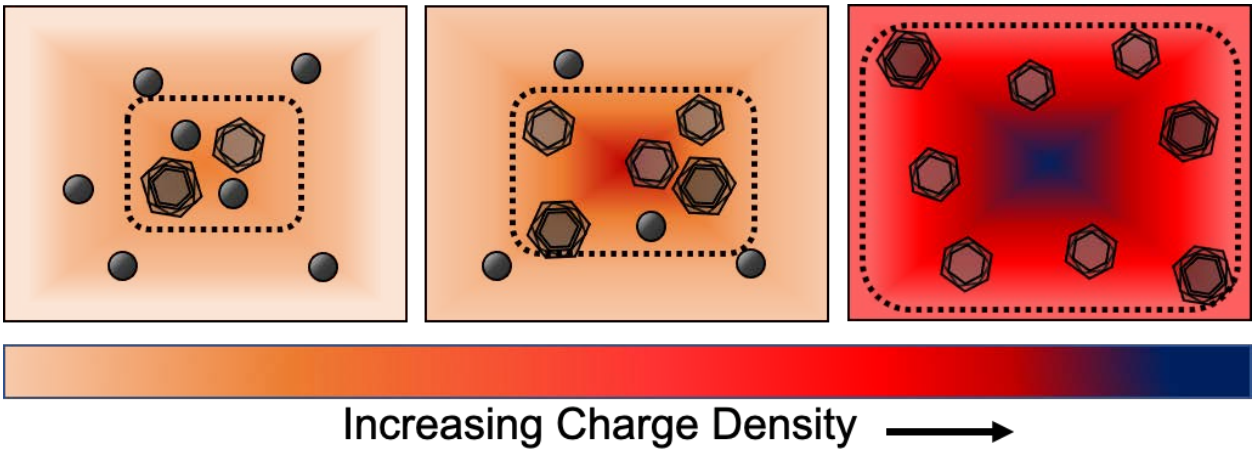

Figure A3.21. Scheme of how increasing energy density affects crystallinity in a FJH reaction.

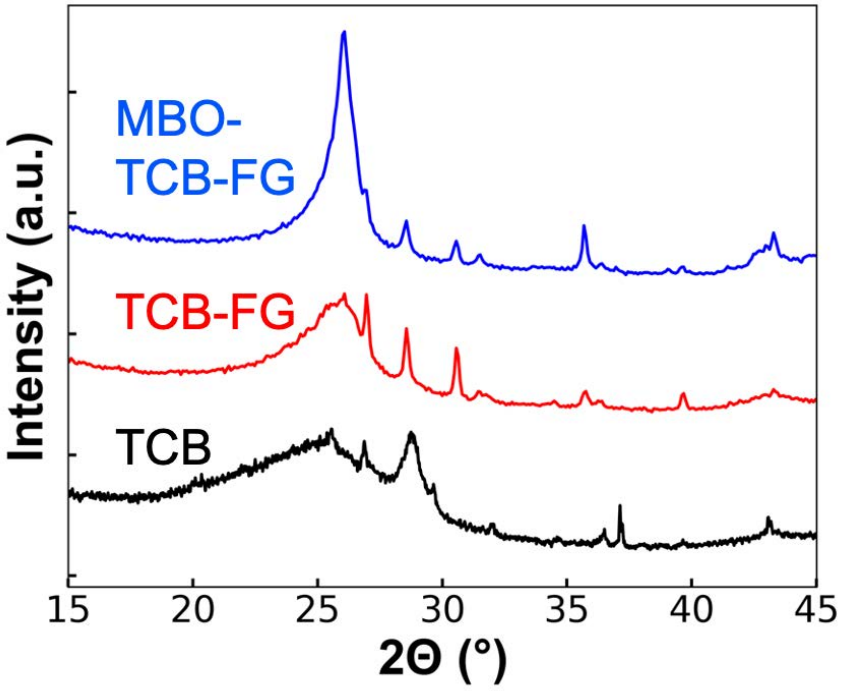

Figure A3.22. X-ray diffraction analysis of tire carbon black (TCB), tire carbon black-derived flash graphene (TCB-FG), and tire carbon black-derived flash graphene after model-based optimization (MBO-TCB-FG). The red line (TCB-FG) represents flash graphene made with randomized parameters (the first sample flashed) and the blue line (MBO-TCB-FG) represents a sample made with "optimized" parameters (the last sample flashed). The MBO-selected parameters used to synthesize MBO-TCB-FG shown here are as follows: 203 V, 233 mg, 150 mF capacitance, a pulse time of 256 ms and three pre-flash treatments of 50, 75, and 100 V, sequentially. The randomly selected parameters used to synthesize TCB-FG are as follows: 199 V, 433 mg, 150 mF capacitance, a pulse time of 68 ms, and one pre-flash treatment of 85 V.

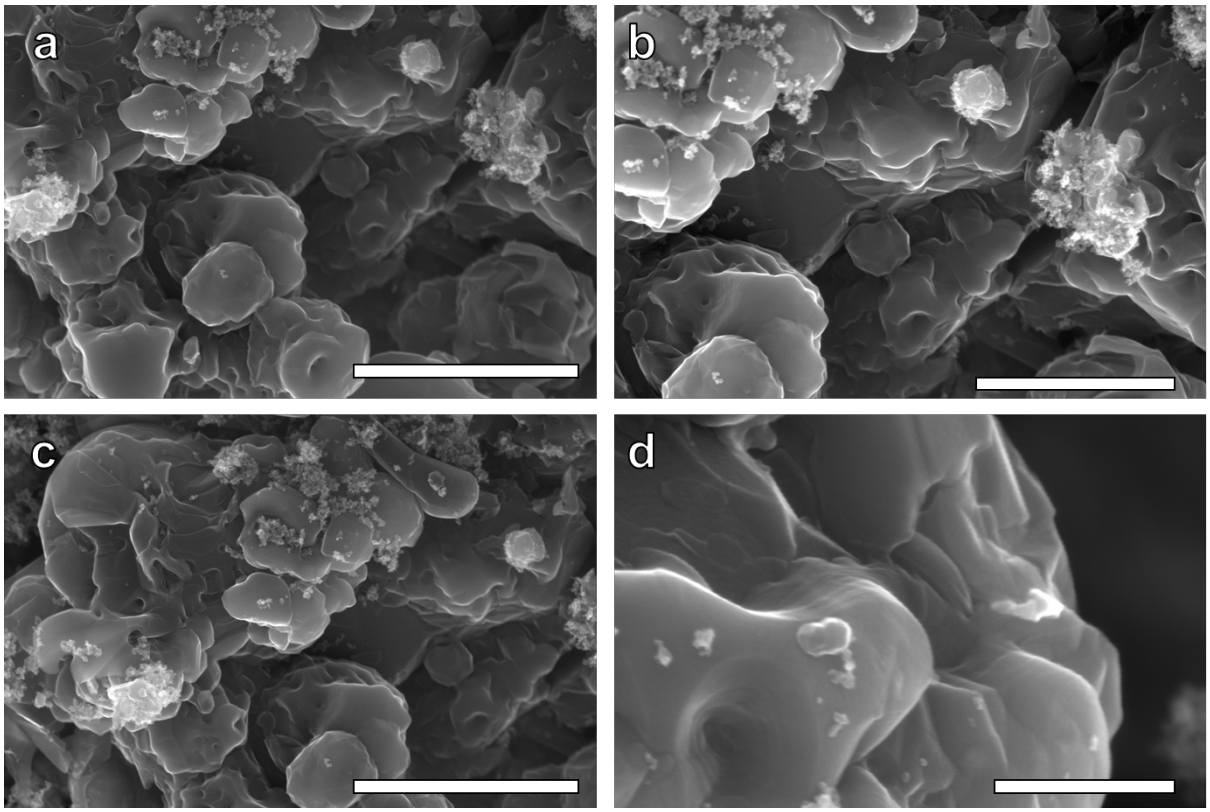

Figure A3.23. Scanning electron micrographs of optimized tire carbon black-derived flash graphene (MBO-TCB-FG in **Figure A3.19**). Scale bars are as follows: **(a)** 3 μm, **(b)** 2 μm, **(c)** 3 μm, **(d)** 500 nm.

Table A3.1. Various element content in different carbon materials determined by XPS survey spectral analysis

Materials	C	O	S	Si	D parameter
CB	98.6%	0.7%	0.7%	0	22.4 eV
CB-FG	98.5%	1.5%	0	0	23.2 eV
MC	95.2%	4.8%	0	0	20.4 eV
MC-FG	94.2%	3.6%	0	2.3%	21.6 eV

Table A3.2. Variations on the trained XGB-R model and their effects on model performance.

Change	Rationale	Result
Using V_0^2 instead of V_0 for CD	V_0^2 is more indicative of the potential energy being released by the capacitor.	r^2 drops by ~0.1-0.2; RMSE increases.
Using ΔV for CD instead of V_0	Metric would represent the amount of physical charge passing through the sample.	r^2 drops by ~0.1 to 0.2.
Separating out CD into its constituent parts: mass, voltage, capacitance	-	r^2 drops by ~0.15. RMSE increases. Model particularly struggles to pick up on low-yield carbon black samples.
Same as above but replace mass with $mass^{-1}$	Inverse correlation to mass	Inverse of mass accrues some feature importance, but models do not attain the same accuracy as they do with CD.
Using only features derived from experimental parameters	-	Typical r^2 of 0.6. Noticeably diminished performance.
Using only features derived from IT curves	-	Typical r^2 of 0.4.
Addition of pulse time as a feature	Previous observation of morphological evolution with increasing t[8]	Model performance decreases slightly due to overfitting; pulse time has ~0% feature importance (might be accounted for by I_F/I_{Max})
Addition of local maxima/minima in IT curve as a feature	Indicative of sample outgassing and interruption of sample-to-electrode contact	Model performance decreases due to overfitting; feature has very low importance value
Addition of reaction atmosphere curve as a feature	Atmosphere might affect reaction rate	Model performance decreases due to overfitting; feature has very low importance value
Addition of pretreatment voltage or highest pretreatment applied as a feature	Pretreatments put sample resistance in an acceptable range for flashing	Model performance decreases due to overfitting; feature has very low importance value (might be accounted for in IT curves)
Addition of mean current in IT curve as a feature	Represents average current density	Model performance decreases due to overfitting; feature has very low importance value
Using V_f/V_0 as a feature	Gives the percent of voltage discharged in the reaction	Model performance decreases due to overfitting; feature has low importance value and correlates with I_F/I_{Max}

Using sample resistance as a feature	Resistance contributes to heating	Model performance decreases due to overfitting; feature has very low importance value. Correlates to I_{Max} and A_{IT}

Table A3.3. Hyperparameters used to train models for a regression model of graphene yield.

Model	**Hyperparameters**	**Range**
Random Forest (RF-R)	Max_depth=6, min_samples_split=3, n_estimators=1000	Max_depth = 3-7, min_samples_split = 2-5, n_estimators = 200, 500, 1000
XGBoost (XGB-R)	max_depth=4, min_child_weight = 2, n_estimators = 45, learning_rate = 0.12, gamma=0.07, subsample=0.725	Max_depth = 3-7, min_child_weight= 2-5, n_estimators = range(45, 65, 5), gamma=np.linspace(0.07, 0.13, 6), learning_rate = np.linspace(0.07, 0.13, 6), subsample=np.linspace(0.7,0.8,5)
Decision Tree Regressor (DT-R)	Max_depth=4, min_samples_split=3	Max_depth = 3-7, min_samples_split = 2-5
Linear Regressor (LR-R)	Default	N/A
Multilayer Perceptron (MLP-R)	Hidden_layer_sizes=(100, 100, 100), activation='relu', learning_rate='adaptive', solver='adam', alpha=0.05	Hidden_layer_sizes: [(100, 100, 100), (10,10,10), (50,50,50), (200, 200, 200)], activation= ['relu','tanh','logistic'], alpha= [0.05, 0.10, 0.12, 0.15], learning_rate = ['constant','adaptive'], solver='adam'
Bayesian Regressor (BR-R)	Default	N/A

References A.3.

1. J. Lin, Z. Peng, Y. Liu, F. Ruiz-Zepeda, R. Ye, E. L. G. Samuel, M. J. Yacaman, B. I. Yakobson, J. M. Tour. *Nat. Comm.,* **2014**, *5***,** 5714.
2. A. P. Kauling, A. T. Seefeldt, D. P. Pisoni, R. C. Pradeep, R. Bentini, R. V. B. Oliveria, K. S. Novoselov, A. H. Castro Neto. *Adv. Mater.,* **2018,** *30,* 1803784.
3. Y. Mizokawa, T. Miyasato, S. Nakamura, K. M. Geib, C. W. Wilmsen. *J. Vac. Sci. Techn. A,* **1987**, *5,* 2809.
4. A. Mezzi, S. Kaciulis. *Surf. Int. Anal.,* **2010,** *42,* 1082-1084.
5. A. J. Barlow, O. Scott, N. Sano, P. J. Cumpson. *Surf. Int. Anal.,* **2015,** *47,* 173.
6. D. X. Luong, K. V. Bets, W. A. Algozeeb, M. G. Stanford, C. Kittrell, W. Chen, R. V. Salvatierra, M. Ren, E. A. McHugh, P. A. Advincula, Z. Wang, M. Bhatt, H. Guo, V. Mancevski, R. Shahsavari, B. I. Yakobson, J. M. Tour, *Nature* **2020**, *577*, 647.

7. E. Lewinson Violin plots explained. (2019) *Towards Data Science.*
8. M. G. Stanford, K. V. Bets, D. X. Luong, P. A. Advincula, W. Chen, J. T. Li, Z. Wang, E. A. McHugh, W. A. Algozeeb, B. I. Yakobson, J. M. Tour, *ACS Nano* **2020**, *14,* 10, 13691.

Improvements on the FJH reactor as the Process is Scaled Up 4.

Spectrometer Temperature Reading of Flash Reactions in Real Time

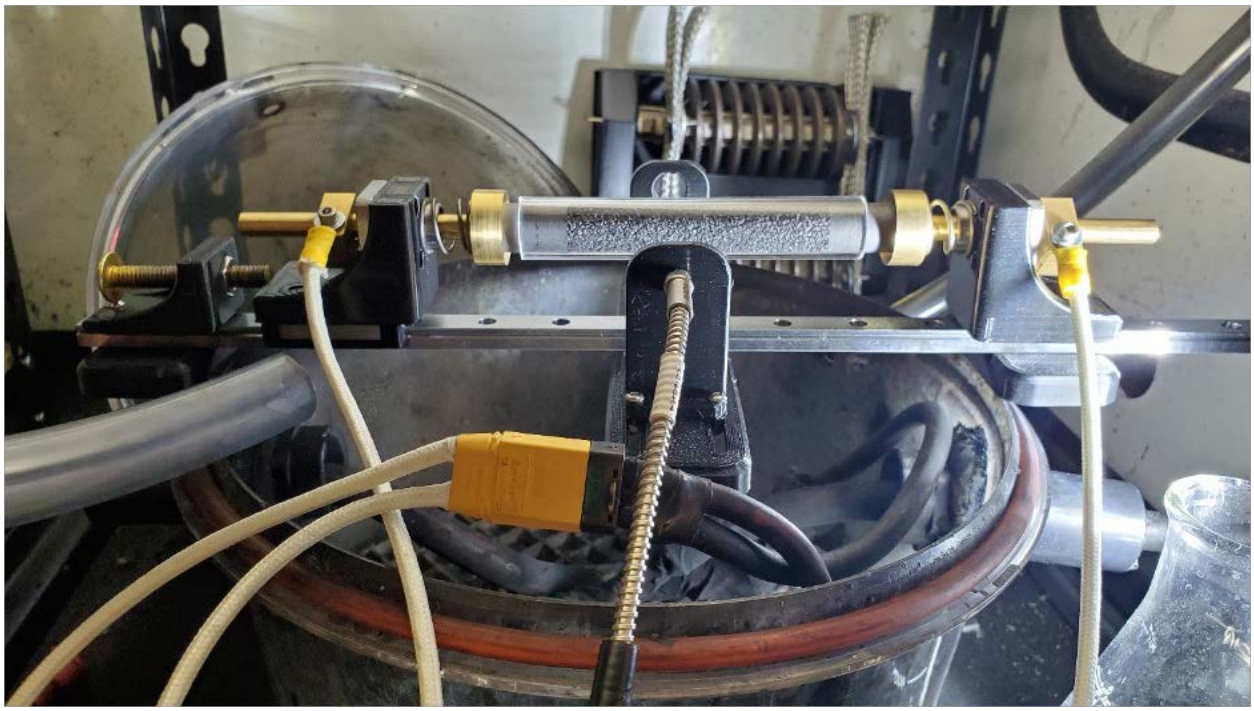

Figure 4.1. New instrument setup for large sample + temperature measurement.

Determined using a new temperature sensing system, the surface temperature of MC flashing is ~ 2100 K. Based on the Raman analysis, MC near the center has better quality than the surface, indicating that the temperature inside is hotter (~3000 K). The feedstock was 10 g of MC that was successfully flashed to produce 9.2 g of product with 100% graphene purity.

New calculations made based on experience indicates that powder FJH reaction automation at using 5.2 g batches at flashing voltage of 350 V will require a 2.5 min cycle, with an average production of 2 g/min or 2.88 kg/day if run for 24 h. The raw material charging time is the limitation since it takes 90% of the flashing cycle.

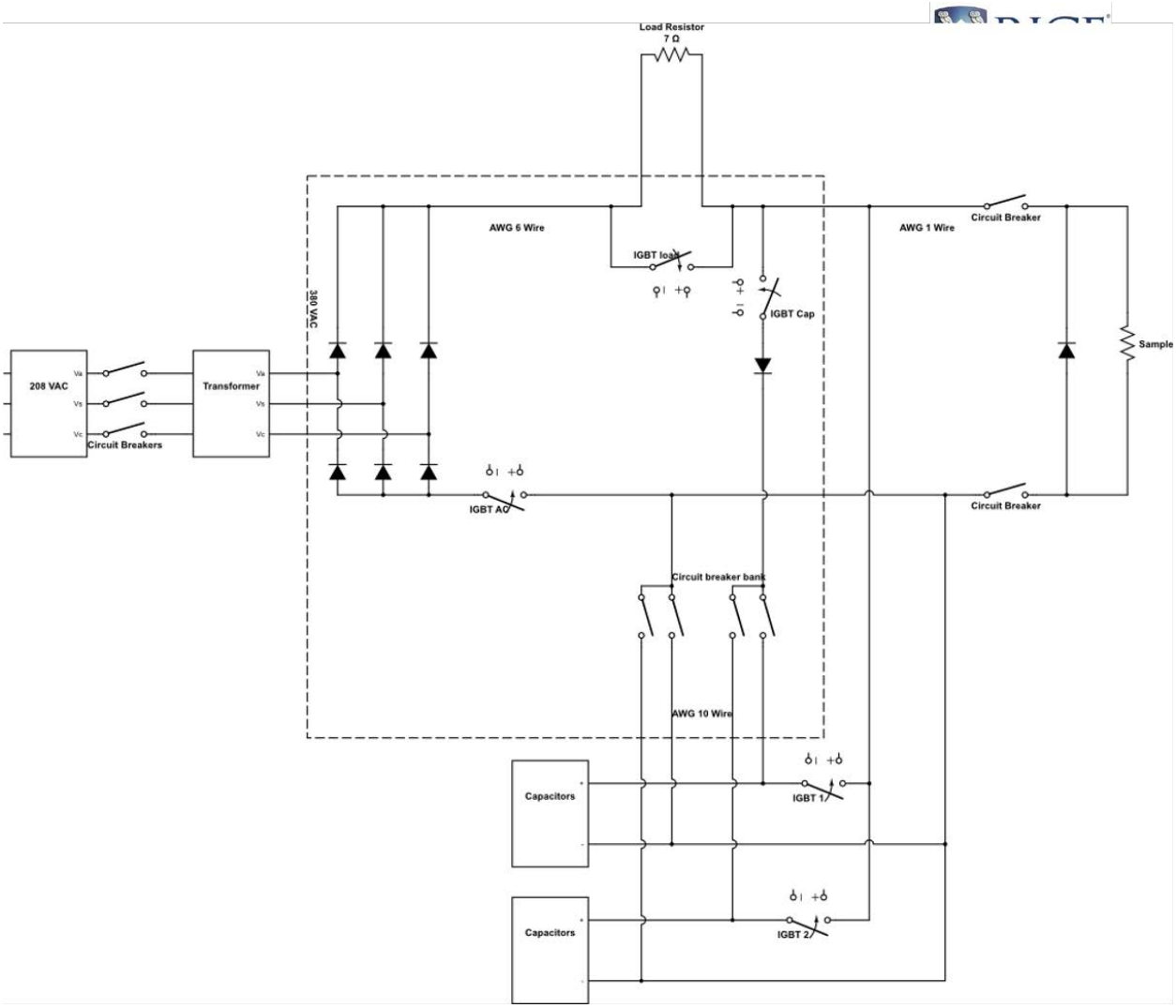

Figure 4.2. A fast-charging system was designed that could charge in 30 s and increase the production rate five times. The circuit diagram is shown above.

Production Throughput During This Project

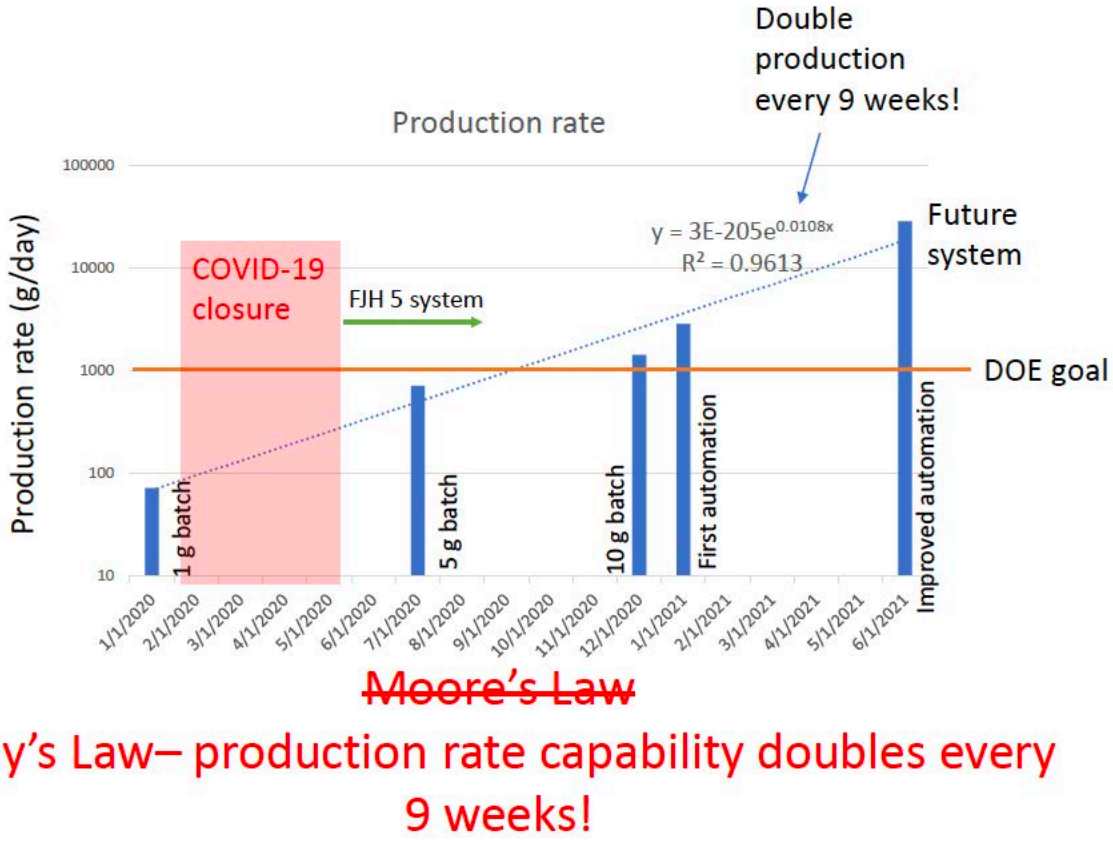

Figure 4.3. Our progress toward increasing production from 1 January 2020 to 1 June 2021, was charted. We have been able to double production every 9 weeks despite the COVID 19 closure of the lab. This was named "Duy's Law" for one of the inventors of the process.

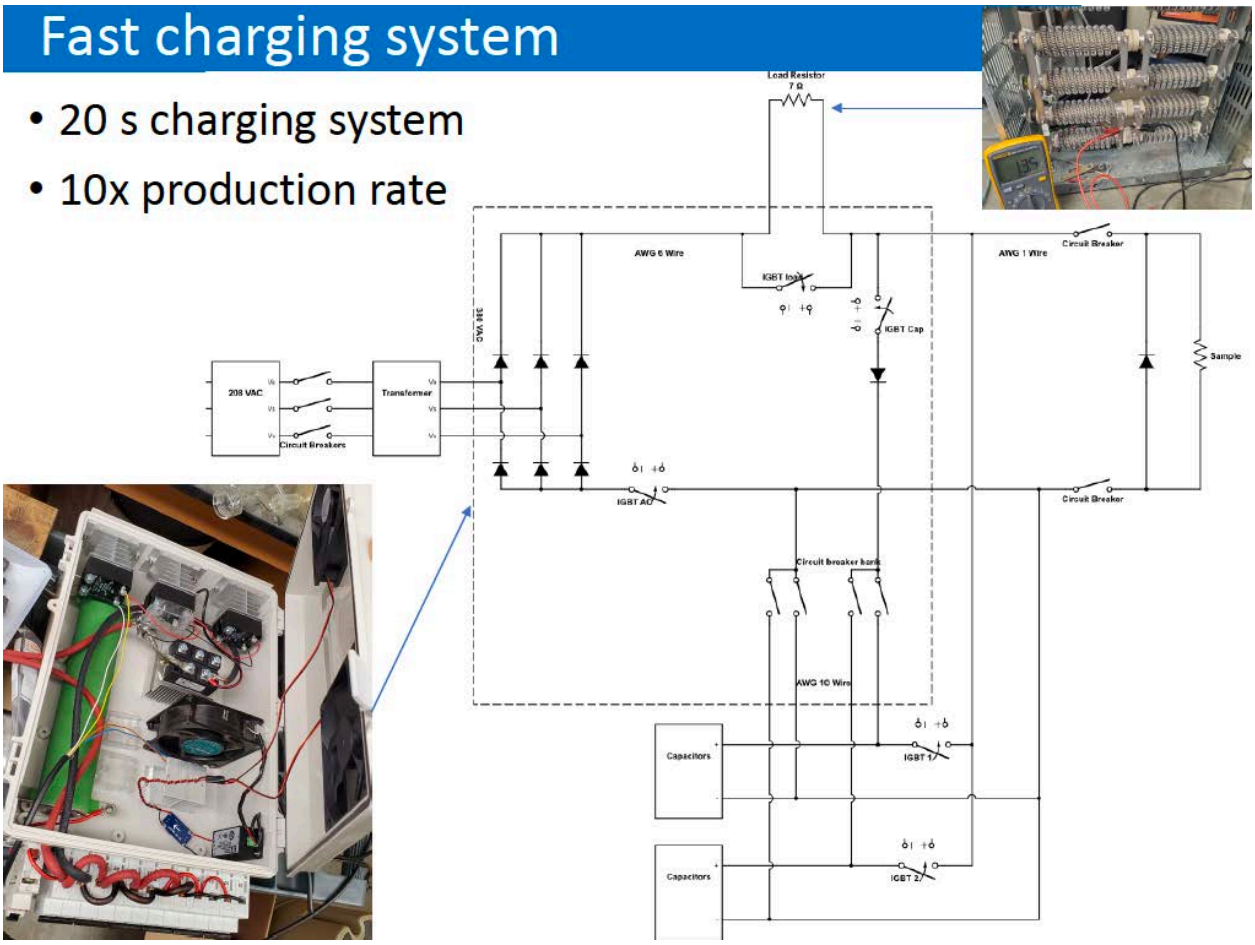

Figure 4.4. A photo and the circuit diagram (same as **Figure 4.2**) for a 19 s charging system, 8X faster than previous version at 70% power capability. Ideally, we can get up to 0.96 kg/h.

Video Analysis of a Flash Reaction

We used a high-speed camera to capture a video of a flash reaction the shows the blinking of the sample at 1000 Hz. The reaction starts at random places around the sample and develops from there. Eventually the flash becomes homogeneous along the sample. The slow-motion video reveals a poor connection between the graphite electrode with the brass support that causes some flashing in the electrode; this will be improved now that we know it is a problem. the outgassing is controllably burned as it proceeds into the air. This shows the advantage of flashing in flowing air that prevents the accumulation of combustible gas in the reaction chamber. We are working to interface this video into a heat map with the help of the spectrometer.

Milestone Preparation: Materials Needed to Prepare 1 kg of FG

Based on our calculations and scale-up research, the production of 1 kg of FG to meet our Milestone will require the following supplies in addition to materials already used to build the equipment:

1. 200 quartz tubes

2. 60 graphite electrodes
3. MC: 1.2 kg ground to 0.6-1.2 mm size.
4. Automation scale.
5. Replaceable magazines and brass electrodes
6. MC weighing station, a bullet gunpowder dispenser only $300 Amazon.
7. Graphite cleaning tumbler, bullet cartridge cleaner only $60 on Amazon.

Figure 4.5: Photos of (left to right) the automation scale, the brass electrodes, the gunpowder dispenser and the bullet cartridge cleaner used for the Milestone effort.

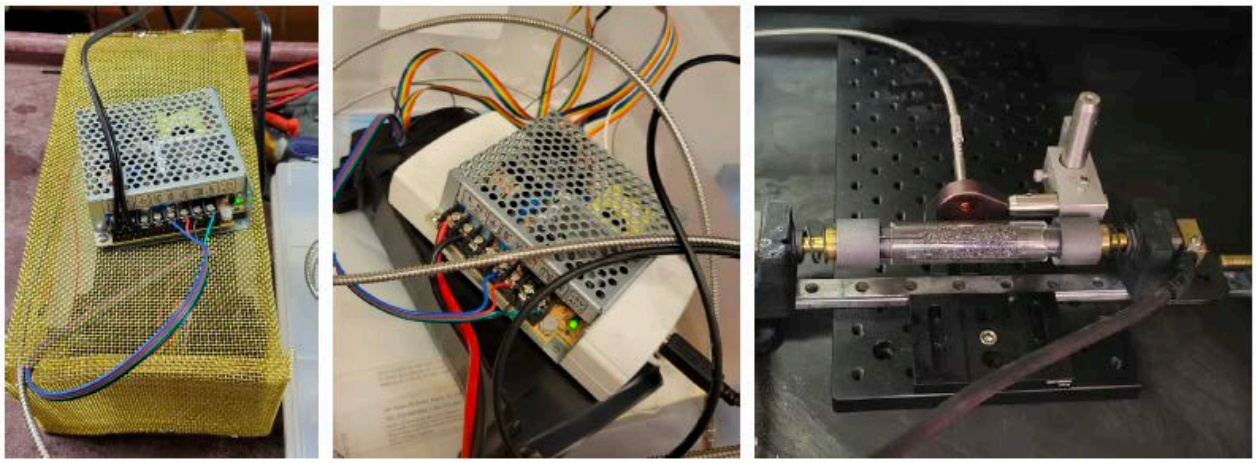

Figure 4.6. New spectrometers to determine temperature of very rapid flash reaction were built**.** We successfully built and deployed two spectrometers (left and middle) for two of our FJH systems. Both spectrometers worked well to collect the temperature profiles. (right) A filter was used to protect the optical fiber end of the spectrometer from the damage an exploding sample might produce.

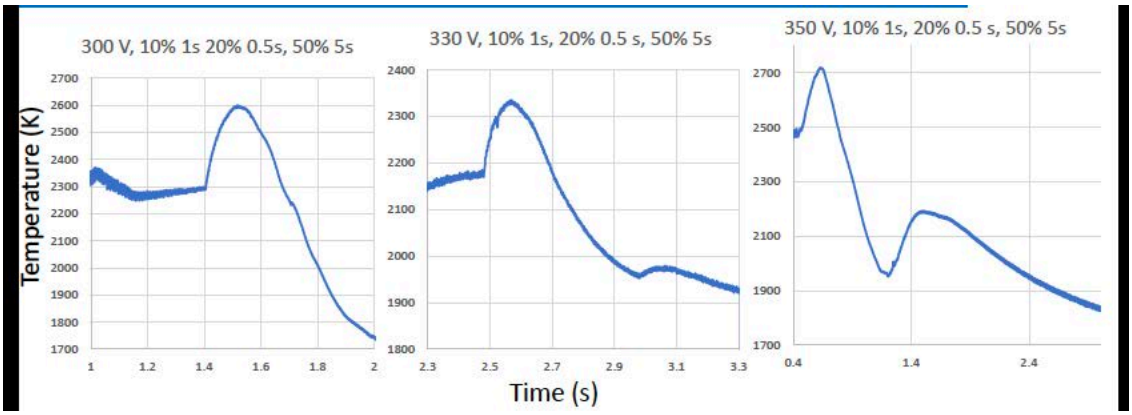

Figure 4.7. Performance of new spectrometer in measuring reaction temperature for 5 g MC at same VFD sequence but different voltages for each sample. All samples reached a similar peak temperature within the first sequence at 10% duty cycle, followed by pulses at 20% and 50% duty cycles.. The duty cycles of 20% and 50% were found to prolong the heat and might not be necessary.

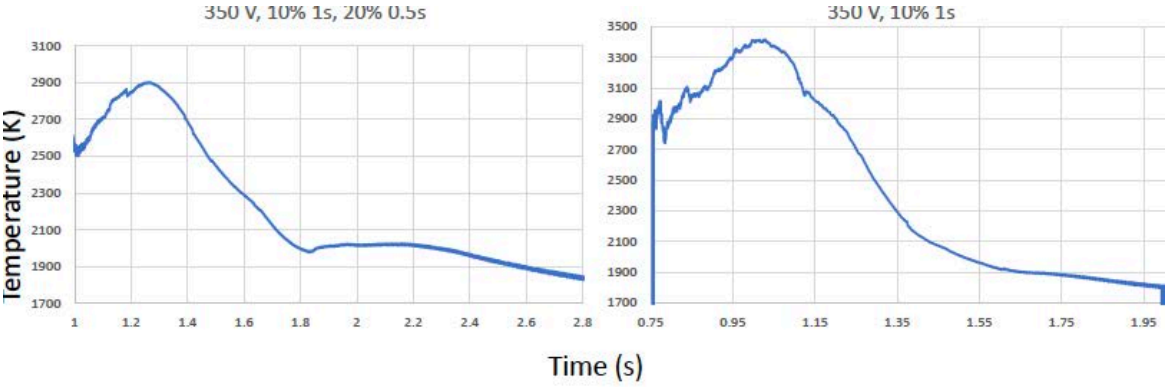

Figure 4.8. Removing the 50% duty cycle pulse (left) and both the 50% and 20% duty cycle pulses (right) result in similar maximum reaction temperatures. However, the graphene quality decreased based on Raman analysis. But the dispersions show similar or even better properties for this graphene due to more turbostratic structure. Energy requirement was reduced from 7.5 to 5.2 kJ/g. Charging time might decrease 30% as well.

Temperature Feedback System

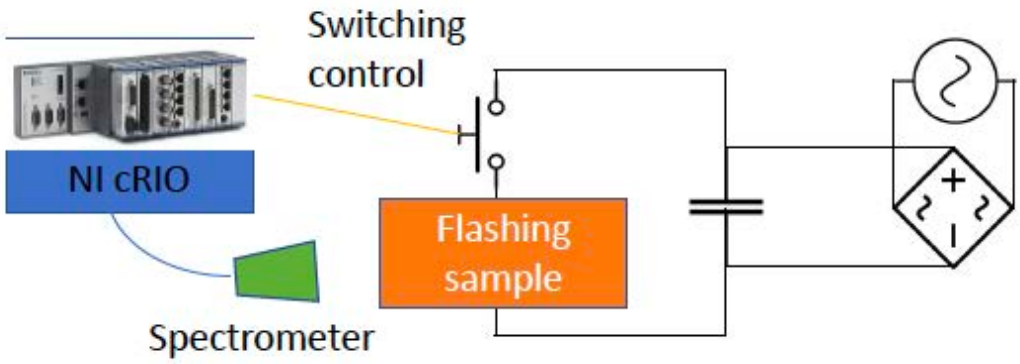

Figure 4.9. A feedback loop to control the FJH reaction temperature using a proportional integral derivative (PID) program was designed, as shown in this diagram. The system can use a spectrometer or IR thermometer to provide the temperature value for the feedback loop.

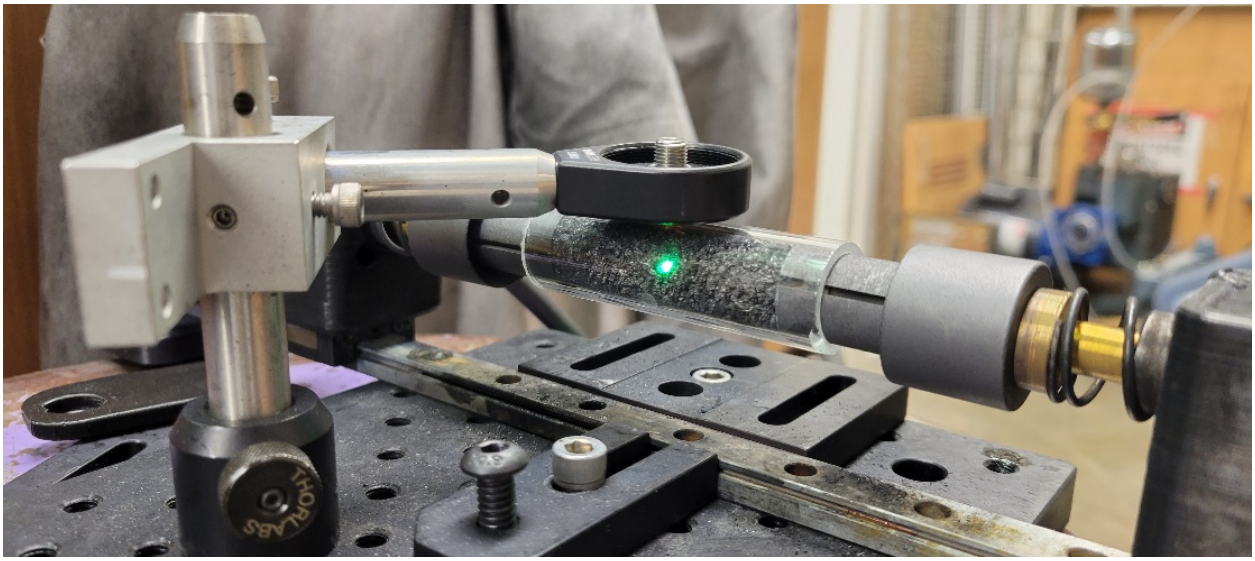

Figure 4.10. This photo shows the temperature control system at the reactor before a FJH reaction. We found that the temperature can be measured by both a commercial IR pyrometer and a customized built spectrometer. The experimental results show both methods match well in temperature measurements. A IR pyrometer is used for temperature feedback

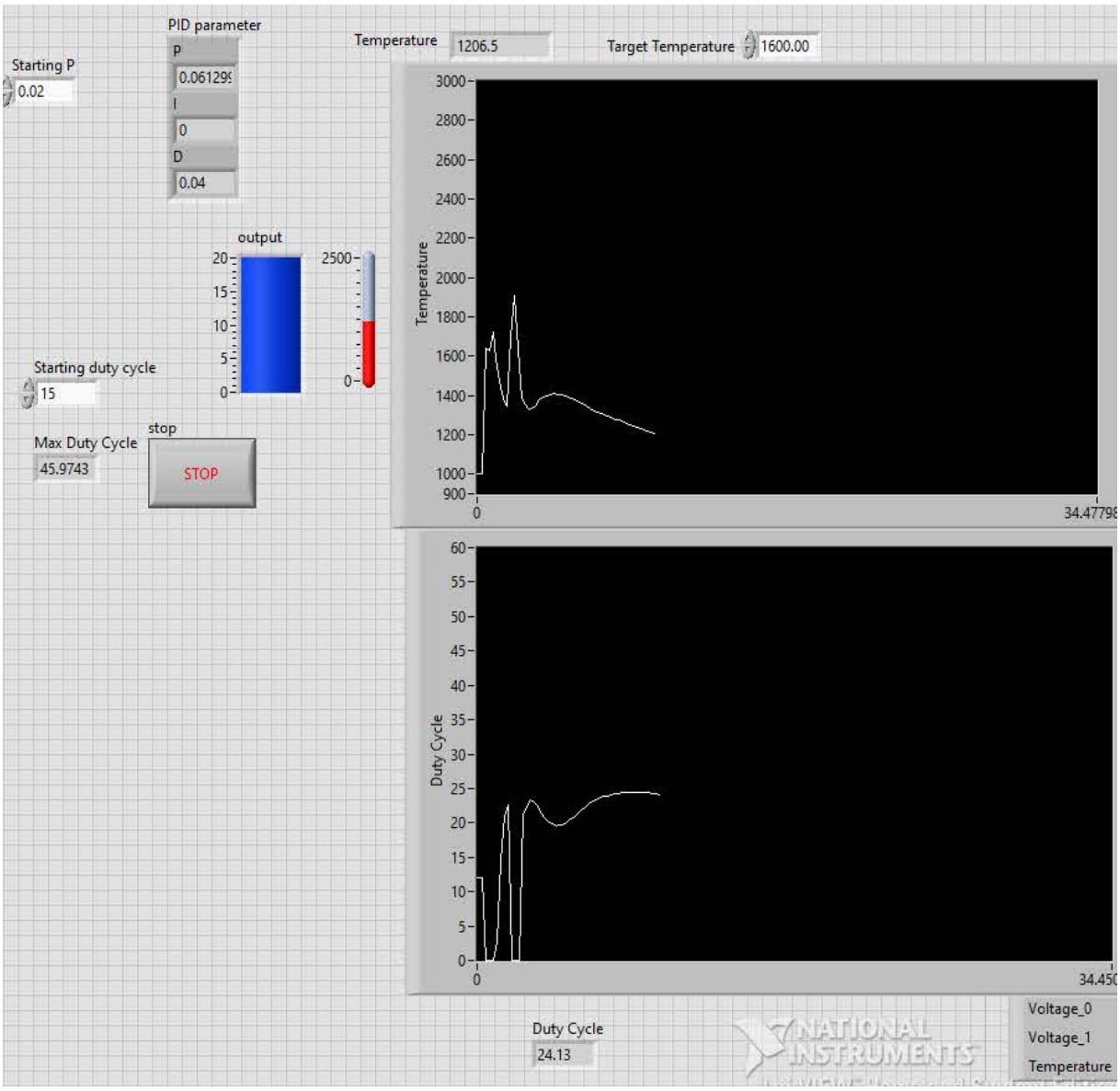

Figure 4.11. A screenshot of the *LabView* based PID controller system user interface. This features automatic control of the duty cycle to regulate the progress of the reaction through temperature feedback. While this screenshot shows specific input values, the PID parameters will change with various components and conditions so that the FJH reaction is optimized.

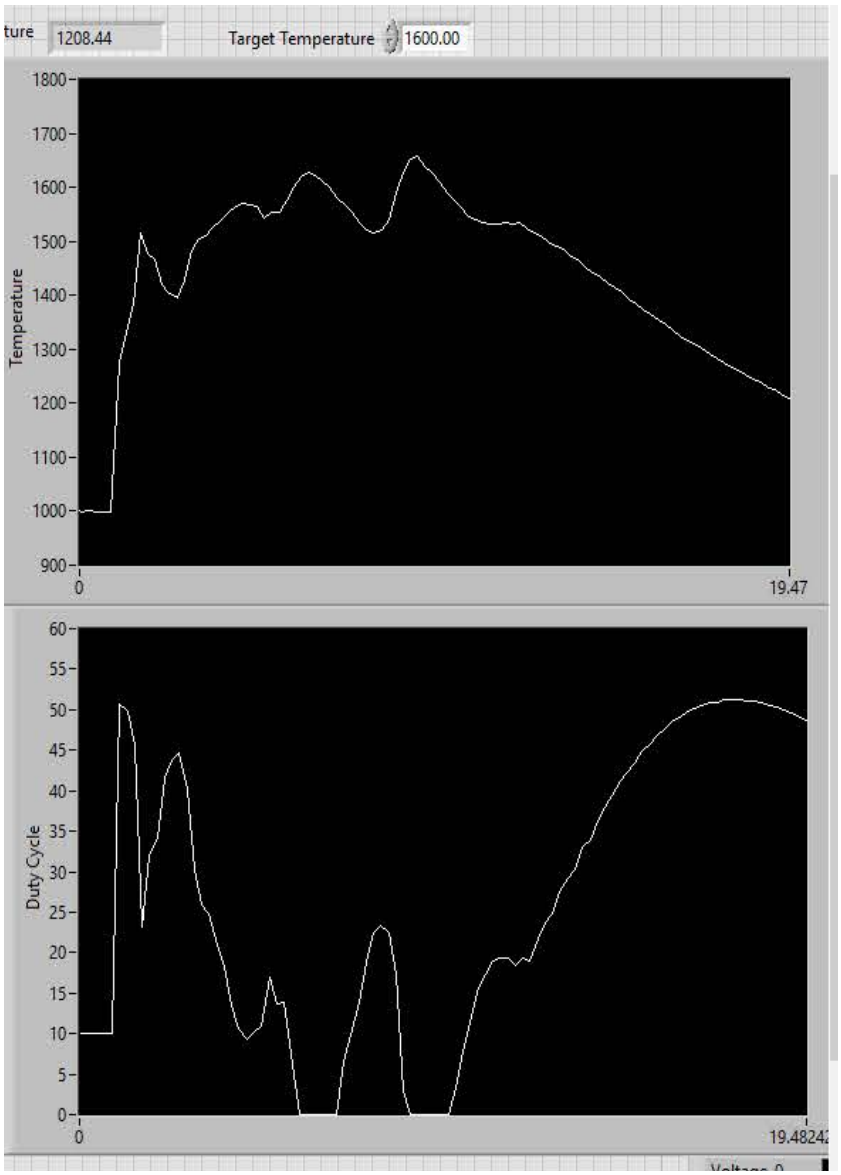

Figure 4.12. The PID temperature feedback design was successfully tested with 5.7 g of MC as shown in this screenshot of the sample temperature and the duty cycle. The program regulates the duty cycle to maintain a target temperature. The current profile shows that the peak current is <1000 A, which is good for the IGBT switching operation. A IGBT is "an insulated-gate bipolar transistor is a three-terminal power semiconductor device primarily used as an electronic switch, which, as it was developed, came to combine high efficiency and fast switching." *Wikipedia*

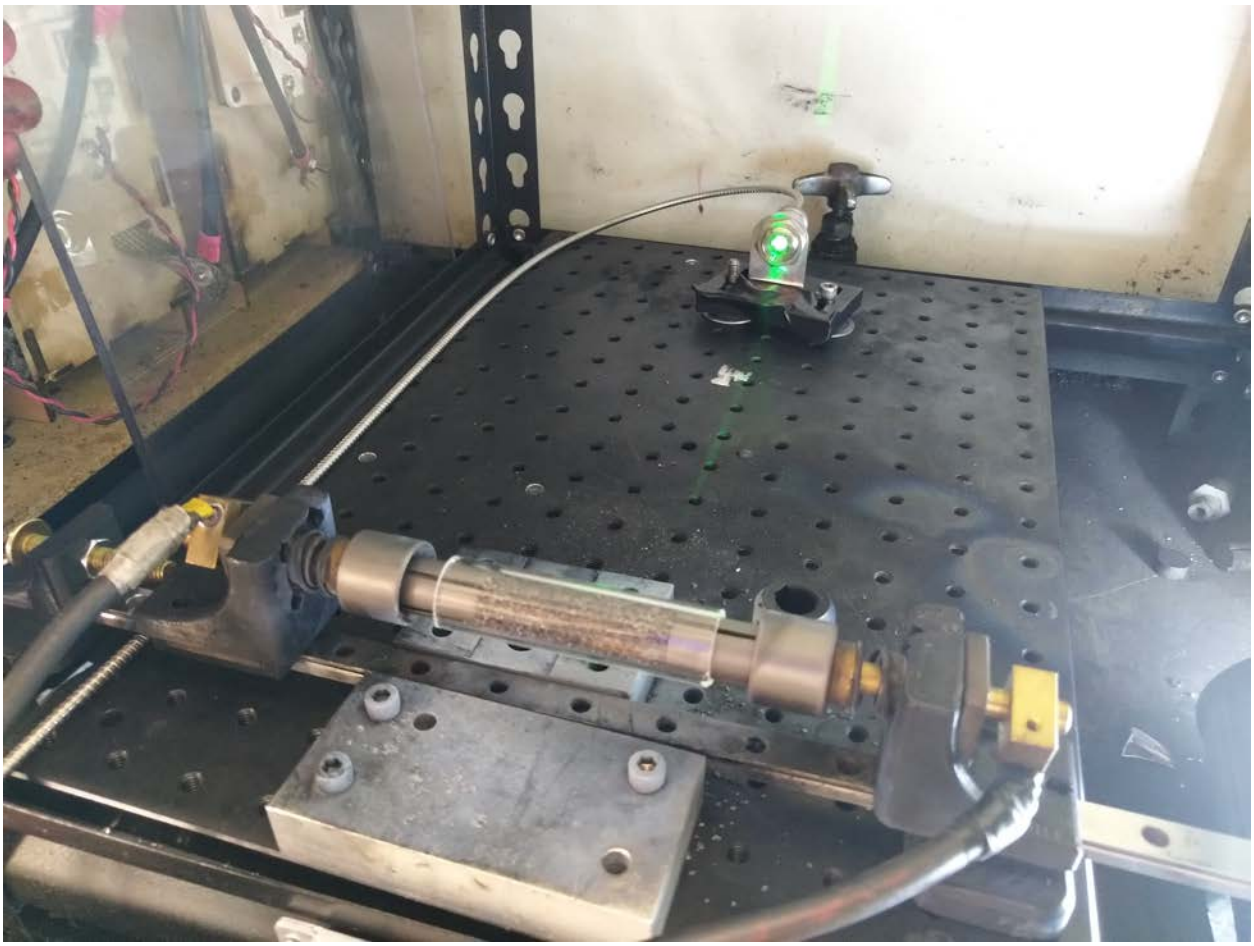

Figure 4.13. A photo of the temperature control system from another viewpoint. The laser thermometer is shown with the aiming laser turned on. It is aiming at a reaction vessel containing 5.7 g MC. The temperature control system set up and working, and the graphene quality *via* PID control competes with that from VFD flashing.

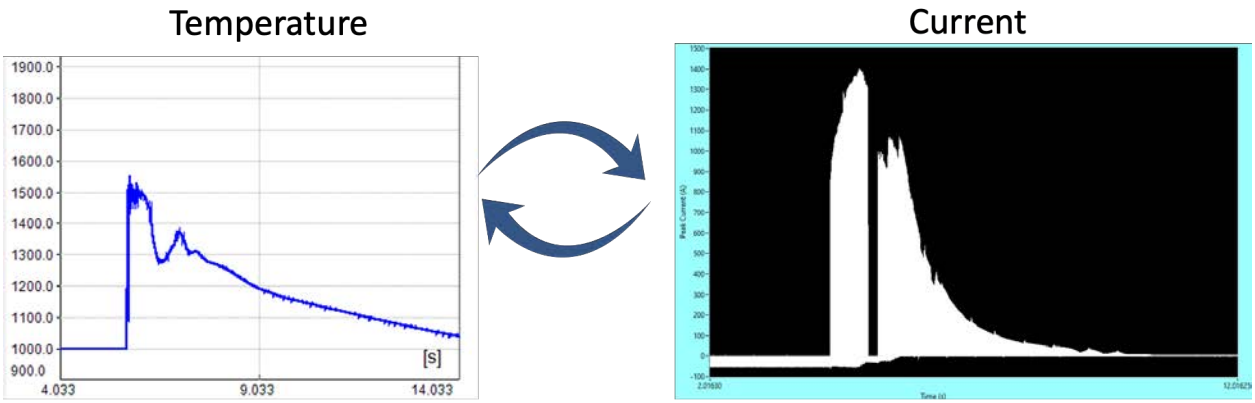

Figure 4.14. The temperature control system has allowed us to study the relationships between the temperature, current profiles and graphene quality. The PID works *via* a feedback loop: the laser thermometer measures temperature, and the PID adjusts current until the temperature reaches the target. The cycle is repeated until the FJH is completed.

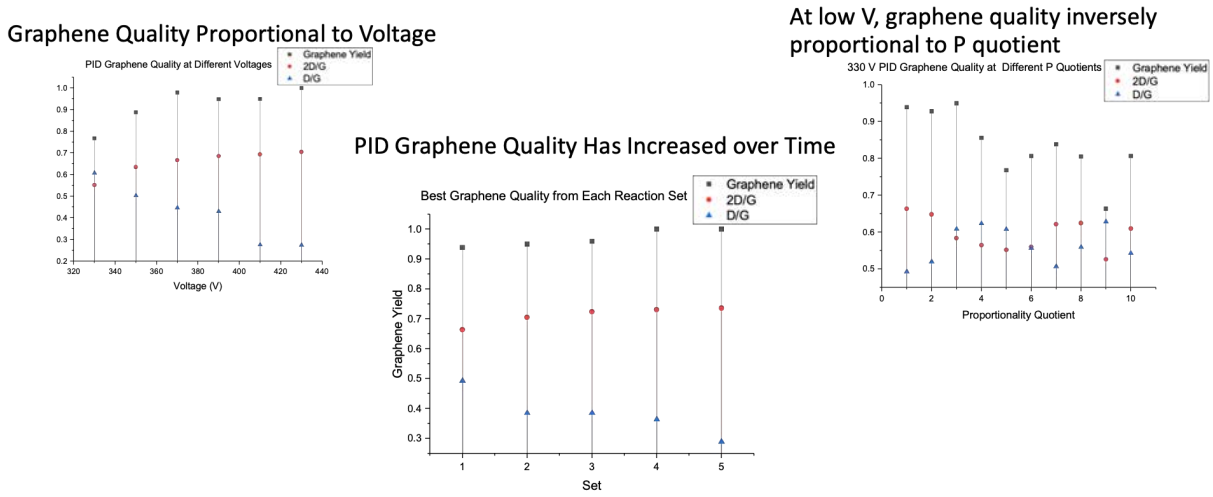

Figure 4.15. A few graphene quality trends are illustrated here as examples that have been guiding our exploration of the parameter space. Graphene quality monitored by 2D/G ratio, D/G ratio, graphene yield, and flashing consistency.

Kilogram-Scale Graphene Production in the Tour Lab 5.

Summary.

The FJH method converts many carbon feedstocks into graphene in seconds using an electrical pulse. This opens an opportunity for processing of low or negative value resources, such as coal and plastic waste, into high value graphene. Here, we demonstrate a lab-scale automation FJH system that allows the synthesis of 1.1 kg of turbostratic flash graphene from coal-based MC in 1.5 h. The automation was based on the conversion of 5.7 g of MC per batch using an electrical pulse width modulation system to conduct the bottom-up upcycle of MC to graphene.

Introduction

The high-yield bottom-up production of graphene has typically been limited to milligram scales. The FJH method provides a remedy to this through its capability to convert virtually any carbon source into tFG *via* a reaction completed in seconds.[1-5] The versatility of FJH has also lent itself to the conversion extraction of metals from industrial waste[6-7] as well the ultrafast synthesis of various carbon compounds.[8-9] The conversion and morphology of the synthesis product depends on the heating profile as determined by the electrical discharge rate.[10] In tFG synthesis, this heating profile has a significant effect on the turbostraticity.[11] Thus, the tFG quality is controlled by the rate of discharge of the capacitors making up the FJH system. Furthermore, constraints on the rate at which FJH can be performed are imposed by both the charging rate of the capacitor banks in the FJH reactor as well as the need for the FJH product to be cooled prior to being removed and replaced with another by the automated system.

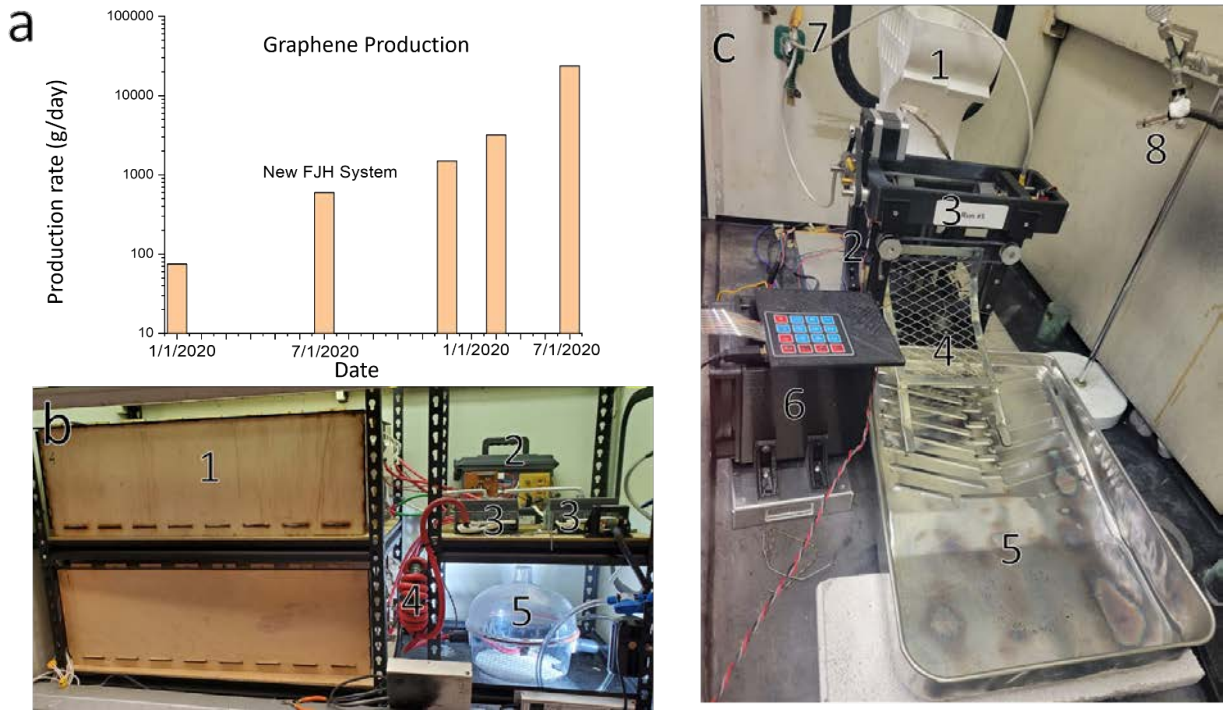

Figure 5.1. a. Production rate from the first publication that disclosed the carbon materials conversion using the FJH process. b. The scale-up flashing system that has total capacitance of 0.624 F with 500 VDC rating and is capable of flashing 10 g of MC per batch. b1. six capacitor banks, each consisting of eight 13 mF capacitors in parallel. b2: Switching controller that controls the simultaneous discharge of the capacitor banks. b3: Kill switches to toggle the flashing system. b4: Inductor with 1 mH inductance that slightly slows the discharge rate by raising the time constant. b5: Flashing chamber to contain sample outgassing. c. The automated system can flash 5.7 g of MC per batch and reloading the new sample with ~20 s cycling. c1: The magazine that holds the reaction vessels prior to flashing. c2: The stand for the flashing chamber. c3: The jig that loads, flashes, and unloads reaction vessels. c4: The ramp onto which the reacted vessels drop upon being unloaded. c5: The basin used to collect flashed samples. c6: The controller for the loading and unloading sytems. c7: The connection to the 0.624 F capacitor banks. c8: An air hose for cooling the reaction vessel to minimize the melting of the flashing stand.

Results and Discussion 5.

From the discovery of the FJH process, the tFG production rate has doubled each 9 weeks on average (**Figure 4.3**). The exponential growth in production rate is because of two factors: building a reactor for the higher capacity flashing system that is capable of flashing 10 g MC in each batch and the automated sample reloading system (**Figure 5.1**). The FJH system is powered by 48 capacitors at a total of 0.624 F capacitance. Each set of 8 capacitors are put into a capacitor bank and controlled by a solid-state relay. Six capacitor banks are connected to the kill switch upstream from the connection to the sample jig. To slow the current for more stable electrical control, a 1 mH inductor is put in series with the circuit. The sample can be flashed either a controlled environment flashing chamber or in ambient atmosphere. The automated system is controlled by

a customized *LabView* program. Once the sample is loaded inside the flashing jig, the FJH system will commence the flash. After the flash is done, the sample is dropped into a collection tray and the new sample is loaded into the flashing jig.

Flashing with Pulse Width Modulation

Pulse width modulation (PWM) is utilized to cut the continuous discharge of the capacitor banks into sections via the rapid (1 kHz) on-and-off switching enabled by IGBTs mounted on each capacitor bank. The customized *LabView* program controls the frequency of IGBT switching, the fraction of time the switch is turned on (duty cycle), as well as the duration of each duty cycle. Thus, to compensate for the exponential decrease in power during the discharge of a capacitor, higher duty cycles are selected as the reaction proceeds to maintain more constant electrical power over the duration of the discharge, as seen in **Figure 5.2a**.

With only a DC flash and a full-time open circuit, the single current spike results in measured surface temperatures significantly higher than for an equivalent flash using PWM. This rapid temperature increase thus models more closely an adiabatic process and increases the risk of violent outgassing that results in the explosion of the reaction vessel. As a result, pretreatment of the sample is needed prior to a pure DC flash to mitigate the chance of reaction explosion. As seen in **Figure 5.2a**, the flash is commenced after a few pretreatments and has a peak current of over 1500 A. With a PWM flash, the pretreatment is not necessary, and the peak current is less than 1000 A, reducing the flashing time and the risk of explosion and equipment failure, while increasing the energy efficiency and production throughput. Furthermore, as seen in **Figure 5.3**, PWM flashes exhibit superior solubility compared to DC flashes, reflecting an improvement in tFG quality. The brevity of the temperature spike in the pure DC flash leads to reduced uniformity in the FG product relative to that of a PWM flash.

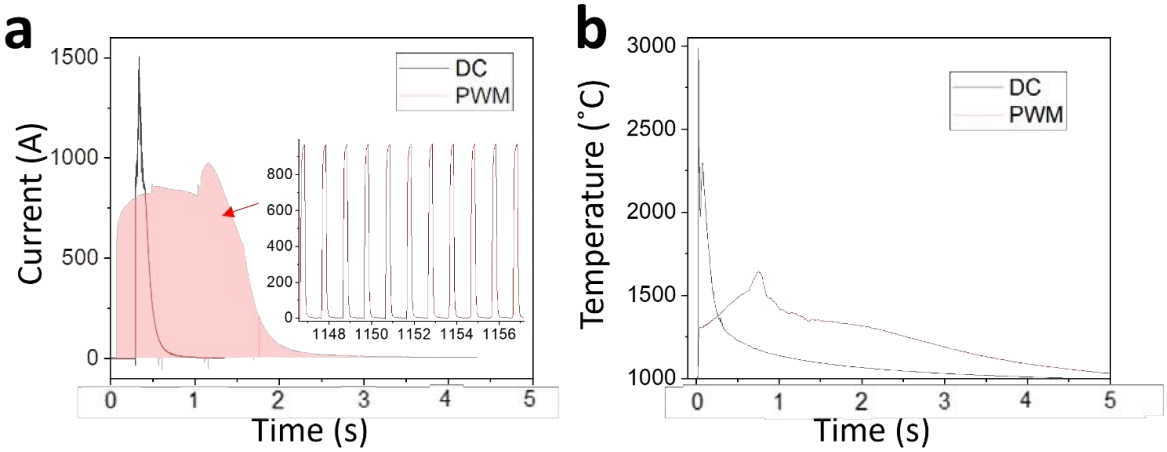

Figure 5.2. a. Current profile of DC flash vs PWM flash. The pulse sequence of the PWM flash is shown in the inset as a single pulse being divided into duty cycles to reduce the average power used. b. Temperature profile of the same DC and PWM flash.

The temperature profile (**Figure 5.2**) shows that the DC flash has a temperature of 3000 °C peak and <500 ms duration, matching well with the result from our previous publication. The PWM flash peaks at 1600 °C but has duration of only ~2 s. However, when comparing the graphene

quality by Raman, the two are similar spectroscopically. The result indicates that the lower temperature can be compensated for by longer flashing time. Even though the DC flash seems to have shorter duration, the production throughput using DC is much lower than PWM flash because of the addition of pretreatment flashes.

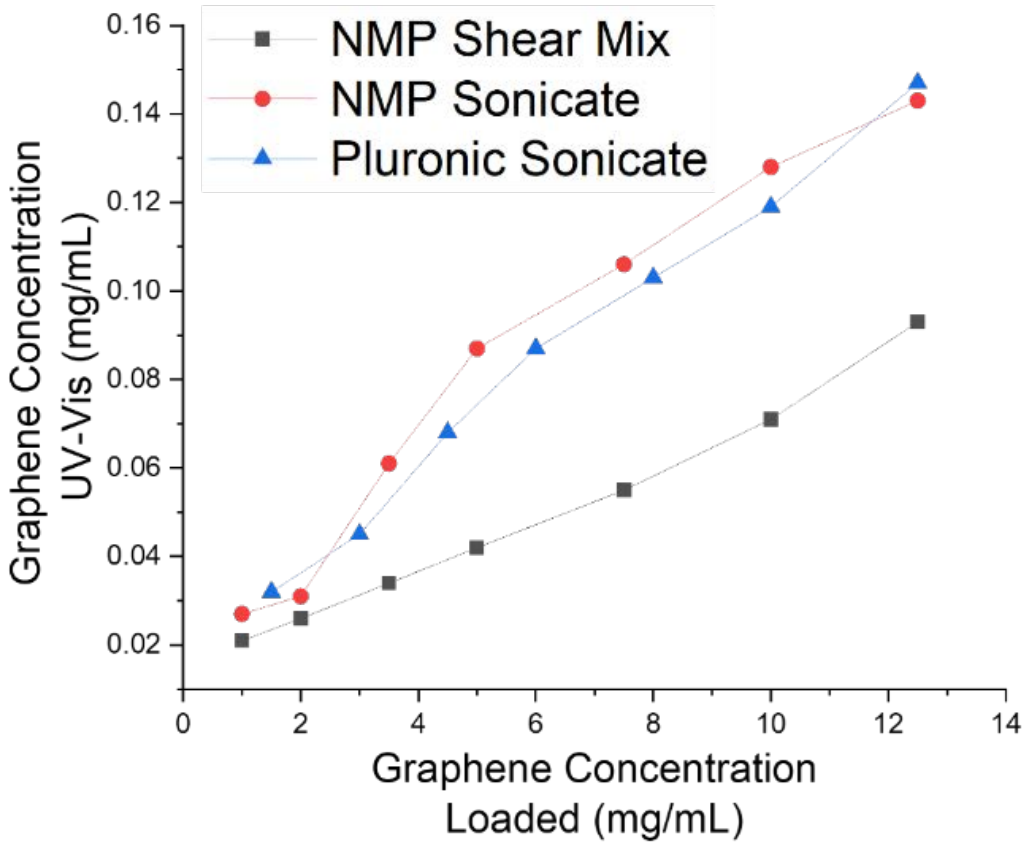

Figure 5.3. UV-Vis dispersion map of tFG concentration from a 5.7 g MC feedstock at 330 V using PWM flash conditions. We achieve a dispersion of 0.16 mg/mL tFG from MC feedstock. This is lower than the dispersion of tFG produced from flashing of carbon black, but this is attributed to the large sheet size of MC rather than tFG quality.

The ability to perform flashing with a tunable and more uniform heating profile enables consecutive flashes to be performed without concern of significant variance in product quality between flashes. This paved the way for the addition of an automated extension to the flash graphene system, as shown in **Figure 5.1c**. This system automatically loads reaction vessel, charges the capacitor banks, flashes the material in the reaction vessel, and unloads the reaction vessel before repeating. With the automated system, batches were run at different flashing voltages yielding over 200 samples in total, amounting to 1.1 kg of tFG. Raman spectroscopy shows a positive correlation between the tFG yield and the energy input into the samples, as shown in **Figure 5.4**, allowing a yield of > 90% for the highest voltage batch, which indicates good carbon

feedstock conversion. The current rate of flashing permits over 10 kg of tFG to be produced per day.

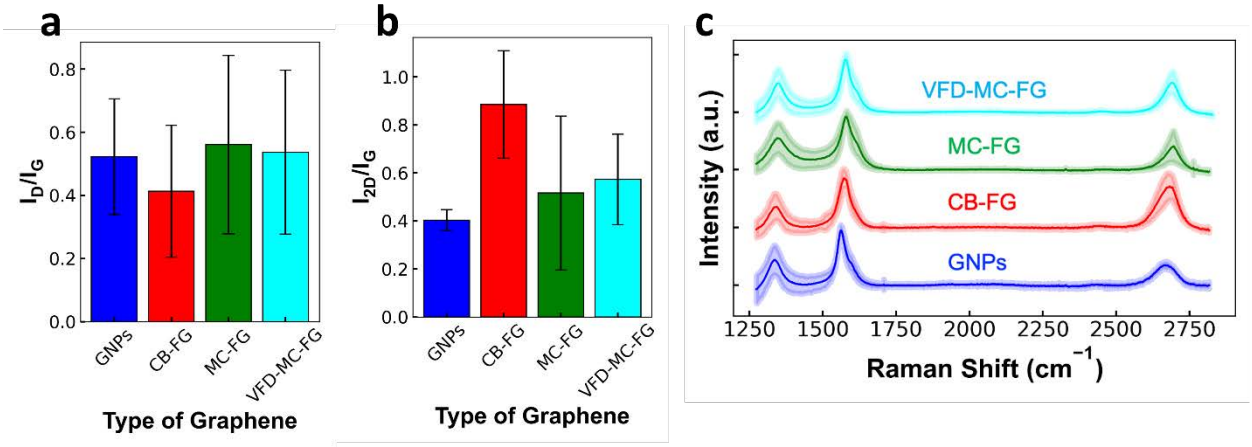

Figure 5.4. a. Comparison of the ratio of the intensities of the D and G Raman bands for turbostratic flash graphene from different graphene products, including graphene nanoparticles (GNPs), carbon black flash graphene (CB-FG), metallurgical coke flash graphene (MC-FG) and variable frequency driver produced metallurgical coke flash graphene (VFD-MC-FG). b. Comparison of the ratio of the intensities of the 2D and G Raman bands. The ratio of the amplitude of the D Raman peak to the G Raman peak is inversely proportional to the graphene sheet size. b. Comparison of the ratio of the intensities of the 2D and G Raman bands for different carbon feedstocks. This ratio is proportional to the conversion yield of carbon feedstock to tFG. c. Comparison of Raman maps of each of the feedstocks. Error bars are expressed as shaded areas around the main lines

Conclusion on Scale-Up of FJH Process

In summary, the implementation of PWM *via* a VFD enables enhanced control of the electric discharge of the FJH system's capacitor banks. This enables control over the heating profile during graphene synthesis, enabling flashes to be optimized around individual feedstocks. The increase in consistency that PWM provides allows consecutive flashes to be performed by the automation system without significant variance in graphene quality. This provides a solution to previous limitations on graphene applications arising from low scalability. We met the end Milestone of the project, to make 1 kg of FG in 1 day.

Methods

Materials: Metallurgical coke was ground and sieved until particle diameter was between 0.8- and 2-mm. CB (APS 10 nm, Black Pearls 2000) was purchased from Cabot Corporation.

FJH System: The circuit diagram of the FJH system is earlier in this report. The automated system used the same discharge source as that presented in previous reports and literature. The capacitors were charged to 370 V prior to each flash, which translates to 15 kJ of energy per g of MC reacted. The 1.1 kg tFG produced *via* automation was performed under multiple cycles that produced roughly 0.25 kg of tFG per cycle. PWM was implemented using a custom written *LabView*

program with a frequency of 1000 Hz. The duty cycle of the PWM was programmed to be 10% for 1 s, 20% for 0.5 s, and 50% for 5 s before dropping to 0%.

References 5.

1. Luong, D. X.; Bets, K. V.; Algozeeb, W. A.; Stanford, M. G.; Kittrell, C.; Chen, W.; Salvatierra, R. V.; Ren, M.; McHugh, E. A.; Advincula, P. A.; Wang, Z.; Bhatt, M.; Guo, H.; Mancevski, V.; Shahsavari, R.; Yakobson, B. I.; Tour, J. M., Gram-Scale Bottom-Up Flash Graphene Synthesis. *Nature* **2020,** *577*, 647-651.
2. Wyss, K. M.; Beckham, J. L.; Chen, W.; Luong, D. X.; Hundi, P.; Raghuraman, S.; Shahsavari, R.; Tour, J. M., Converting plastic waste pyrolysis ash into flash graphene. *Carbon* **2021,** *174*, 430-438.
3. Advincula, P. A.; Luong, D. X.; Chen, W.; Raghuraman, S.; Shahsavari, R.; Tour, J. M., Flash graphene from rubber waste. *Carbon* **2021,** *178*, 649-656.
4. Wyss, K. M.; Wang, Z.; Alemany, L. B.; Kittrell, C.; Tour, J. M., Bulk Production of Any Ratio ^{12}C:^{13}C Turbostratic Flash Graphene and Its Unusual Spectroscopic Characteristics. *ACS Nano* **2021,** *15* (6), 10542-10552.
5. Algozeeb, W. A.; Savas, P. E.; Luong, D. X.; Chen, W.; Kittrell, C.; Bhat, M.; Shahsavari, R.; Tour, J. M., Flash Graphene from Plastic Waste. *ACS Nano* **2020,** *14* (11), 15595-15604.
6. Deng, B.; Wang, X.; Luong Duy, X.; Carter Robert, A.; Wang, Z.; Tomson Mason, B.; Tour James, M., Rare earth elements from waste. *Sci. Adv. 8* (6), eabm3132.
7. Deng, B.; Luong, D. X.; Wang, Z.; Kittrell, C.; McHugh, E. A.; Tour, J. M., Urban mining by flash Joule heating. *Nat. Commun.* **2021,** *12*, 5794.
8. Deng, B.; Wang, Z.; Chen, W.; Li, J. T.; Luong, D. X.; Carter, R. A.; Gao, G.; Yakobson, B. I.; Zhao, Y.; Tour, J. M., Phase controlled synthesis of transition metal carbide nanocrystals by ultrafast flash Joule heating. *Nat. Commun.* **2022,** *13*, 262.
9. Chen, W.; Li, J. T.; Wang, Z.; Algozeeb, W. A.; Luong, D. X.; Kittrell, C.; McHugh, E. A.; Advincula, P. A.; Wyss, K. M.; Beckham, J. L.; Stanford, M. G.; Jiang, B.; Tour, J. M., Ultrafast and Controllable Phase Evolution by Flash Joule Heating. *ACS Nano* **2021,** *15*, 11158-11167.
10. Chen, W.; Wang, Z.; Bets, K. V.; Luong, D. X.; Ren, M.; Stanford, M. G.; McHugh, E. A.; Algozeeb, W. A.; Guo, H.; Gao, G.; Deng, B.; Chen, J.; Li, J. T.; Carsten, W. T.; Yakobson, B. I.; Tour, J. M., Millisecond Conversion of Metastable 2D Materials by Flash Joule Heating. *ACS Nano* **2021,** *15*, 1282-1290.
11. Stanford, M. G.; Bets, K. V.; Luong, D. X.; Advincula, P. A.; Chen, W.; Li, J. T.; Wang, Z.; McHugh, E. A.; Algozeeb, W. A.; Yakobson, B. I.; Tour, J. M., Flash Graphene Morphologies. *ACS Nano* **2020,** *14*, 13691-13699.

Participants & Other Collaborating Organizations:

Argonne National Laboratory – testing of flash graphene in lubrication applications by Dr. Anirudha Sumant continues.

Peer-reviewed Published Papers citing full or partial NETL/DOE funding

1. Algozeeb, W. A.; Savas, P. E.; Luong, D. X.; Chen, W.; Kittrell, C.; Bhat, M.; Shahsavari, R.; Tour, J. M. Flash Graphene from Plastic Waste. *ACS Nano* **2020** *14*, 15595-15604. DOI: 10.1021/acsnano.0c06328
2. Stanford, M. G.; Bets, K. V.; Luong, D. X.; Advincula, P. A.; Chen, W.; Li, J. T.; Wang, Z.; McHugh, E. A.; Algozeeb, W. A.; Yakobson, B. I.; Tour, J. M. Flash Graphene Morphologies. *ACS Nano* **2020**, *14*, 13691-13699. DOI: 10.1021/acsnano.0c05900
3. Deng, B.; Luong, D. X.; Wang, Z.; Kittrell, C.; McHugh, E. A.; Tour, J. M. Urban Mining by Flash Joule Heating. *Nature Commun.* **2021**, *12*, 5794. DOI: 10.1038/s41467-021-26038-9
4. Advincula, P. A.; Luong, D. X.; Chen, W.; Raghuraman, S.; Shahsavari, R.; Tour, J. M. Flash Graphene from Rubber Waste. *Carbon* **2021**, *178*, 649-656. DOI: 10.1016/j.carbon.2021.03.020.
5. Chen, W.; Wang, Z.; Bets, K. V.; Luong, D. X.; Ren, M.; Stanford, M. G.; McHugh, E. A.; Algozeeb, W. A.; Guo, H.; Gao, G.; Deng, B.; Chen, J.; Li, J. T.; Carsten, W. T.; Yakobson, B. I.; Tour, J. M. Millisecond Conversion of Metastable 2D Materials by Flash Joule Heating. *ACS Nano* **2021**, *15*, 1282-1290. DOI: 10.1021/acsnano.0c08460
6. Wyss, K. A.; Beckham, J. L.; Chen, W.; Luong, D. X.; Hundi, P.; Raghuraman, S.; Shahsavari, R.; Tour, J. M. Converting Plastic Waste Pyrolysis Ash into Flash Graphene. *Carbon* **2021**, *174*, 430-438. DOI: 10.1016/j.carbon.2020.12.063
7. Chen, W.; Li, J. T.; Wang, Z.; Algozeeb, W. A.; Luong, D. X.; Kittrell, C.; McHugh, E. A.; Advincula, P. A.; Wyss, K. M.; Beckham, J. L.; Stanford, M. G.; Jiang, B.; Tour, J. M. Ultrafast and Controllable Phase Evolution by Flash Joule Heating. *ACS Nano* **2021**, *15*, 11158–11167. DOI: 10.1021/acsnano.1c03536
8. Barbhuiya, N. H.; Kumar, A.; Singh, A.; Chandel, M. K.; Arnusch, C. J.; Tour, J. M.; Singh, S. P. The Future of Flash Graphene for the Sustainable Management of Solid Waste. *ACS Nano* **2021**, *15*, 15461-15470. DOI: 10.1021/acsnano.1c07571
9. Wyss, K. M.; Wang, Z.; Alemany, L. B.; Kittrell, C.; Tour, J. M. Bulk Production of Any Ratio ^{12}C:^{13}C Turbostratic Flash Graphene and its Unusual Spectroscopic Characteristics. *ACS Nano* **2021**, *15*, 10542–10552. DOI: 10.1021/acsnano.1c03197
10. Chen, W.; Ge, C.; Li, J. T.; Beckham, J. L.; Yuan, Z.; Wyss, K. M.; Advincula, P. A.; Eddy, L.; Kittrell, C.; Chen, J.; Luong, D. X.; Carter, R. A.; Tour, J. M. Heteroatom-Doped Flash Graphene. *ACS Nano* **2022**, *16*, 6646-6656. DOI: 10.1021/acsnano.2c01136.
11. Beckham, J. L.; Wyss, K. M.; Xie, Y.; McHugh, E. A.; Li, J. T.; Advincula, P. A.; Chen, W.; Jian Lin, J.; Tour, J. M. Machine Learning-Guided Synthesis of Flash Graphene. *Adv. Mater.* **2022**, 2106506, 1-11. DOI: 10.1002/adma.202106506
12. Wyss, K. M.; Luong, D. X.; Tour, J. M. Large-Scale Syntheses of 2D Materials: Flash Joule Heating and Other Methods- A Review. *Adv. Mater*. **2022**, 2106970, 1-27. DOI: 10.1002/adma.202106970
13. Deng, B.; Wang, Z.; Chen, W.; Li, J. T.; Luong, D. X.; Carter, R. A.; Gao, G.; Yakobson, B. I.; Zhao, Z.; Tour, J. M. Phase Controlled Synthesis of Transition Metal Carbide Nanocrystals by Ultrafast Flash Joule Heating. *Nature Commun*. **2022**, *13:262*, 1-10. 10.1038/s41467-021-27878-1
14. Algozeeb, W. A.; Savas, P. E.; Yuan, Z.; Wang, Z.; Kittrell, C.; Hall, J. N.; Chen, W.; Bollini, P.; Tour, J. M. Plastic Waste Product Captures Carbon Dioxide in Nanometer Pores. *ACS Nano* **2022**, *16*, 7284-7290. DOI: 10.1021/acsnano.2c00955.

15. Deng, B.; Wang, X.; Luong, D. X.; Carter, R. A.; Wang, Z.; Tomson, M. B.; Tour, J. M. Rare Earth Elements from Waste. *Sci. Adv.* **2022**, *8*, eabm3132, 1-9. DOI: 10.1126/sciadv.abm3132
16. Wyss, K. M.; De Kleine, R. D.; Couvreur, R. L.; Kiziltas, A.; Mielewski, D. F.; Tour; J. M. Upcycling End-of-Life Vehicle Waste Plastic Into Flash Graphene. *Comm. Engineering* **2022**, *1*, 3, (1-12). DOI: 10.1038/s44172-022-00006-7

Patent applications owned by Rice University

Track Code	Type	Status	Country	Application Number	Application Date	Title	Inventors
2021-031-PZ	Provisional	Active	United States	63/147,069	2/8/21	Recycling of Spent Batteries by Flash Joule Heating	James M. Tour, Weiyin Chen, Wilbur Carter Kittrell and Duy X. Luong
2019-015-HK	Country Specific EPO Patent	Filed	Hong Kong	62021035222	7/19/21	Sub-second graphene synthesis by flash Joule heating	James M. Tour, Wilbur Carter Kittrell, Duy X. Luong, Wala Algozeeb, and Weiyin Chen
2021-011-PCT	PCT	Filed	Not Applicable (PCT App)	PCT/US21/052030	9/24/21	Ultrafast synthesis of carbide, corundum nanoparticles, and precious metal recovery from waste by a flashing joule heating process	James M. Tour and Bing Deng
2021-011-PCT2	PCT	Filed	Not Applicable (PCT App)	PCT/US21/052043	9/24/21	Ultrafast synthesis of carbide, corundum nanoparticles, and precious metal recovery from waste by a flashing joule heating process	James M. Tour and Bing Deng
2021-011-PCT3	PCT	Filed	Not Applicable (PCT App)	PCT/US21/052057	9/24/21	Ultrafast synthesis of carbide, corundum nanoparticles, and precious metal recovery from waste by a flashing joule heating process	James M. Tour and Bing Deng
2021-011-PCT4	PCT	Filed	Not Applicable (PCT App)	PCT/US21/052070	9/24/21	Ultrafast synthesis of carbide, corundum nanoparticles, and precious metal recovery from waste by a flashing joule heating process	James M. Tour and Bing Deng
2021-031-PZ2	Provisional	Active	United States	63/285,952	12/3/21	Flash Recycling of Batteries	James M. Tour, Wilbur Carter Kittrell, Duy X. Luong, and Weiyin Chen